

## MASTER THESIS

**Master's degree in Advanced Materials Science and Engineering**

# **LASER-ASSISTED SURFACE MODIFICATION OF ZIRCONIA-BASED MATERIALS TO ENHANCE OSTEOBLAST RESPONSE FOR DENTAL APPLICATIONS**



## **Memory and Annexes**

**Author:** Nerea Garcia de Albeniz  
**Director:** Joan Josep Roa Rovira  
**Co-Director:** Carles Mas Moruno

October2020



## Abstract

Zirconia based materials are considered one of the best choices for dental applications due to its superior mechanical properties, aesthetic advantages and biocompatibility. Furthermore, in the last decade, the use of topographic patterns has been a continuously growing area of research for tissue engineering and it is widely accepted that the surface topography of biomaterials can influence the biological response. On this matter, micro-topographical modification of dental zirconia (3Y-TZP) has demonstrated to play an important role in cell response in terms of adhesion, proliferation and differentiation. In this sense, one studied approach is to modify the surface roughness at micrometric-length scale by means of laser technique.

The main goal of this Master's project is to investigate the effect of microscale surface modification of dental zirconia (3Y-TZP) to promote bone cells adhesion and growth. The samples were prepared by Cold Isostatic Pressing and sintered at 1450 °C. Afterwards, the surface modification was conducted by using a nanosecond laser equipment. The created topographical pattern consists on parallel lines with different interspaces of 30, 50 and 100 µm; and these three samples were also compared to flat 3Y-TZP. Afterwards, the specimens were microstructurally characterized by means of: Archimedes method for density calculation and confocal laser scanning microscopy for the topographical analysis of the patterns. Furthermore, the samples were hydrothermally degraded in steam water for 10 hours, and after microstructural (X-Ray diffraction "XRD" and Raman) and mechanical (Vickers hardness) characterization was performed to the non-degraded and degraded samples. Finally, cellular study was conducted to evaluate the behaviour of hMSCs on the modified surfaces after 6 hours of adhesion.

The result showed laser patterns of ~ 1.7µm height and pronounced pile-up as side effect of the laser beam. The XRD and Raman characterization showed that m- phase transformation was induced on the sample surface after 10 hours of degradation in water steam, while the  $V_m$  (%) content obtained in the non-degraded samples was negligible. Also, the Vickers hardness was decreased after the degradation process. Finally, all the patterned surfaces allowed cell attachment, increased cell area and elongation morphology, and promoted cell alignment in the direction of the laser patterns.

## Resumen

Los materiales base zircona son considerados *gold estándar* en aplicaciones dentales debido a que presentan propiedades mecánicas superiores, ventajas estéticas y gran biocompatibilidad. Además, en la última década, se ha incrementado el uso de patrones topográficos en el campo de ingeniería de tejidos, en donde es ampliamente aceptado que la topografía de la superficie de los biomateriales puede influenciar la respuesta celular. En esta cuestión, la modificación de la microtomografía de la zircona dental (3T-TZP) ha demostrado tener gran influencia sobre la respuesta celular en términos de adhesión, proliferación y diferenciación. En este sentido, uno de los métodos más estudiados para la modificados de la rugosidad a escala micrométrica es mediante el láser.

La presente tesis de Máster tiene como principal objetivo investigar el efecto de la modificación superficial a nivel micrométrico de la zircona dental (3Y-TZP) para promover la adhesión y el crecimiento celular. Las muestras utilizadas se prepararon median la técnica de compresión Isostática en Frio (CIP) y posteriormente se sinterizaron a 1450 °C. A continuación, se realizó la modificación superficial de las muestras mediante un equipo laser nanosegundo. Los patrones topográficos creados consisten en líneas paralelas con diferentes interlineados de 30, 50 and 100  $\mu\text{m}$ ; y estas tres muestras se compararon también con una muestra plana. Posteriormente, las muestras fueron caracterizadas microestructuralmente mediante: el método de Arquímedes para el cálculo de las densidades y la microscopia láser confocal para analizar la topografía de los patrones. Además, las muestras fueron degradadas en vapor de agua durante 10 horas, y posteriormente se caracterizó la microestructura (difracción de rayos X "XRD" y Raman) y propiedades mecánicas de las mismas (dureza Vickers). Finalmente, se realizo un estudio celular para evaluar el comportamiento de las HMSCs hacia los patrones celulares para un tiempo de adhesión de 6 horas.

Los resultados demuestran que los patrones laser presentan una profundidad de alrededor de 1,7 $\mu\text{m}$ , y que el acumulamiento de material producido en los bordes es pronunciado. El análisis XRD y Raman muestra que se induce fase monoclinica en la superficie después de 10 horas de degradación hidrotérmica, mientras que el  $V_m$  (%) de las muestras no degradadas es negligible. Además, se observa como la dureza Vickers decrece después del proceso de degradación. Finalmente, se observó como los patrones láser facilitan el anclaje de las células, incrementan el área y la forma elongada de las células, y promueven la alineación celular en la dirección de los patrones.

## Acknowledgements

This Project Course work was carried out at the at Universitat Politècnica of Catalunya (UPC), Spain, as part of the Erasmus Mundus Advanced Materials Science and Engineering Master Programme. The research groups involved are the Centre for Structural Integrity, Reliability and Micromechanics of Materials (CIEFMA) and the Biomaterials, Biomechanics and Tissue Engineering (BBT), both of them part of the Department of Materials Science and Engineering at UPC.

Firstly, I would like to thank my thesis directors Joan Josep Roa Rovira and Carles Mas Moruno for giving me the opportunity to work in this project and for all their support and guidance provided to carry out this project. Also, I would like to thank the PhD STUDENT Joaquim Minguela for the help in the result interpretations and the training of the laser equipment. I also appreciate the help and assistance from the CIEFMA laboratory technicians Fernando, who trained and taught me to use the equipment that was necessary to carry out this work. Furthermore, I thank Meritxel for the training of the cell culture laboratory.

I thank the AMASE program for accepting me and giving me the opportunity to be here. To the friends that I have cultivated in this experience. Thank you for making my experience abroad as wonderful as it was.

Last but not least, I would like to thank my family, friends and boyfriend for the emotional support.



## Glossary

**AFM:** Atomic Force Microscope

**BCC:** Body-Centered Cubic

**CIP:** Cold Isostatic Pressing

**FCC:** Face-Centered Cubic

**FESEM:** Field Emission Scanning Electron Microscope

**FIB:** Focused Ion Beam

**hMSC:** *human Mesenchymal Stem Cells*

**LSCM:** Laser Scanning Confocal Microscopy

**LTD:** Low-Temperature Degradation

**OM:** Optical Microscope

**PSZ:** Partially Stabilized Zirconia

**SEM:** Scanning Electron Microscope

**TZP:** Tetragonal Zirconia Polycrystals

**XRD:** *X-Ray Diffraction*

**xY-TZP:** Tetragonal zirconia partial stabilized with x molar percent of yttria

**YSZ:** Yttria-stabilized Zirconia

**ZTA:** Zirconia Toughened Alumina





## Outline

<b>ABSTRACT</b>	<b>I</b>
<b>RESUMEN</b>	<b>II</b>
<b>ACKNOWLEDGEMENTS</b>	<b>III</b>
<b>GLOSSARY</b>	<b>V</b>
<b>PREFACE</b>	<b>1</b>
Background .....	1
Motivation.....	2
Structure of the project .....	3
<b>INTRODUCTION</b>	<b>4</b>
Zirconia based ceramic .....	4
1.1.1. General information .....	4
1.1.2. Microstructure.....	5
1.1.3. Stabilization of Zirconia .....	6
1.1.4. Phase transformation.....	9
1.1.5. Properties .....	15
1.1.6. Applications .....	16
Zirconia in dentistry .....	22
1.1.7. Types of zirconia used in dentistry.....	22
1.1.8. Biocompatibility.....	26
1.1.9. Biological response to implants .....	27
1.1.10. Influence of the surface properties on implant-tissue response .....	31
Surface modification of zirconia-based ceramics .....	33
1.1.11. Grinding/polishing process.....	34
1.1.12. Sandblasting .....	35
1.1.13. Chemical etching .....	37
1.1.14. Laser treatment .....	39
1.1.15. Ultraviolet light treatment .....	41
1.1.16. Coatings .....	43
<b>STATE OF THE ART</b>	<b>47</b>
<b>OBJECTIVES</b>	<b>55</b>
<b>EXPERIMENTAL METHODS</b>	<b>56</b>

Materials .....	57
Sample preparation .....	58
4.1.1. Conforming method.....	58
4.1.2. Sintering process.....	60
4.1.3. Polishing of the samples .....	63
Design of Experiments (DoE).....	65
4.1.4. Concept and definition .....	65
4.1.5. Methodology.....	66
4.1.6. Design of the laser experiments .....	68
Surface treatment .....	0
4.1.7. Laser treatment.....	0
Hydrothermal degradation .....	1
Characterization techniques .....	2
4.1.8. Microstructural characterization.....	2
4.1.9. Mechanical characterization.....	11
Cellular study .....	13
4.1.10. Cell culture .....	13
4.1.11. Cell adhesion .....	14
<b>RESULTS AND DISCUSSION .....</b>	<b>15</b>
Selection of the laser parameters .....	15
Microstructurally characterization.....	16
5.2.1. Density .....	16
5.2.2. Topographical characterization.....	17
Hydrothermal degradation .....	19
5.3.1. Raman Spectroscopy.....	19
5.3.2. XRD .....	21
5.3.3. Vickers Hardness .....	22
Cellular study .....	23
5.4.1. Qualitative analysis.....	23
5.4.2. Quantitative analysis .....	26
<b>ENVIRONMENTAL IMPACT ANALYSIS .....</b>	<b>28</b>
<b>CONCLUSIONS .....</b>	<b>29</b>
<b>FUTURE WORK .....</b>	<b>31</b>
<b>BIBLIOGRAPHY .....</b>	<b>32</b>

<b>ANNEX A</b>	<b>49</b>
Annex A.1 Design of Experiments.....	49
Annex A.2 Interface of L-Win and Weldmark.....	58



## **Preface**

The work presented in this master thesis is the result of my master studies in Advanced Materials Science and Engineering (AMASE) programme. The project was developed at the Polytechnic University of Catalunya-BarcelonaTECH (UPC), between January 2020 and October 2020. The research groups involved are the Centre for Structural Integrity, Reliability and Micromechanics of Materials (CIEFMA) and the Biomaterials, Biomechanics and Tissue Engineering (BBT), both of them part of the Department of Materials Science and Engineering at UPC.

## **Background**

The history of the evolution of dental implants is a magnificent and fascinating journey through time. As early as 2000 BC, early versions of dental implants were used in the civilization of ancient China. Carved bamboo pegs were originally used to replace the missing teeth at that time [1]. Since then, the materials in which dental implants came into development range from gold ligature and ivory to chromium, cobalt, iridium and platinum [2]. However, those materials did not prove to be very successful: the primary issue was the rejection of the foreign body dental implant.

For the implant to be successful, the implant surface and the peri-implant bone need to achieve a strong and durable connection together through a process known as osseointegration [3]. Since the concept of osseointegration emerged for the first time in 1950, materials like titanium led to significant improvement in the techniques used for tooth replacement. However, incomplete osseointegration and mechanical loosening still represent key challenges associated with the use of metallic implants [1]. Regarding these issues, recent clinical studies reported that dental implants made from zirconia-based materials are a promising alternative to titanium dental implants. In addition to their excellent mechanical properties and cosmetic results (i.e. whitish colour), zirconia-based implants allow a degree of osseointegration and soft tissue response that is superior to that of titanium dental implants [4].

Furthermore, in the last years, special attention has been given to the relation between the surface modification of the material and the biological response to the implant. The purpose of surface modification is to alter the properties of the surface to enhance the biological performance of the surface, without changing the bulk properties of the material [5]. On this matter, the optimization of the roughness has shown to be a key approach. Instead of being simply smooth, the surfaces are generally roughened by sandblasting and acid etching, which dramatically increases the surface area to which bone can attach [2].

## Motivation

The global market for dentistry is an attractive segment of the medical device sector. It was evaluated at 26 billion USD in 2018 and is expected to reach 36.5 billion USD by the end of 2024 [6]. This growth is driven by the expansion of the elderly population worldwide and increasing consumer awareness of oral healthcare needs [7]. Within the dental market, dental implants field is the one growing faster. There is a tremendous increase in patients' demands and expectations for more aesthetic dental implants with higher survival rates, which has made clinicians interested in the osseointegration and survival of implants. However, there is still much work to do in terms of implants durability, where incomplete osseointegration and implant infection represent the major concerns.

At present, zirconia-based materials are gaining interest as bioceramic materials for implants applications due to their superior biocompatibility, reduced bacterial plaque affinity, and low corrosion when compared to traditional titanium implants. Furthermore, surface modification of zirconia-based materials can be achieved by altering the topography and the surface chemistry, which has proven to have a major impact on osseointegration and the bacterial response to the implant. Different approaches have been used to improve the surface properties of zirconia-based materials, including polishing, sandblasting, acid etching, biofunctionalization, coating, laser treatment, and ultraviolet light treatment, between others. Nonetheless, there is a need for more research to find the specific surface modification technique that maximizes the potential of zirconia as an implant material. The present work aims to contribute to the search for that technique. It provides an insight into the effectiveness of laser treatment and chemical etching surface modification techniques to enhance the cell adhesive potential of the investigated material. To this end, *in vitro* cellular studies were carried out to determine which pattern and topography more optimally favours the cellular response. Furthermore, the success of this material also depends on its final properties after the surface modification, thus the mechanical properties and microstructure were also analysed.

On a personal level, I am very pleased to be able to collaborate in some way in the investigation of new strategies to improve dental implants. What is more, it is about improving people's health and well-being. Furthermore, regarding the academic field, this research project is an opportunity to combine my biomedical engineer and materials science studies and put them into practice. It enables me to get more familiar with many sample preparation and characterization equipment, as well as to learn how to interpret the results. Also, it will help me develop my communication and self-learning skills.

## **Structure of the project**

### **Chapter 1. Introduction**

This chapter is a review of zirconia-based ceramic materials and their properties, with a focus on their applications in dentistry. Moreover, the biocompatibility of zirconia is widely explained: biological responses to the implant materials and how the surface properties influence the cellular responses. The introduction ends up with an overview of the existing surface modification strategies.

### **Chapter 2. State of the art**

Chapter 2 analyses the current status of the three relevant topics of this work: zirconia-based materials, surface modification treatments, and cellular response to implant materials. The analysis made is based on the trend that these topics followed during the last 10 years in terms of the number of published papers.

### **Chapter 3. Objective**

In this chapter, the aims and scope of the project are presented.

### **Chapter 4. Experimental methods**

This chapter includes a detailed explanation of the material used and the experimental procedure followed during the preparation of the samples. Next, the techniques and parameters selected for the surface modification of the zirconia samples are presented. Also, there is a description of the procedure of the cell culture done on the samples and the timetable followed for the observation of the cell behaviour. In the last subsection, the characterization techniques used in the project are described, which includes microstructural and mechanical characterization and the evaluation of the cellular response to different surfaces.

### **Chapter 5. Summary of the main results and discussion section**

Chapter 5 summarizes the main findings. The results and discussion of the microstructural and mechanical characterization before and after the surface treatment are presented. Furthermore, the finding obtained concerning the cell-behaviour study are included.

### **Chapter 6. Conclusions**

General conclusions and perspectives are summarized. The conclusions are based on the objectives set at the beginning of the project and on the findings obtained at the end.

### **Chapter 7. Future work**

Finally, the different possible tracks to be followed after this project are presented.

## Introduction

Currently, zirconia is one of the most important ceramic materials at the industrial level due to its excellent mechanical and microstructural properties. This introductory chapter will present the information required to understand the material of study.

This chapter is divided into three sections:

- i. The first section gives a general overview of zirconia, its microstructure, properties and general classification. Furthermore, emphasis is given to the transformation toughening property of zirconia, which is a major advantage compared with other ceramic materials. It is also explained the main limitation of this material, hydrothermal degradation, a phenomenon that has been very important for its development. Finally, some of the current applications of zirconia are explained, with a special focus on the biomedical field.
- ii. The second section is focused on the dental applications of zirconia. The advantages of zirconia as dental material as well as the types used in dentistry are explained. Next, the biological response to the implant is explained, which includes bone tissue integration and bacterial adhesion. In addition to that, the relation between the cellular response and various surface properties is described.
- iii. Finally, the last section gives an overview of the current surface modification techniques used in zirconia to enhance cellular response and their reliability.

### ***Zirconia based ceramic***

#### **1.1.1. General information**

Zirconium dioxide ( $\text{ZrO}_2$ ), also known as zirconia, is a material classified as advanced ceramic since it is composed of metallic zirconium (Zr) and non-metallic oxygen (O) elements bonded by ionic and covalent bonding [8]. It was first discovered in 1789 by the chemist Martin Klaproth while he was studying the mineral zircon, but isolated for the first time later in 1824 by the Swedish chemist Jöns Jakob [9] [10].

The main sources of the zirconia are zirconate ( $\text{ZrO}_2\text{-SiO}_2$ ,  $\text{ZrSiO}_4$ ) and baddeleyite ( $\text{ZrO}_2$ ). Zirconate is more abundant, but less pure, requiring significant processing to get zirconia. By contrast, baddeleyite is a source of extreme purity in obtaining the material since it already contains levels of zirconia ranging from 96.5 to 98.5% [11].



### 1.1.2. Microstructure

Zirconia ( $\text{ZrO}_2$ ) is a polymorphic material that, at ambient pressure, can exist in three different crystallographic phases depending on the temperature: a monoclinic ( $m$ -), a ( $t$ -) tetragonal and a ( $c$ -) cubic phase. At ambient temperature and upon heating up to  $1170^\circ\text{C}$  zirconia is on its  $m$ -phase. Then, the  $t$ -phase form is stable between  $1170$  and  $2370^\circ\text{C}$ , which has a fluorite-like structure with a body-centered cubic (BCC) unit cell. Finally, the crystallographic form is  $c$ -phase above  $2370^\circ\text{C}$  and up to the melting point ( $\sim 2680^\circ\text{C}$ ). The  $c$ -phase has also a fluorite-like structure, but with a face-centered cubic (FCC) cell distribution. The three crystallographic forms of pure zirconia are shown in **Figure 1** [12]–[14].

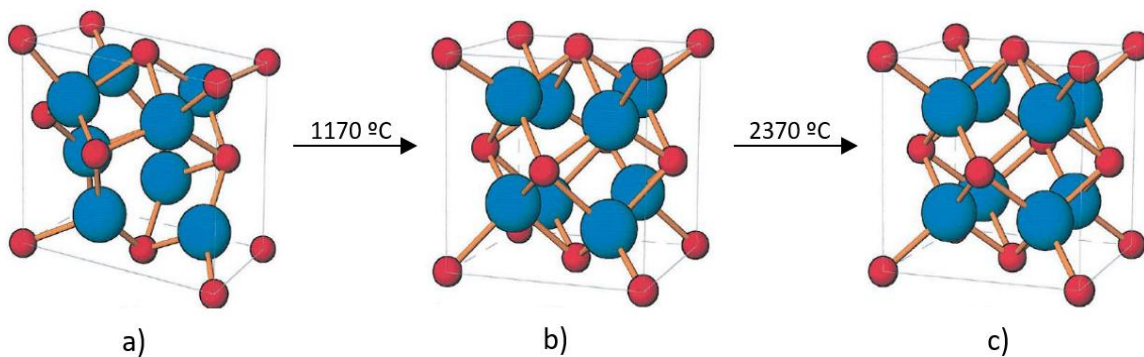


**Figure 1.** Schematic representations of the three crystal structures of  $\text{ZrO}_2$  (a) monoclinic, (b) tetragonal, and (c) cubic [15].

The main drawback of  $\text{ZrO}_2$  is attributed to the displacive tetragonal ( $t$ -) to monoclinic ( $m$ -) phase transformations that undergoes the material, which occurs at a temperature between  $850$  and  $1000^\circ\text{C}$  (depending on the cooling process). The  $m$ - configuration occupies 3-4 % more volume than the  $t$ -configuration, which is a relatively large volume change. When the material is cooled, there is a  $t \rightarrow m$  phase transformation accompanied by a shear strain of  $\sim 0.16$  and volume expansion of  $\sim 4\%$ . Unaccommodated, this change shape in the transformation volume induces high internal compressive stresses, embrittlement and cracking of the material, which result in the catastrophic fracture of the fabricated components. This phase transformation is also known as martensitic transformation since it exhibits a high-speed volume shape change that occurs by shear without diffusion [16] [17] [18].

The martensitic transformation makes the sample more brittle and with reduced mechanical properties. However, this is avoided by alloying pure  $\text{ZrO}_2$  with stabilizers. The stabilizer allows the retention of the  $t$ - or  $c$ - structure at room temperature, so as the  $m$ -phase does not form under normal cooling conditions, the volume expansion and subsequent crack formation are avoided [8] [19].

### 1.1.3. Stabilization of Zirconia

As stated previously, it is possible to stabilise high-temperature phases of  $\text{ZrO}_2$  at low temperature by doping it with certain aliovalent ions, also known as stabilizers. When the temperature decreases, the oxygen overcrowding around the lattice hinders the small Zr atom to maintain the fluorite structure and generates internal strain, which is relieved by changing the atom disposition into monoclinic structure. Therefore, the *t*- or *c*-phase structures can be stabilized at low temperature by the relaxation of the internal strain of the lattice, which can be achieved by two mechanisms [20]:

- by adding dopants with higher cation radius and lower valence that substitute Zr atoms and introduce oxygen vacancies in the lattice. This is the case of yttria stabilizer, where the oversized  $\text{Y}^{3+}$  cation substitute the  $\text{Zr}^{4+}$  cations and generate oxygen vacancies, which relieves the oxygen overcrowding around the small Zr atoms (see **Figure 2**) [21], and
- by stabilising the cation network: *distorting the network (undersized dopants)*, *dilating the network (oversized dopants)*, or *creating a strong cation-O bond*.

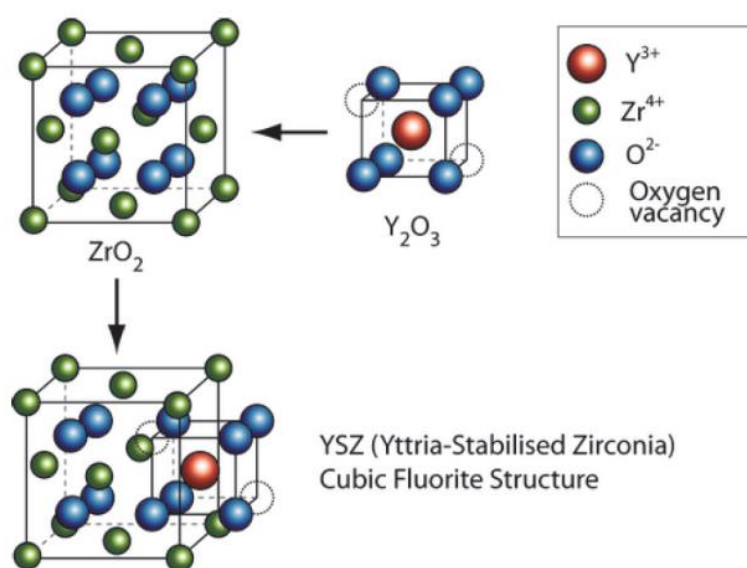


**Figure 2.** Oxygen vacancies formation into the  $\text{ZrO}_2$  lattice through the addition of  $\text{Y}_2\text{O}_3$  [20].

Furthermore, by increasing the amount of dopant more *c*-phase is formed, as illustrated in **Figure 3**. For the  $\text{ZrO}_2$ - $\text{Y}_2\text{O}_3$  system, usually a composition of 2-3 mol. % and 8 mol. % of yttria ( $\text{Y}_2\text{O}_3$ ) is used to stabilize the *t*- and the *c*-phases at room temperature, respectively [21].

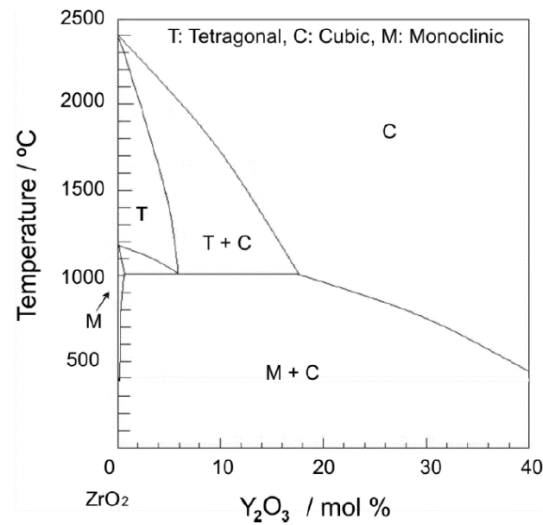


**Figure 3.** Portion of the phase diagram of  $ZrO_2$ - $Y_2O_3$  system [22].

Zirconia ceramic materials (monolithic or composites) are commonly referred to as Zirconia Toughened Ceramics (ZTC). Within this family, depending on the type of stabilizer used, they can be divided into three subcategories: TZP (Tetragonal Zirconia Polycrystals), PSZ (Partially Stabilized Zirconia) y DZC (Dispersed Zirconia Ceramics).

**Tetragonal Zirconia Polycrystals:** Zirconia TZP is a material composed of almost 100 % *t*-phase at room temperature, with a grain size in the range of 0.2 – 1  $\mu m$ . Two most common forms of TZP are often stabilized with yttria ( $Y_2O_3$ , **Figure 4a**) or ceria ( $CeO_2$ , **Figure 4b**), which is why they are designated with the prefixes “Y” and “Ce”, respectively, and a number that represents the concentration of the oxide in molar percentage (mol. %). For example, 3Y-TZP is a polycrystalline tetragonal zirconia stabilized with 3 mol. %  $Y_2O_3$ . The sintering temperatures are around 1300 – 1600  $^{\circ}C$  [23] [24].

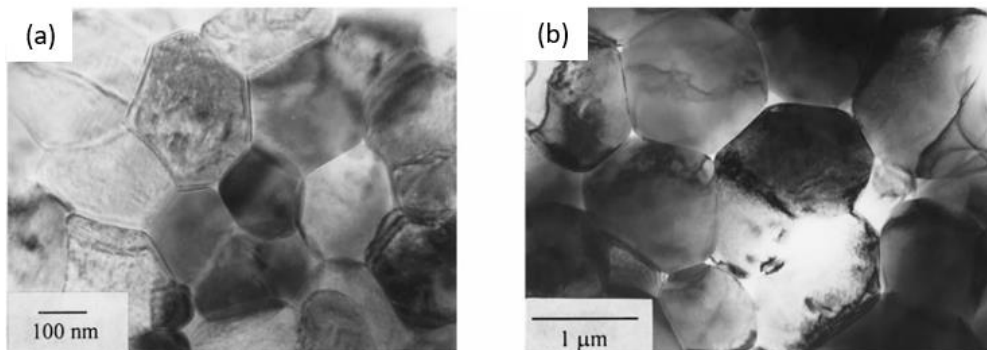


**Figure 4.** TEM micrographs of (a) 3Y-TZP, and (b) 12Ce-TZP; each sintered at 1300 $^{\circ}C$  for 2 h, with 1 wt.% of Mg- $Al_2O_3$ - $SiO_2$  glass [25].

**Partially Stabilized Zirconia:** The PSZ materials consist of a c-phase microstructure (large grain dimensions) with *t*-phase precipitates inside (finer grain dimensions). PSZ is obtained by adding high concentrations of stabilizer (8 – 10 mol. %), usually Magnesia (MgO) (see **Figure 5**) or Calcia (CaO) and sintering at high temperature ( $\sim 1600^\circ\text{C}$ ) [23] [26].

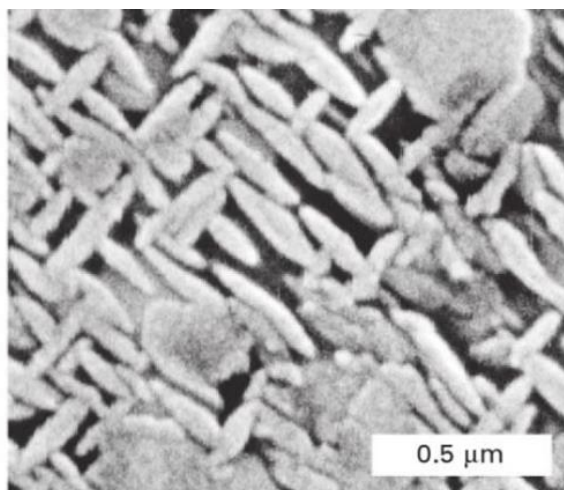


*Figure 5. SEM micrograph of the *t*- precipitates in Mg-PSZ [27].*

**Dispersed Zirconia Ceramics:** A composite material formed by a dispersion of *t*-ZrO<sub>2</sub> in a proportion ranging from 5 to 30 mol. % in a ceramic matrix. The mechanical properties of the DZC material, especially the fracture toughness, will depend greatly on the transformability of the dispersed zirconia. The most recognized example of this type of materials is zirconia toughened alumina (ZTA), illustrated in **Figure 6** [23].

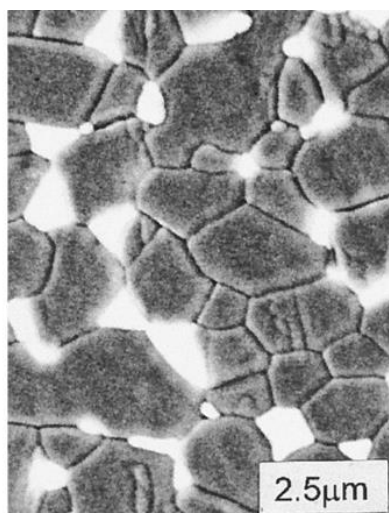


*Figure 6. SEM micrograph of ZTA, where the ZrO<sub>2</sub> grains are bright in contrast [18].*

Therefore, in all groups mentioned above the stabilizer maintains the  $t$ - of  $c$ -phase in a metastable state at room temperature. Besides the temperature, various parameters influence their stability, which is presented and briefly described below [8]:

- Grain/particle size: This parameter is relevant because the  $t$ - to  $m$ - phase transformation occurs in the grain boundaries. Indeed, below a critical value of particle size, the surface energy in the interface is no longer able to withstand the energy associated with the volume change of the grain during the phase transformation.
- Stabilizer content and distribution: The stability of the  $t$ - or  $c$ -phase is increased by increasing the quantity of the dopant. Therefore, heterogeneous dispersion on the dopant in the  $ZrO_2$  will lead to zones with a higher concentration of  $m$ -phase.
- Porosity and humidity:  $ZrO_2$  suffers from hydrothermal degradation since the nucleation of the  $m$ -phase is enhanced by water (**section 1.1.4.2**). Superficial porosity will increase the contact surface between the  $ZrO_2$  and water, especially on the surface area, and thus, reduce the stability of the  $t$ -phase.
- Residual stresses: While compressive stresses will stabilize the  $t$ -phase by preventing swelling, shear and tensile stresses will promote transformation towards the  $m$ -phase.

#### **1.1.4. Phase transformation**

Tetragonal to monoclinic ( $t \rightarrow m$ ) phase transformation has a significant role in stabilized  $t$ - $ZrO_2$  ceramics in either improving their toughness under externally applied stress or decreasing the properties under a humid environment. These two mechanisms are known as transformation toughening and ageing, respectively.

##### **1.1.4.1. Toughening mechanisms**

The toughening mechanisms in zirconia-based ceramic materials are related to volume expansion and shear strain associated with the  $t \rightarrow m$  phase transformation. The two main toughening mechanisms are stress-induced transformation toughening and micro-cracking toughening.

###### **2.1.4.1.1. Transformation toughening mechanism**

Transformation toughening mechanism implies the increase in the fracture toughness of the materials as a result of a phase transformation occurring at the tip of an advancing crack. For the transformation toughening to be successful, there are some essential requirements [28]:

- *The material must have a metastable phase which must be capable of transforming into a more stable phase by the stress-induced in the crack tip.*
- *The phase transformation must be instantaneous. It cannot require a diffusion process since it takes a long range of time.*
- *It must be accompanied by a volume or shape change.*
- *To ensure that there is a net increase in toughness of the material, the transformed product must not be significantly more brittle than the parent phase from which it forms.*

Martensitic transformations are defined as athermal and diffusionless changes in the crystal structure of a solid material that involve the simultaneous movement of atoms, to result in a macroscopic change of shape of the transformed region [28]. Therefore, in a material that has a metastable phase, the martensitic transformation can lead to transformation toughening of the material. This is the case of some stabilized zirconia materials where the stabilizer maintains the  $t$ -phase in a metastable state at room temperature. In these zirconia groups, the  $t \rightarrow m$  martensitic transformation is a key to transformation toughening of the material.

Alloying pure zirconia with stabilizing oxides such as CaO, MgO,  $Y_2O_3$  or  $CeO_2$  allows the retention of the  $t$ - structure at room temperature [17]. Under the application of external tensile stress, the metastable  $t$ -zirconia phase transforms to its thermodynamically stable  $m$ -phase. Following this transformation, there is a slight increase in the volume of the particle and the result is that compressive stresses are set on the vicinity of a propagating crack, which tends to close the cracks preventing their growth. The result is an increase in the toughness of zirconia, preventing the propagation of cracks and improving the mechanical behaviour of the material against tension stresses [29] [30]. A schematic representation of phase transformation toughening is shown in **Figure 7**.

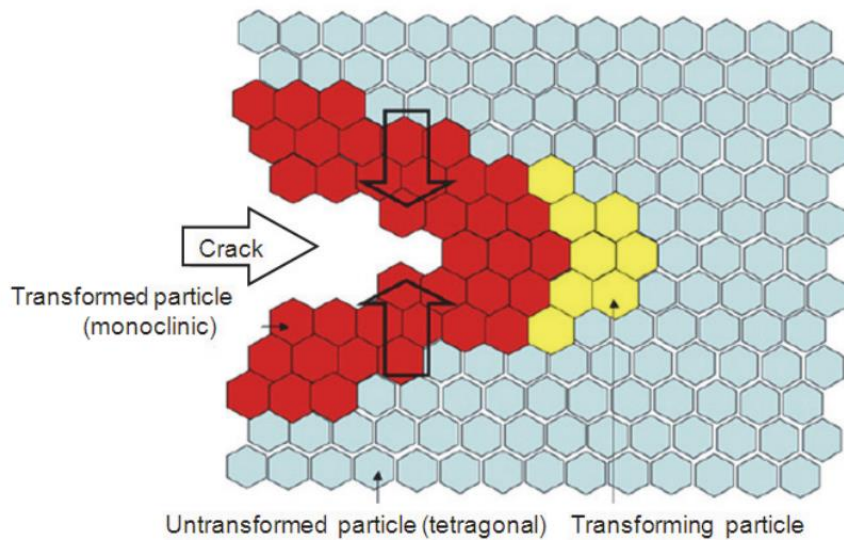


*Figure 7. Schematic illustration of transformation toughening mechanism in front of a propagating crack [31].*

The increment in toughness is dependent on the ease of transformation, and therefore, depends on the parameters governing the stability of the *t*-phase. These parameters are the stabilizer content and distribution, the grain size, the residual stresses, and the porosity of the material and ambient humidity discussed in the previous section.

#### 2.1.4.2. Microcrack toughening

The microcrack toughening mechanism relies on the idea that the microcracks ahead of the main crack can toughen the material. Due to the high stresses on the proximity of the main crack tip, stable grain boundary microcracks are nucleated. These microcracks can extend in response to the stress and, thus, lower the stress experienced by the tip on the main crack [32].

The microcrack toughening mechanism is also given in zirconia ceramics. Is the most common mechanism in ZTA [33]. When the  $\text{ZrO}_2$  is transformed from the *t*- to the *m*- phase, the associated volume expansion causes microcracking of the particles around the matrix. These microcracks will then lower the strain energy of the main crack tip and lead to the distortion and bifurcation of the main crack propagation path [34]. However, a high density of microcracks, rather than toughen the material will result in reduced fracture toughness [33].

Furthermore, it must be pointed out that in zirconia-based ceramic materials, generally, the presence of microcrack toughening mechanism is smaller compared with that of transformation toughening. The schematic of microcrack toughening mechanism is presented in **Figure 8**.



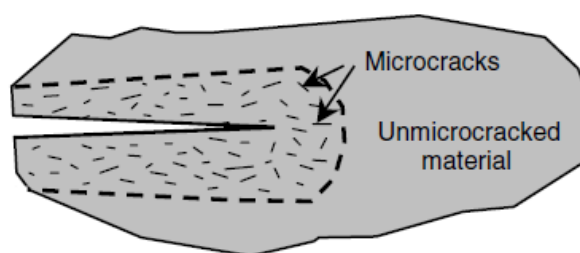


Figure 8. Schematic illustration of microcrack toughening mechanism [35].

#### 1.1.4.2. Hydrothermal degradation

On the other hand, the progressive and spontaneous transformation of the metastable *t*-phase into the *m*- one lead to the mechanical property degradation of zirconia, a process known as ageing [36]. The uncontrolled transformation takes place, particularly, in the aqueous medium, the water vapour medium or the medium of other liquids, at a relatively low temperature from 65 °C. Therefore, this phenomenon is also called hydrothermal degradation or low-temperature degradation (LTD) [37].

The LTD phenomenon was first described by Kobayashi *et al.* in 1981 [38]. They revealed that Y-TZP ceramics suffers a slow *t*- to *m*- phase transformation in the surface grains in a humid environment and at relatively low temperatures (150 – 400 °C), followed by microcracking and a loss in strength. Since then, several models have been proposed to explain the mechanism of degradation, but it is still not completely well understood. However, regardless of the type of mechanism, the accepted ageing facts are [37]:

- The degradation process is most intensive at a temperature of 200 - 300°C, and its time dependant.
- It is caused by the tetragonal to monoclinic transformation accompanied by microcracks.
- The transformation proceeds from the surface of the specimen into the inside.
- A moist environment accelerates ageing.
- Smaller grain size and higher stabilizer content retard the transformation.

##### 1.1.4.2.1 Nucleation and growth mechanism

Various approaches have been described to explain the ageing process of zirconia. The model proposed by Chevalier [39] is based on a nucleation and growth mechanism: LTD initiates at the surface of the zirconia material, propagates at the surface by a nucleation and growth mechanism and later progresses toward the bulk. First, there is nucleation on a particular grain at the surface caused by the water molecules. This transformation induces a volume expansion that induces stress on the



surrounding grains and microcracking (see **Figure 9a**). Then, the water penetrates through the microcrack on the grain boundaries and the transformation progresses from neighbour to neighbour (see **Figure 9b**). Finally, the growth of the transformation zone leads to microcracking, grain pull-out and finally surface roughening, which ultimately leads to strength degradation (see **Figure 9c**) [36].

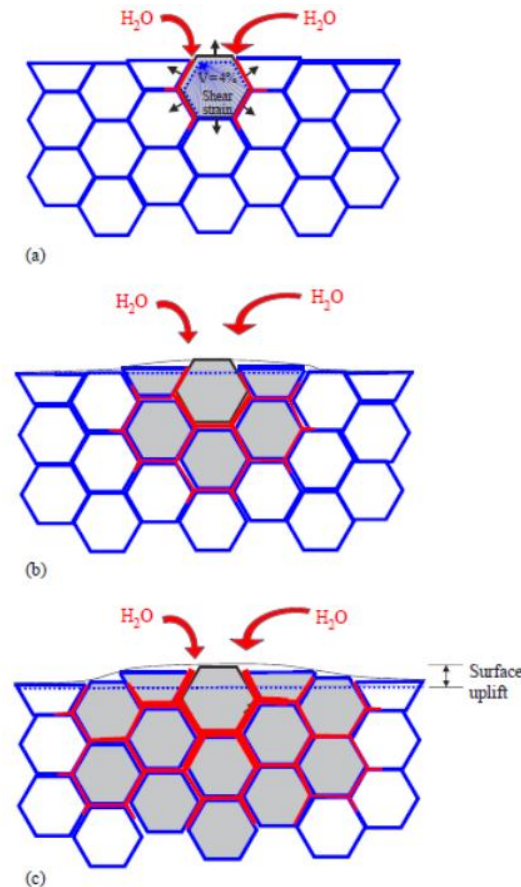


**Figure 9.** Scheme of the ageing process occurring in a cross-section, showing the transformation from neighbour to neighbour. Transformed grains are grey. The red path represents the penetration of water due to microcracking around the transformed grains [39].

Similarly, Emilio et al. [40] studied the hydrothermal degraded  $ZrO_2$  by mean of focused ion beam tomography. From the FIB images they proposed that microcracks are oriented preferentially parallel to the surface and mostly confined in a depth of  $3,8\mu m$  (see **Figure 10**). Furthermore, they observed that the microcracks are not connected to the surface. Based on that, they proposed that the microcracks do not act as water penetration channels, and, consequently, they do not accelerate the nucleation and growth process of the m-phase. they concluded that not significantly contribute as channels for water penetration, and, consequently, will not accelerate the nucleation and growth of the monoclinic phase produced by hydrothermal degradation.

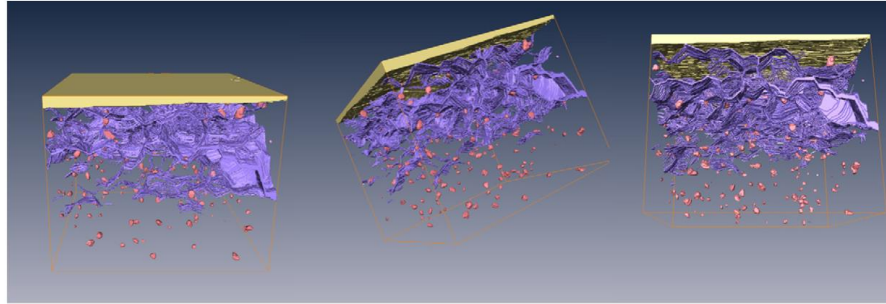


**Figure 10.** Three different perspectives of the reconstructed volume of microcracks, showing platinum protective layer deposited previous to the tomography (yellow), microcracks network (blue) and pores (red, -small spheres-). [40]

Furthermore, Gaillard *et al.* [41] studied the hydrothermal degradation mechanism of 3Y-TZP by degrading the material at 131°C in water vapour for different time periods (from 1 to 60 h). The AFM observations showed that the  $t \rightarrow m$  phase transformation occurs autocatalytically: *the transformation starts around defects with greater residual stresses and then propagates to neighbouring areas due to the stress generated by the volume increase*. The degradation extends autocatalytically until the surface is entirely transformed and then propagates into the volume. In **Figure 11** it can be distinguished the degraded surface layer, which is characterized by microcracking and phase transformation. In fact, it is possible to see the uniform habit plane that separates the  $m$ -phase from the  $t$ -phase. Furthermore, in the study they also obtained that the thickness of the degraded layer appears to be constant and about 2600 nm for the highest degradation time.

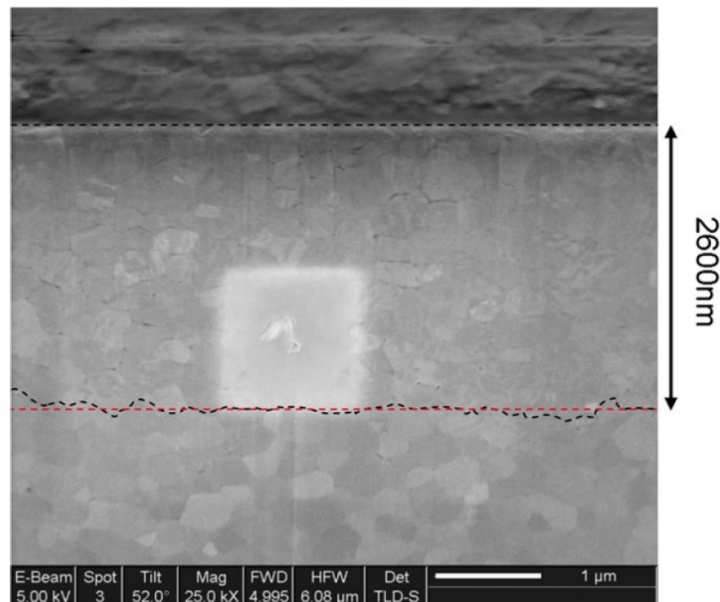


**Figure 11.** SEM pictures of a FIB cross-section of an 3Y-TZP sample after 60 h of degradation. The degraded layer is characterized by transformed grains and microcracking [41].

The hydrothermal degradation of zirconia has terrible consequences on the material, including  $t \rightarrow m$  phase transformation and microcracking, which consequently decrease the mechanical properties of zirconia.

#### **1.1.4.2.2**      *Variables affecting the hydrothermal degradation*

The main factors that affect the kinetics of the degradation process are those who influence the stability of the metastable  $t$ -phase. Thus, a zirconia material that possesses a more stable  $t$ -phase will be more resistant against hydrothermal degradation (under the same external factor). The most important variables affecting the degradation kinetic were described in **section 1.1.3**, which are: (i) *grain size*, (ii) *stabilizer content and dispersion*, (iii) *porosity of the surface*, and (iv) *residual stresses*.

One studied solution to deaccelerate the hydrothermal degradation is the addition of alumina ( $\text{Al}_2\text{O}_3$ ) particles. As an example, Zhang *et al.* [42] evaluated the incorporation of  $\text{Al}_2\text{O}_3$  in 3Y-TZP to improve the LTD resistance of the material without compromising on the mechanical properties. The results showed that the combined effect of stabilizing  $\text{ZrO}_2$  with a coating of  $\text{Y}_2\text{O}_3$  together with the addition of  $\text{Al}_2\text{O}_3$  significantly retarded the degradation of the material without affecting its transformation induced fracture toughness. In another study, Tovar-Vargas *et al.* [43] obtained an enhancement of the LTD resistance with the addition of alumina to ceria-calcia stabilized zirconia material.

Another solution proposed to enhance the LTD resistance of zirconia is the application of a nitriding to the material, which is a thermal treatment where  $\text{N}_2$  is added to the surface of the zirconia. The nitrogen replaces oxygen in the crystal structure and stabilizes the zirconia tetragonal structure at low temperatures. Dorado-Bustamante *et al.* [44] analysed the effect on ageing of incorporating nitrogen to 3Y-TZP and saw that the treatment increased the stability of the material and improved its LTD resistance.

### **1.1.5. Properties**

Zirconia material is characterized for its excellent mechanical properties since they are similar to those of stainless steel. However, its properties vary depending on the crystalline structure in which the atoms are disposed, as depicted in **Table 1**. The  $t$ -phase has increased fracture toughness and strength compared with the  $m$ - or  $c$ - ones, as transformation toughening phenomena only occurs on metastable  $t$ -phase. Also, the formation of  $c$ -phase, richer in stabiliser, can impoverish the surrounding  $t$ - grains, making them more susceptible to LTD (see **section 1.1.4.2.2**). Therefore, when mechanical properties prevail, it is more desirable the stabilization of the  $t$ -structure.

**Table 1.** Comparison of some mechanical properties of *m*-, *t*-, and *c*- zirconia. Where  $\rho$  is the density,  $E$  is the Young's modulus,  $HV$  is the Vickers hardness,  $\sigma_f$  is the fracture strength and  $K_{IC}$  is the indentation fracture toughness.

Property	<i>m</i> - zirconia [45] [46]	<i>t</i> - zirconia [47] [48]	<i>c</i> - zirconia [49]
$\rho$ (g/cm <sup>3</sup> ) [50]	5.83	6.10	6.09
$E$ (GPa) [41]	185	210	240
$HV$ (GPa)	11	13	15
$\sigma_f$ (MPa)	220	900-1200	290
$K_{IC}$ (MPa·m <sup>1/2</sup> )	3-4	7-10	1.5

Besides the excellent mechanical properties of zirconia, this material has other interesting properties that make it suitable for many applications. These key properties are [11] [16]

- *High-temperature stability: the maximum operating temperature is 2100 °C*
- *High density: 4 - 6 g/cm<sup>3</sup>*
- *Chemical inertness*
- *Biocompatibility*
- *Good wear and corrosion resistance*
- *Low thermal conductivity:  $\sim 2.5$  W/m·K at 25 °C (20 % that of Al<sub>2</sub>O<sub>3</sub>)*
- *Good thermo-shock resistance ( $\Delta T = 400 - 500$  °C)*
- *High thermal expansion coefficient:  $\sim 10 \cdot 10^{-6}$  K<sup>-1</sup> at 25°C*
- *Good ionic conductivity at high temperatures (500°C):  $< 1 \cdot 10^{-4}$  S·cm<sup>-1</sup>*

#### 1.1.6. Applications

Zirconia has already been widely used over 40 years for multiple sectors of the industry and because of its great impact, new possible applications are being continuously investigated. The physical, mechanical and thermal properties stated in the previous section make this material desirable for a wide range of application that vary from the automotive or structural ambit to medical purposes. Even though this section is focused on the biomedical applications of the zirconia, a summary of some other industrial applications is listed hereunder.

- Automotive industry

Within the automotive industry, zirconia is used to fabricate automotive engine components. One utilization is ceramic liners or fillings as piston crowns, main faceplates, and piston liners attached to metal engine elements (**Figure 12**), provided its high thermal resistance and high thermal expansion coefficient [51].



*Figure 12. Zirconia ceramic engine piston [52].*

- Refractory applications

Zirconia powder is used in refractory coatings to enhance thermal shock resistance and abrasion resistance. The refractory applications for zirconia include insulating fibre and thermal barrier coatings, electric furnace heaters over 2000 °C in oxidizing atmospheres (**Figure 13**), between others [53].



*Figure 13. Zirconia refractories in furnaces [54].*

- Cutting instruments and abrasion tools

Zirconia is used to make abrasion wheels and cutting tool ends (knives and scissors) (**Figure 14**). Due to its superior strength, hardness and wear resistance when compared to  $\text{Al}_2\text{O}_3$ , these tools retain their edge and stay sharp longer [53].



Figure 14. Zirconia ceramic knives [55].

- Energy applications

Stabilized zirconia, in particular 8Y-TZP, is one of the materials most used in oxygen sensors (**Figure 15**) and solid oxide fuel cells (SOFC) electrolytes because of its high level of oxygen-ion conductivity and its stability in both oxidizing and reducing atmospheres at high temperatures [53].

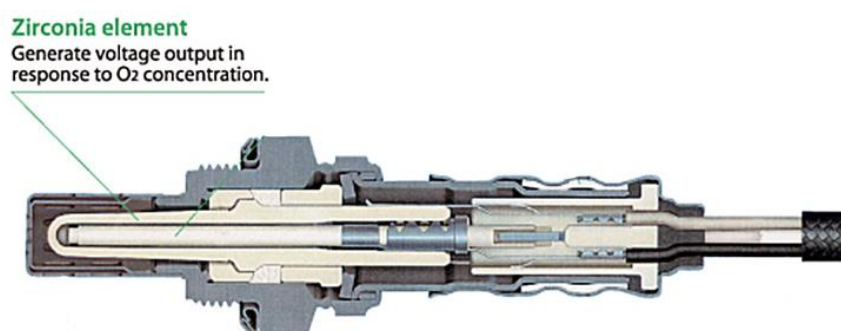


Figure 15. Zirconia oxygen sensor [56].

Apart from the applications mentioned, zirconia material has been mostly used in the biomedical field. It is considered to be a suitable ceramics material for biomedical applications because of its superior mechanical properties as well as high biocompatibility compared with other ceramics. Besides, zirconia-based ceramics have high corrosion resistance and lightweight. In the biomedical field, it is used in surgical tools and instrumentation manufacturing. However, the most widespread applications are dentistry and orthopaedics, specifically in the area of femoral heads for total hip replacements.

#### 1.1.6.1. Hip prosthesis

Among the most outstanding application of zirconia, hip prosthesis manufacturing has drawn significant attention, especially for the femoral head component. The hip prosthesis components were formerly made of metal alloys as Co-Cr or Cr-Ni alloys. However, these materials produced an inflammatory response of the tissue due to the wear particles generated during the lifetime of the prosthesis, and yet the problem was greater with the particles released due to the corrosion.

Bioceramic materials were introduced as an alternative to the traditional metallic hip prosthesis.  $\text{Al}_2\text{O}_3$  was first used as an alternative in the 1970s.  $\text{Al}_2\text{O}_3$  ceramics have biocompatibility, high wear resistance, and chemical durability, making them suitable for orthopaedic bearing. However, a high incidence of fractures of  $\text{Al}_2\text{O}_3$  femoral heads was reported due to the poor fracture toughness of the material [57]. To avoid this risk, in the late 1980s zirconia was introduced, which has one major advantage over  $\text{Al}_2\text{O}_3$ : *it offers 2 to 3 times higher flexure strength and fracture toughness, and thus its fracture resistance is significantly higher* [58].

Among all zirconia-based ceramics materials, yttria-stabilized zirconia (Y-TZP) has become the most attractive alternative in hip femoral heads manufacturing (**Figure 16**). Besides being biocompatible and wear and corrosion-resistant, this zirconia type is characterized because of its increased fracture toughness due to the phase toughening mechanism [58].



*Figure 16. Example of a femoral head made of zirconia [13].*

Nevertheless, the use of zirconia reduced drastically when in 2001 about 400 femoral heads failed only two years after their implantation in patients, when the expected lifetime was of 15 years. After much research, it was discovered that those failures were due to the hydrothermal degradation of zirconia [39]. The reasons of failure for a zirconia prosthesis implanted in the body are double. On one hand, because of the ageing phenomenon, the surface of the material is modified, leading to an increase in wear. On the other hand, microcracking processes may also promote premature failure of the device [10]. Nonetheless, the unfortunate event of femoral head premature failure has driven the scientific and orthopaedic community into more detailed research regarding the ageing phenomena of zirconia.

#### **1.1.6.2. Dentistry**

Zirconia is considered one of the best ceramics products in the market for dental reconstruction. Since Y-TZP was introduced to dentistry for the first time in the early 1990s, it has been increasingly used in the field of dental technology [59]. Nowadays it is estimated that between 15.000 and 20.000 zirconia dental structures are made every day worldwide [53].



The use of zirconia in dentistry arises from the search for the ultimate material to improve the aesthetic outcome of metal restorations. The search began in 1960, when ceramics materials (i.e. porcelain) were initially used as coating materials of the metallic implants, for a better aesthetic result. However, these ceramic materials were not characterized by having good mechanical properties, especially, they presented low strength, porosity and impurities [60]. Later on, zirconia and alumina coatings were introduced as an alternative, with zirconia coated-implants showing the best results regarding biocompatibility and strength. Furthermore, since the discovery of the stabilization of the metastable tetragonal phase of zirconia in 1990, the interest for zirconia-based ceramics in restorative medicine increased. Zirconia overshadowed alumina and also dental restorations started directing into metal-free prosthetic restoration. [61]

Zirconia meets the combined requirements for excellent aesthetic and superior strength. The transformation toughening mechanism provides this material with a high fracture toughness compared with other ceramics. Aside from its metal-like mechanical properties, zirconia has many advantages over alumina or metal implants, which are [12]:

1. *Decreased hypersensitivity compared to that caused by some metal implants.*
2. *Much lower conductivity than alumina, which reduces sensitivity to thermal changes.*
3. *Improves the aesthetic result, eliminating the shine of metals.*

Zirconia is increasingly being used for the fabrication of crowns, bridges, implants, implant abutments, veneers and orthodontic brackets, among others [53]. In **Figure 17** some examples of dental applications of zirconia are shown.

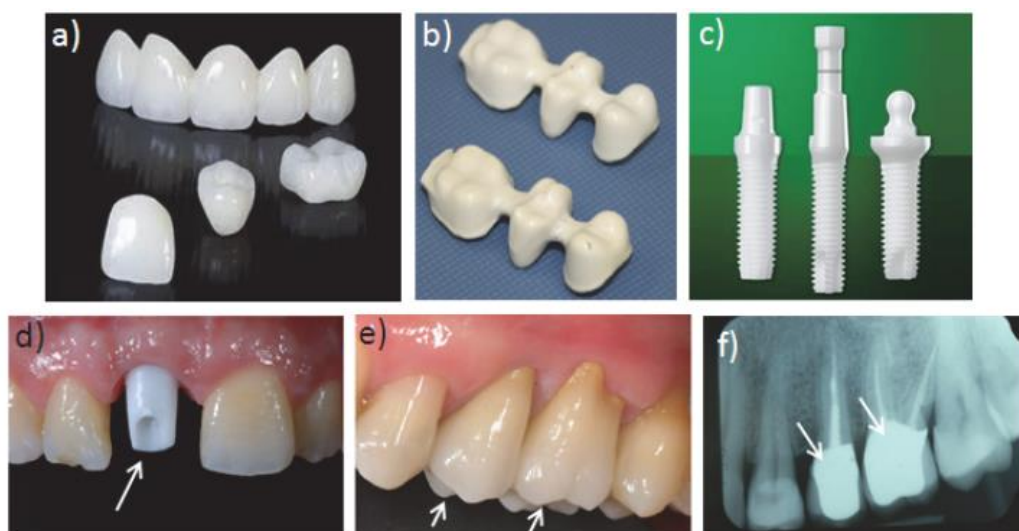


**Figure 17.** a) Dental crowns [62], b) three crown bridge [31], c) all ceramic implants, d) zirconia abutment for implants [63], e) cemented zirconia restorations and [63] f) radiographic evaluation of the two zirconia restorations [63].



- Zirconia crowns and bridges

Dental crowns are the caps that mimic the teeth by capping and encircling the teeth, reconstructing their shape, size and durability. Compared to ordinary metallic and porcelain crowns, zirconia-based crowns have the advantage of being translucent, which make possible to successfully mimic the natural tooth [64].

One important argument is the durability of the zirconia crown compared to other ceramics crowns, which are also aesthetically favourable, and to the metallic ones. A clinical study performed by Larsson *et al.* [65] revealed a cumulative 5-year survival rate of 97.1% for implant-supported zirconia crown., which is comparable to that of conventional porcelain-fused-to-metal crowns. Furthermore, Brignardello-Petersen [66] performed a study to determine the 5 and 10-year survival rate of zirconia-based all ceramics single crowns to 56 patients who had received 137 TSZCC. The obtained results showed a success rate of 97 and 62 % at 5 and 10 years, respectively.

- Zirconia brackets

Dental brackets made of zirconia have some advantages compared to the regular metallic ones: (i) *superior wear and deformation resistance*, (ii) *superior strength*, (iii) *they reduce plaque adhesion*, (iv) *improved aesthetic* [53].

- Zirconia implants and implant abutments

Commercially, the most used implants and implant abutments are made of titanium. However, the main disadvantage is the management of the greyish appearance of the soft tissue of the surrounding of the implant due to the peri-implant mucosa. Zirconia implants restoration allow preserving soft tissue colour more similar to the natural one compared to metal restorations [63]. This is because, besides good strength, zirconia implants offer enhanced biocompatibility, metal-like radiopacity for better radiographic evaluation, reduced bacterial adhesion, reduced plaque accumulation, and subsequently, low inflammation risk [53].

The clinical studies published to date on zirconia-based implants and implant abutments showed promising results of the implant survival rate. Cao *et al.* [67] reviewed several studies to evaluate the long-term survival of titanium implants with zirconia abutments after 5 years. The overall implant survival rate of implants with zirconia abutments was estimated to be 96 % and compared with all-titanium implants, the results significantly favoured implants with zirconia abutments. Also, Zembic *et al.* [68] resumed from six published clinical studies promising survival rate of zirconia implant. These studies showed low fracture rate of zirconia implants ranging from 0 to 4 %, compared to higher rates ranging from 10 to 12 % made out of glass-infiltrated ceramic after 5

years of clinical follow-up. Also, the authors stated that the fracture rate of the “gold standard” titanium implant at 5 years amounts to 1.6 %, being not much lower than the one obtained for ceramic implants.

## ***Zirconia in dentistry***

Ceramics are very important in the science of dental biomaterials. Due to an increasing interest in aesthetics and outcomes regarding toxic and allergic reactions of metal implants with body tissues, the dentistry community and researchers are looking for metal-free and tooth-coloured restorations [69]. Therefore, in the latter part of the 20<sup>th</sup> century, special attention has been given to the development of new high strength dental ceramics, which appear to be less brittle, less limited in their tensile strength, and less subjected to time-dependent stress failure [70].

Among all those dental ceramics, zirconia-based materials have stood out in contemporary restorative dentistry. These materials, also known as “ceramic steel”, have shown extraordinary mechanical properties for dental use: *superior toughness and high fatigue and wear resistance*. Besides, other significant advantages of zirconia must be highlighted [64]:

- (i) **Aesthetics:** Zirconium presents a bright and white tooth-like natural colour, which is a major advantage for tooth replacement applications. Zirconia implants appear even more natural than ceramics crowns with metal implants underneath. Moreover, the white colour of zirconia implants also eliminates the possibility of a darkened gum line that sometimes occurs due to metal implants.
- (ii) **Hygienic:** Zirconium dental implants are shown to produce less plaque accumulation compared to the titanium ones, which will promote healthier gums around the implant with a lower inflammation risk.
- (iii) **Strength:** The strength of zirconia implants is equal to that of titanium implants.
- (iv) **Biocompatible:** Zirconium is inert and therefore it does not cause any allergic reactions. It is well tolerated by both bone and soft tissue when implanted in the body.

### **1.1.7. Types of zirconia used in dentistry**

Although many types of zirconia-containing ceramic systems are available, only three of them are commercially available for dental healthcare applications. These are magnesium cation-doped partially stabilized zirconia (Mg-PSZ), zirconia-toughened alumina (ZTA), and the most widely used yttrium cation-doped tetragonal zirconia polycrystals (3Y-TZP) [17].

### 1.1.7.1. Magnesium partially stabilized zirconia

The microstructure of Mg-PSZ consists of fine *t*- precipitates embedded in a coarse *c*-zirconia matrix (30 – 60  $\mu\text{m}$ ) partially stabilized by 8 to 10 mol. % of MgO (**Figure 18**). This zirconia type is sintered at a temperature much higher than other composites, between 1680 and 1800  $^{\circ}\text{C}$ . Besides, the cooling cycle requires strict control since the *t*-phase precipitates at this stage ( $\sim 1100$   $^{\circ}\text{C}$ ) and its volume fraction controls the fracture toughness of the material [17] [64].

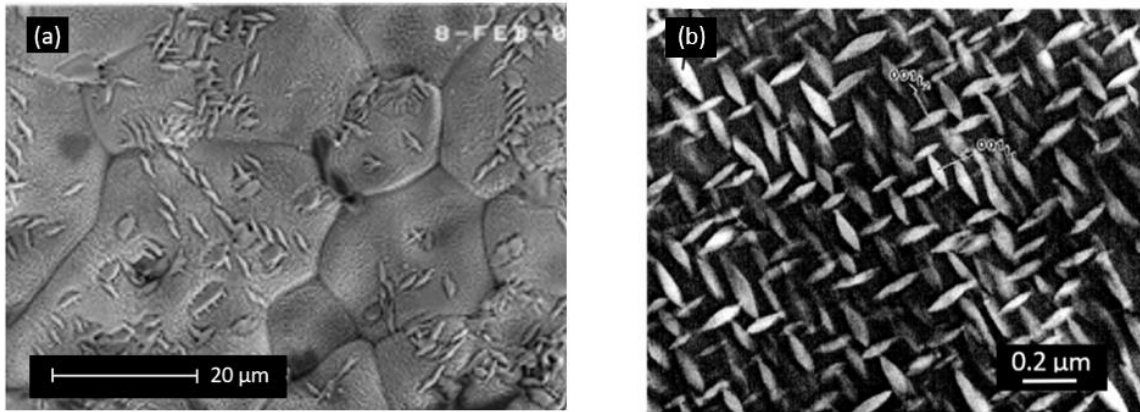


**Figure 18.** (a) Mg-PSZ microstructure with large *c*-grains (15-50  $\mu\text{m}$ ) and tiny *t*- precipitates [71]; and (b) lenticular *t*-ZrO<sub>2</sub> precipitates on *c*-faces [30].

Although much research has been dedicated to Mg-PSZ for its possible biomedical application, this zirconia type is reported unsuitable for dentistry because of its high porosity, associated with its large grain size that may lead to surface wear and large crack propagation [72]. Furthermore, Mg-PSZ precursors free of SiO<sub>2</sub> are difficult to obtain, so magnesium silicates may form and reduce the stabilizing Mg content in the grain.

A dental ceramic system called Denzir-M (Dentronic AB, Skellefteå, Sweden) is an example of Mg- PSZ ceramic currently available for hard machining of dental restorations [30].

### 1.1.7.2. Zirconia Toughened Alumina

Zirconia Toughened Alumina (ZTA) is a composite material formed by *t*-ZrO<sub>2</sub> dispersed in an Al<sub>2</sub>O<sub>3</sub> matrix, which utilizes the stress-induced transformation of ZrO<sub>2</sub> to achieve excellent mechanical properties. In contrast with the other two classes, the stability of the *t*-phase at room temperature does not necessarily involve the use of stabilizers but instead is controlled by the size, morphology and particle localization (intra-or intergranular) [73].

Among the dental ceramics, the only commercially available dental product which is ZTA is the In-Ceram Zirconia (Vident, Brea, CA, USA), consisting of 33 vol. % of 12 mol. % CeO<sub>2</sub>-stabilized zirconia

(12Ce-TZP) added to In-Ceram Alumina. A positive aspect of this zirconia type is that Ce-TZP ceramics usually exhibit better thermal stability and higher temperature degradation resistance than Y-TZP ceramics under similar conditions. However, as a drawback, ZTA shows a greater amount of porosity (between 8 and 11 %) when compared to Y-TZP (**Figure 19**), which explains the generally lower mechanical properties of In-Ceram Zirconia [11] [68].

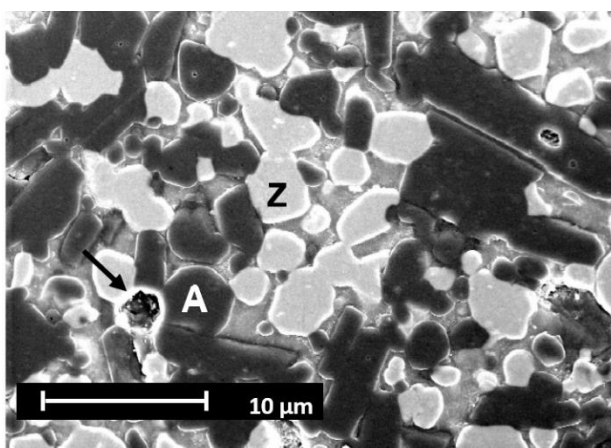


**Figure 19.** Microstructure of ZTA slip-cast ceramic. A: alumina grains, Z: zirconia grains, and black arrow indicates pore [74].

#### 1.1.7.3. Yttria full stabilized tetragonal zirconia polycrystal

The 3Y-TZP bioceramic consist of  $\text{ZrO}_2$  stabilized with 2 to 3 mol. % of yttria ( $\text{Y}_2\text{O}_3$ ) that is made of 100 % fine metastable *t*-grains, known as Y-TZP [11]. To date, studies on the potential of 3Y-TZP in dental applications continue to increase. It is the type of zirconia most frequently utilized for different dental applications since its mechanical properties are similar to those of metals and better than the other zirconia-based ceramic materials, whereas the colour approximates that of natural teeth [64]. Furthermore, it shows low porosity and high density [72].

It is important to point out that the mechanical properties of 3Y-TZP strongly depend on its grains size. The critical grain size for this material is 1  $\mu\text{m}$ . If the size exceeds this threshold, 3Y-TZP is less stable and more susceptible to spontaneous *t*- to *m*-phase transformation whereas smaller grain sizes (< 1  $\mu\text{m}$ ) are associated with a lower transformation rate. Moreover, when the grain size is below 0.2  $\mu\text{m}$  the transformation is not possible, and the fracture toughness of the material is reduced [68]. The sintering procedure dictates the grain size of the material, meaning that it has a strong impact on both the final properties and stability of the final product. Higher sintering temperature and longer sintering periods produce larger grain sizes, and consequently, the *t*- phase is less stable which results in reduced mechanical properties. The 3Y-TZP used in dental applications has a microstructure containing small grains which size range from 0.2 to 0.5  $\mu\text{m}$  in diameter, depending on the sintering temperature (**Figure**

20) [17]. Also, most manufactured of 3Y-TZP for dental applications recommend to eliminate grinding or sandblasting to maintain surface integrity and prevent the transformation of  $t \rightarrow m$  [73].

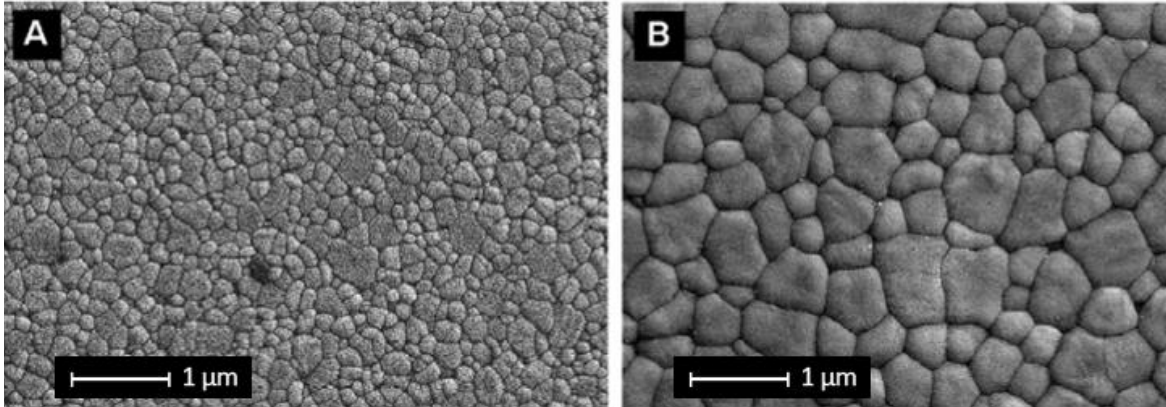


*Figure 20. 3Y-TZP ceramic sintered at (a) 1300 °C for 2 hours and (b) 1500 °C for 2 hours [74].*

Finally, it is necessary to mention that the  $Y_2O_3$  stabilizer content also influences the grain size and final properties of the material. Experiments have been performed regarding the optimum content of yttria, which concluded that 3 mol. %  $Y_2O_3$  is the optimal amount content so there is a balance between ageing and the mechanical properties. Higher yttria content (4 mol. %) has a higher hydrothermal resistance because the  $m$ -phase is reduced. However, this advantage is negated because bigger grains are obtained, and consequently, there is a notable decrease in fracture toughness [24].

In **Table 2** are presented the chemical composition as well as some microstructural and mechanical properties of Mg-PSZ, ZTA, and 3Y-TZP. In it can be seen that Y-TZP ceramic exhibits excellent mechanical properties among the other ceramics, especially its high bending strength. Furthermore, 3Y-TZP ceramic has a much higher fracture toughness compared to more brittle ZTA, making this material more preferable for this application, even if the compressive strength and hardness are lower.

*Table 2. Comparison of some properties of Mg-PSZ, ZTA and Y-TZP bioceramic materials [21].*

Property	Mg-PSZ	ZTA	Y-TZP
Chemical component	$ZrO_2 + 8-10\text{mol. \% MgO}$	$30\text{wt\% } ZrO_2 + 70\text{wt\% } Al_2O_3$	$ZrO_2 + 3\text{mol. \% } Y_2O_3$
Density [ $g \cdot cm^{-3}$ ]	5.74-6	$\geq 3.97$	$>6$
Porosity [%]	+	0.8-0.11	$<0.1$
Tensile strength [MPa]	450-700	$> 500$	900-1200

<b>Compression strength [MPa]</b>	2000	4100	2000
<b>Young modulus [GPa]</b>	200	380	210
<b>Fracture toughness [MPa·m<sup>1/2</sup>]</b>	7-15	4	7-10
<b>Thermal expansion coefficient [K<sup>-1</sup>]</b>	$7 \cdot 10^{-6}$	$8 \cdot 10^{-6}$	$11 \cdot 10^{-6}$
<b>Thermal conductivity [W·(m·K)<sup>-1</sup>]</b>	2	30	2
<b>Hardness [HV0.1]</b>	1200	2200	1200

### 1.1.8. Biocompatibility

“Biocompatibility refers to the ability of a biomaterial to perform its desired function concerning a medical therapy, without eliciting any inflammatory, allergic, immune, toxic, mutagen, or carcinogenic effects in the recipient or beneficiary of that therapy, but generating the most appropriate beneficial cellular or tissue response in that specific situation, and optimising the clinically relevant performance of that therapy” [75].

Biocompatibility is one of the most important advantages of zirconia-based ceramics, which may be attributed to its good hydrophilicity and protein adsorption [76]. Since the first proposal of zirconia material for medical applications in 1969, many *in vitro* and *in vivo* studies have confirmed its high biocompatibility [77]. An overview of some studies regarding the cytotoxicity, mutagenicity and radioactivity of zirconia is featured below.

*In vivo* and *in vitro* studies have been performed to evaluate the cytotoxicity of zirconia. *In vitro* tests have shown no toxicity in fibroblasts [78], lymphocytes [79], macrophages [80], and neither in osteoblast cells [81] [82]. Furthermore, Dalal *et al.* [83] observed that submicron-sized (0.2 - 0.9 µm) Zr-based particles, induced less osteoblast, fibroblast, and macrophage toxicity/reactivity when compared with larger (1 µm) CoCrMo-alloy and Ti-alloy particles. Several *in vivo* studies in various animals (rabbits, rats, monkeys) have also demonstrated no toxic effects of zirconia when implanted into soft tissues or hard tissues [84]–[86].

Radioactivity of zirconia has also been evaluated since zirconia powder contains small amounts of radionuclides from the uranium, radium and thorium actinide series. However, after purifying procedures, zirconia powders with low radioactivity (< 100 Gyh<sup>-1</sup>) can be achieved, which is near to those of alumina and Co-Cr alloys for medical use [87]. Besides, the radioactive potential of zirconia has been investigated by Bavbek *et al.* [88] and Giussano *et al.* [89] and both studies indicated that zirconia ceramic possesses negligible radionuclide activity that can be considered lower than many

hazardous radioactive appliances in our environment. Mutagenicity of zirconia has also been evaluated and all studies suggested that zirconia does not generate mutation of the cellular genome [72,] [73].

### **1.1.9. Biological response to implants**

The interface zone between an implant and the surrounding tissue is the most important factor in defining the biological response to the implant. When an implant is placed in contact with a physiological environment, different species interact with the material surface. Water and inorganic ions are the first molecules to come in contact with the surface, and then small organic molecules and proteins may be adsorbed onto it. Later, bigger entities like bacteria and human cells reach the surface and their adhesion is strongly mediated by the adsorbed protein layer on the surface of the implant [21].

In terms of the biological reaction of the host to the implanted foreign material, the success of the implant depends on two competitive processes: *bacterial colonization versus the adhesion of eukaryotic cells and formation of healthy tissue on the surface*. This is the so-called “race for the surface”, which suggests that the fate of the implant relies on the outcome of these two opposite pathways [92]. If the race is won by tissue cells, then the surface is covered by tissue and become less vulnerable to bacterial colonization. On the other hand, if the race is won by bacteria, tissue cells will not be able to subsequently colonize the surface and the success of the implant would be compromised. Unfortunately, during surgery microorganisms are frequently introduced on the implant surface, so they can start the race for the surface before this integration can occur [93].

#### **1.1.9.1. Bone tissue response**

There are three key concepts to take into account to study the bone response to the implant, osteoinduction, osteoconduction and osseointegration. These three phenomena are interrelated, but they are not identical. Based on ref. [94], they are defined as follows:

- Osteoinduction

This term means that primitive, undifferentiated and pluripotent cells are somehow stimulated to develop into the bone-forming cell lineage. It is the process by which osteogenesis is induced.

In addition to bone cells (i.e. osteoblasts, osteocyte and osteoclasts), bone and adjacent tissues also contain some undifferentiated cells like hematopoietic and mesenchymal stem cells. At the time of injury, those cells are recruited and developed into differentiated preosteoclasts cells that will digest damaged bone, and into osteoblasts that will form new bone. Osteoinduction plays an

important role in bone healing and implant anchorage since the majority of the newly formed bone depends on the osteogenic induction as depicted in **Figure 21**.

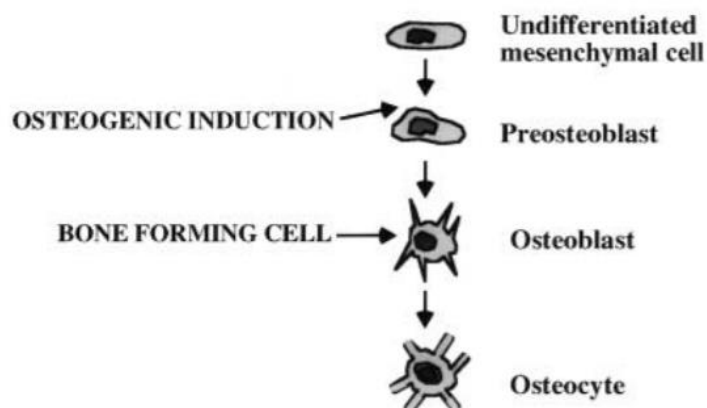


*Figure 21. Schematic representation of the induction process [94].*

- Osteoconduction

Osteoconduction is defined as the growth of bone on the surface of a foreign material. In the case of the implants, bone conduction is highly dependent on the biomaterial used and its interactions with cells. Thus, an osteoconductive surface is one that permits bone growth on its surface or down into pores, channels or pipes.

- Osteointegration

Many definitions of osteointegration have been suggested, but the most biomechanically oriented one is: "A process whereby clinically asymptomatic rigid fixation of alloplastic materials is achieved, and maintained, in bone during functional loading".

Osteointegration of the implant depends on:

- (i) *mechanical interdigitation, which ensures the primary fixation of the implant with the bone after surgery, and*
- (ii) *initial cellular interaction at the implant surface which promotes the osteoinduction and osteoconduction processes [3]*

Both osteoconduction and osseointegration depend not only on biological factors but also on the response to the foreign material. However, the main difference between them is that osteoconductive response may be rather short-lived while successful osseointegration maintains its bone anchorage over a long period. Therefore, osseointegration contributes to the long-term durability of the implant, meaning that a strong and durable connection must be achieved between the peri-implant bone and



the implant surface (**Figure 22**). Incomplete osseointegration leads to aseptic loosening of the implant, therefore it is of vital importance to evaluate the osseointegration capacity of the implant material.

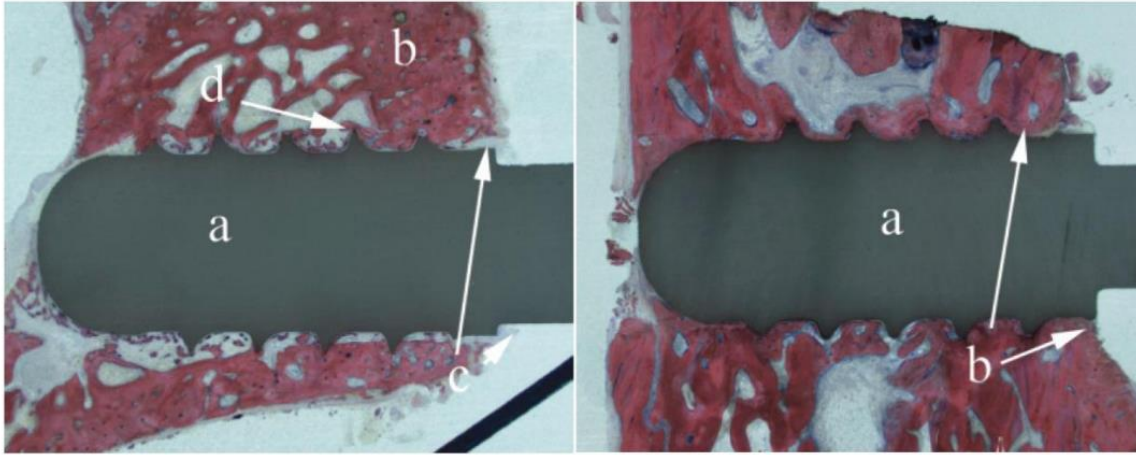


**Figure 22.** *Left: Zirconia machined implant showing a low degree of bone-to-implant contact after 12 weeks of healing: (a) implant; (b) bone; (c) tissue at the neck of the implant; (d) peaked threads. Right: Zirconia sandblasted implant showing a high degree of bone to implant contact after 12 weeks of healing: (a) implant; (b) arrows showing mineralized bone at the neck of the implant [15].*

Zirconia has shown to have good osseointegration capability. Josset *et al.* [82] investigated human osteoblasts in culture with zirconia and found that the osteoblasts showed good adhesion and spreading properties. Pandey *et al.* [95] also ensured good osteoconductivity of zirconia through *in vitro* human osteoblast cell culture. Furthermore, various studies have compared osseointegration of zirconia implants with titanium ones. Depprich *et al.* [96] did 12 weeks *in-vivo* investigation by introducing zirconia and titanium implants into the tibia of minipigs and obtained similar results in both cases. Similarly, Marques *et al.* [97] demonstrated that zirconia and titanium presented a similar pattern of bone healing after 60 days of implantation in rabbits. Even better, Kohal *et al.* [98] showed greater bone stability in zirconia implants (45/59 %) than in titanium (36/45 %) after 14 and 28 days.

#### **1.1.9.2. Bacterial adhesion**

Under favourable conditions, bacteria can attach to the surfaces of medical devices implanted in the human body, which is often the initial step in implant infection [99].

Bacteria constitute an entire ecosystem. As they cannot survive alone, they tend to organize into complex structures that facilitate their survival, called colonies. A colony is composed of the microorganisms together with their extracellular matrix (composed of secreted polymers like saccharides, proteins and glycoproteins). In the presence of a material, these microorganisms are capable of binding to the surface by attractive Van der Waals forces, electrostatic and hydrophobic interactions. These bacteria, known as first or early colonizers, secrete their own matrix and signalling

molecules recruiting secondary or late colonizers, thus initiating the formation of a biofilm [21]. The biofilm is a heterogeneous structure, both in space and over time, with “water channels” that allow transport of essential nutrients and oxygen to the cells growing within the biofilm [100]. A schematic of the biofilm formation process is presented in **Figure 23**.

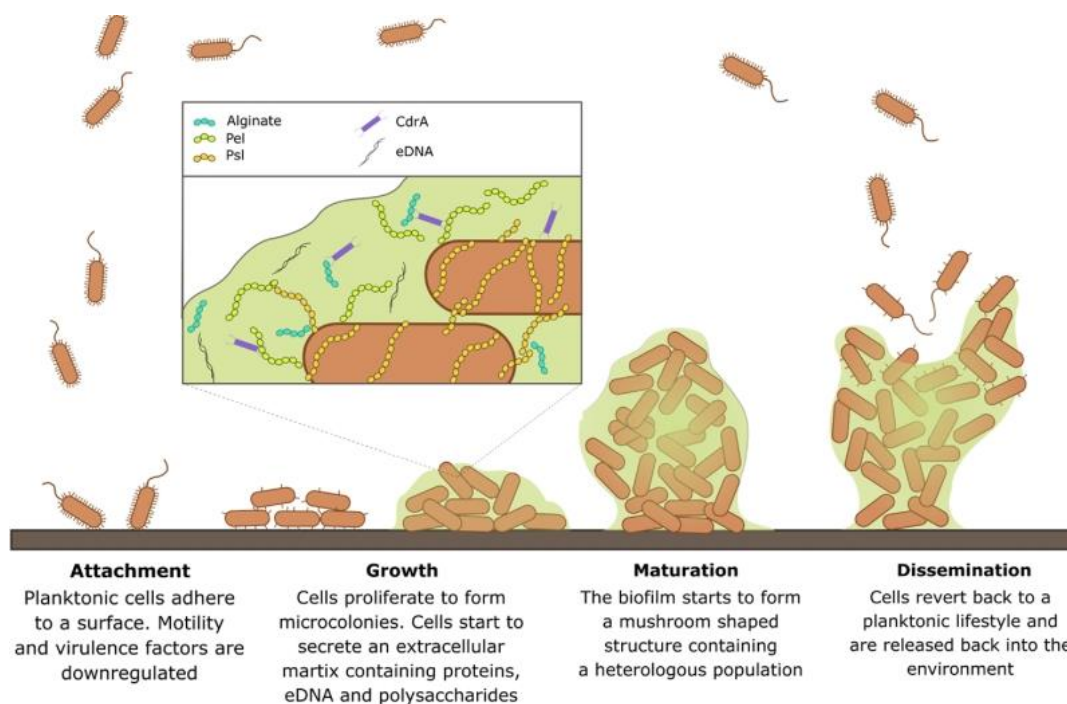


*Figure 23. Schematic representation of the biofilm formation steps [101].*

It only takes a few adherent bacteria to attach to the implant surface, grow and multiply to form a biofilm (**Figure 24**). Once established, biofilms are highly resistant to the immune system and conventional drugs, such as antibiotics, and may also spread and infect other tissues. The infections derived from biofilm formation on implants surfaces affects patient morbidity and even results in death in severe cases [3].

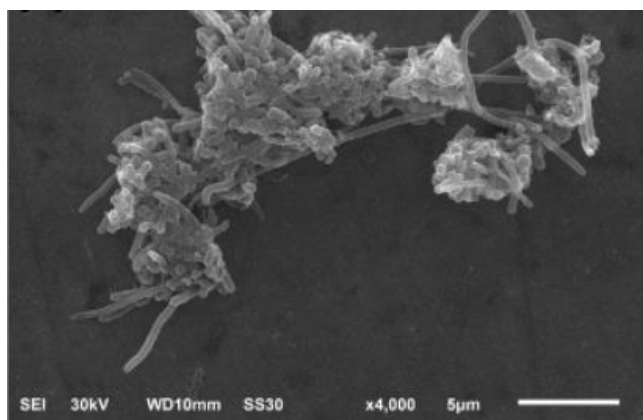


*Figure 24. Scanning electron microscopy (SEM) micrograph depicting a developed biofilm in a zirconia sample [102].*

Within the oral cavity, the mouth, being a humid environment with a practically constant temperature of 36 °C, is the perfect ecosystem for the bacterial microflora. Teeth, crown, dental prostheses and endosseous implants provide a surface to form the biofilm, which can lead to dental pathologies and ultimate implant failure.

One factor that influences the bacterial adhesion process is the biomaterial used. Zirconia has been proved to be satisfactory since it reduces plaque formation on the implant surface, and consequently, leads to good healing and successful implant treatment [103] [104]. Furthermore, when compared to titanium, zirconia implants have shown less bacterial adhesion. Scarano *et al.* [105] investigated the bacterial adhesion of titanium and zirconium oxide and reported a degree of surface coverage by bacteria of 12.1 % on zirconia compared to 19.3 % on titanium. Rimondini *et al.* [106] confirmed these results with an *in vivo* study, in which Y-TZP accumulated fewer bacteria than titanium in terms of the total number of bacteria and the presence of potential putative pathogens.

The adhesion process is not only dependent on the type of biomaterial used but also on the material surface roughness and wettability. This will be discussed in the next subsection.

#### **1.1.10. Influence of the surface properties on implant-tissue response**

The interaction between the implant and the surrounding tissue depends on the characteristics of the implant surface. In particular, the surface characteristics that influence the process of osseointegration include surface chemistry (e.g. chemical composition), topography (e.g. roughness), wettability and surface energy, surface charge and potential, and the crystal structure [107]. Among these, surface wettability and free surface energy, as well as surface roughness, are considered to be crucial [21]. However, such surface properties (specially wettability and surface roughness) are also known to affect bacterial adhesion and biofilm formation [3]. Hence, one of the main challenges in the design of an implant surface is to effectively promote tissue integration without favouring biofilm formation.

Thus, a brief discussion of the influence of surface roughness and wettability on both osseointegration and bacterial adhesion is presented hereunder.

##### **1.1.10.1. Roughness**

In terms of cellular response, many studies have proven that increasing the average surface roughness (Sa) values of implant materials favours the interaction between bone cells and the surfaces, accelerating and increasing the quality of bone to implant contact (BIC) [108]–[112]. This is because textured implant surfaces provide cells with broader adhesion areas (i.e. to establish focal adhesion contacts and subsequent mechanotransduction) and irregularities that allow a better fit and mechanical interlocking, which at the end favour the osseointegration process [113].

Since roughness is a scale-dependent parameter, when referring to implants the authors usually distinguish micro-roughness (roughness at the micrometric length scale) from nano-roughness (roughness at the nanometric scale). In this regard, researchers have proven that each topographical scale influence tissue response at a different level (**Figure 25**). On the one hand, micro-surface roughness attempts to enhance the osteoconduction (in-migration of new bone) through changes in surface topography, and osteoinduction (new bone differentiation) along the implant surface by utilizing implant as a vehicle for local delivery of bioactive agents [114]. Lossdörfer *et al.* [115] and Boyan *et al.* [116] also reported that implant micro-roughness enhanced osteoblast differentiation while decreasing osteoclast formation and activity, which may be related to altered attachment to the surface. Besides, it has been demonstrated that there exists an optimal range in the micrometre scale since moderately average surface roughness ( $S_a$  between 1.0 and 2.0 micron) show stronger bone responses than smoother or rougher surfaces [110] [117]. On the other hand, nanometer length-scale modification can also influence cell behaviour. Several *in vitro* [118]–[120] and *in vivo* [121] [122] experiments have demonstrated higher osteoblast attachment and proliferation and stronger bone tissue incorporation when implants are provided with nanostructures. Moreover, nanotopographies have also been shown capable of stimulating the differentiation of mesenchymal stem cells into the osteoblastic lineage [3].

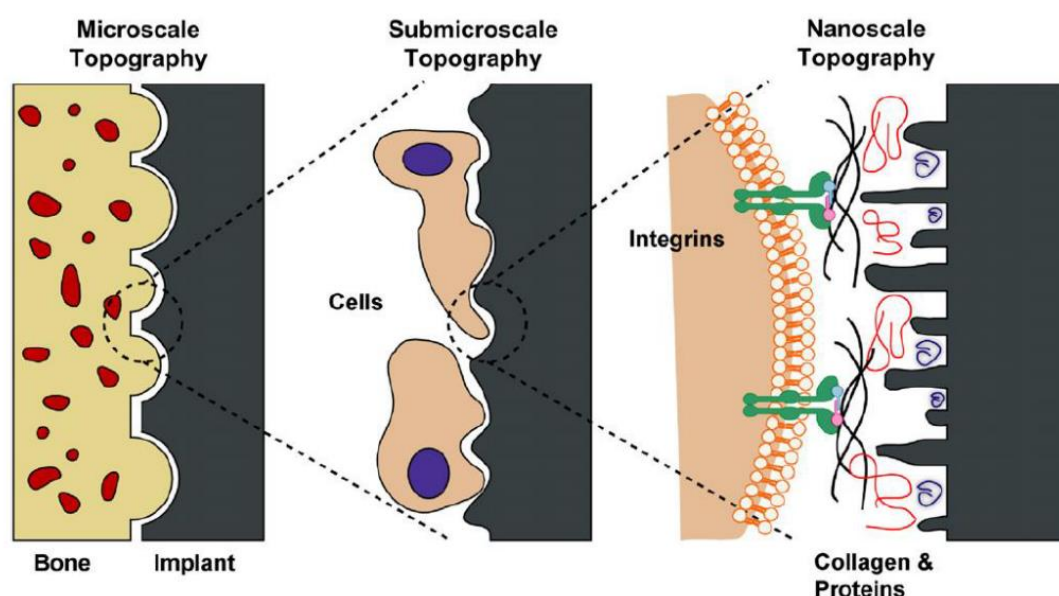


**Figure 25.** Schematic of the interactions between bone and the implant surface at different topographical scales [21].

However, the roughness of the substrate is also known to play a significant role in bacterial attachment and biofilm formation. For instance, Lorenzetti *et al.* [123] demonstrated that microscopic roughness increased the interaction surface between bacterium and substrate, resulting in an “interlocking”

effect and undesired high bacterial adhesion. Mitik-Dineva *et al.* [124] reported that the number of bacteria adhering to the etched nanoscale surface was observed to increase by a factor of three. Yu *et al.* [125] also suggested that nanoscale surface roughness of zirconia influenced initial bacterial adhesion force and early attachment.

#### **1.1.10.2. Wettability**

The surface wettability or hydrophilicity of implants is another property that is considered as one of the key factors controlling the adsorption and interaction of proteins with the implant surfaces and subsequent cell adhesion [126]. This physicochemical parameter can be quantified by the value of the water contact angle (CA). A surface with a CA of less than 90° is considered hydrophilic and if the CA is equal or close to 0°, it is considered as a super-hydrophilic surface. On the contrary, a hydrophobic surface is defined when the value of CA is more than 90° [127].

The wettability of implants is influenced by both surface topography (roughness) and chemistry (chemical groups on the surface, e.g. hydroxyl groups). It has been demonstrated that hydrophilic surfaces favour the osseointegration process by improving the surface reactivity with the surrounding ions, amino acids, and proteins [128]–[130]. Those effects are supported by improvements in the BIC and bone anchorage during bone healing in the early stages [131].

### ***Surface modification of zirconia-based ceramics***

As discussed in the previous section, the surface properties of the implant strongly influence the biological response of the tissue. Alterations of the surface topography and in the physicochemical properties play an important role in regulating bacterial infection, inflammation and bone formation [69]. Hence, various surface modification approaches have been investigated to modify the surface properties of zirconia implants, to promote osseointegration and limit infections. Nevertheless, ceramics materials are sensitive to any surface alteration [132]. Surface modification can induce surface defects, which strongly influence the mechanical properties, and in the particular case of zirconia-based ceramics, it can promote the ageing phenomenon. Therefore, special attention must be placed on properties on the material after the surface modification procedure.

Accordingly, the present section gives an overview of the current surface modification techniques that have been used to enhance the osseointegration behaviour of zirconia-based ceramics implants. Studies about their impact on mechanical reliability are also added (when documented).

### 1.1.11. Grinding/polishing process

Grinding and polishing process is part of the typical processing route of implants. The grinding process removes saw marks and cleans the specimen surface; and subsequently, polishing is used to remove the damage induced by the abrasive particles of the grinding papers [133], as shown in **Figure 26**. Grinding significantly increases the roughness, whereas appropriate polishing can result in smooth surfaces [134].

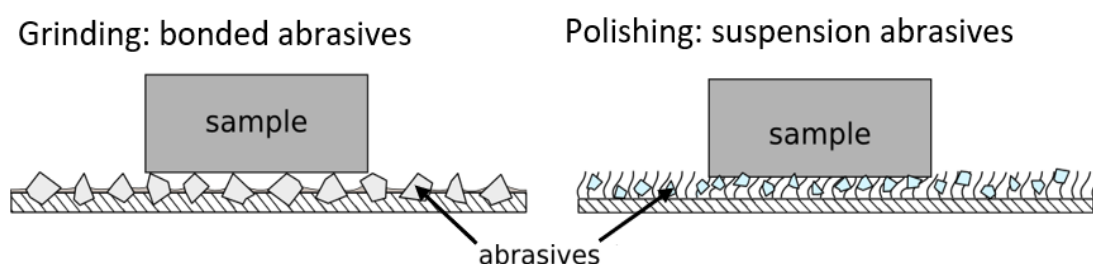


**Figure 26.** Schematic representation of grinding (left) and polishing processes (right) [135].

Grinding/ polishing is one of the oldest surface modification methods. Its **principal advantage** is that it is easy to implement which allows controlling the surface topography to some extent, by monitoring the processing conditions of grinding/polishing (i.e. grit size, speed, etc.). Moreover, it is possible to provide the surface with directional patterns. By contrast, the surface pattern complexity that could be achieved by grinding is limited and more time-consuming when compared with other techniques as laser patterning. Besides, another **major issue** of grinding/polishing is that it is known to affect the properties of zirconia: *it induces changes on the surface (roughness, microstructural modification, residual compressive stresses, cracks, texture, etc.)*, which consequently, may modify the mechanical properties, ageing behaviour and cellular behaviour of the material [136].

Regarding the cellular response of grinded/polished zirconia, Minguela *et al.* [137] investigated the influence of surface topography on the adhesion, proliferation and differentiation of osteoblastic cells. They prepared samples with a range of topographies by combining different roughness and directionalities (**Figure 27**). The results indicated that above certain roughness level ( $S_a = 150$  nm), only when combined with unidirectionally oriented patterns, cell alignment and attachment was favoured. Despite more research in zirconia is needed, previous data reported a similar effect on ground titanium surfaces [138], where  $S_a = 150$  nm showed the optimal cell adhesion behaviour.



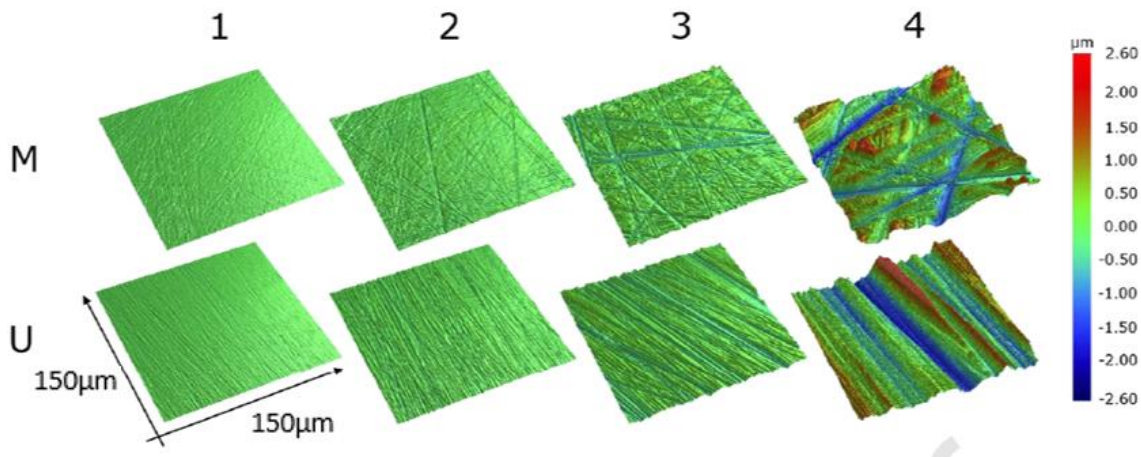


**Figure 27.** WLI topographical images of the specimens after grinding surface modification., which in increasing levels of roughness (from 1 to 4). Multidirectional (M) and unidirectional (U) patterns are displayed [137].

Minguela *et al.* [137] also studied the mechanical response and ageing behaviour of Y-TZP after grinding/polishing. The obtained results demonstrated that the changes induced by grinding/polishing procedures can improve surface mechanical properties, in particular apparent indentation fracture toughness. This property is slightly higher in rougher samples, due to the  $t \rightarrow m$  phase transformation induced during the process. By contrast, regarding the ageing behaviour, they found that coarse grinding accelerated ageing. Instead, the samples that presented intermediate roughness ( $S_a = 16\text{nm}$ ) displayed an excellent ageing resistance due to the recrystallization of the grains. Similarly, Lai *et al.* [139] reported small-grit grinding improved the strength and ageing resistance of Y-TZP dental zirconia material. Thus, the processing conditions (grit size, speed, etc.) should be chosen carefully to avoid damage and ensure implant reliability.

#### 1.1.12. Sandblasting

Sandblasting, also known as airborne particle abrasion, is a process of impinging a stream of particles on to a target surface with pressure, see **Figure 28**. The operating principle consists of particles flowing with the air speed through a nozzle and hitting the target surface from some distance. The immediate consequence of sandblasting is the erosion of the material due to the impact of the particles (usually alumina), which produces a surface with micro-roughness. Several parameters affect the roughness on the implant surface, mostly particle size, shape, and kinetic energy [61].

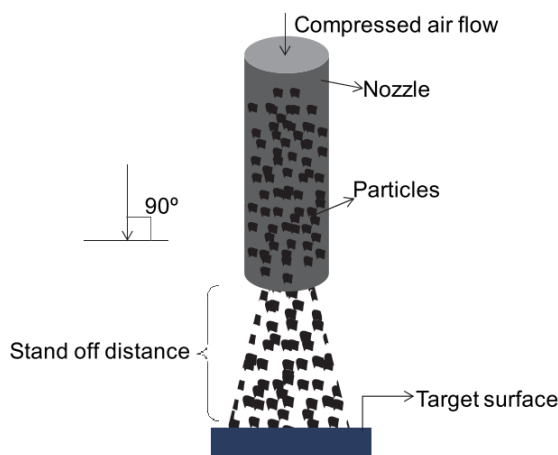


Figure 28. Schematic representation of the sandblasting process [61].

The **key strength** of sandblasting is the possibility of performing a homogeneous and gentle anisotropic abrasion on hard materials such as ceramics or glass (see **Figure 29**). However, the **drawback** of this technique is that it could slightly alter the surface chemistry due to inevitable  $\text{Al}_2\text{O}_3$  contamination. However, this can be overcome by chemical etching treatment (more information is available in **section 1.1.13**), which has been proven to remove alumina residues resulting from sandblasting [140].

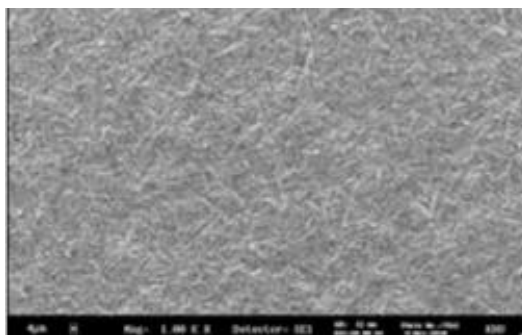


Figure 29. SEM micrographs of zirconia after sandblasting process (magnification x1000). A:  $50\ \mu\text{m}\ \text{Al}_2\text{O}_3$  sandblasting, B:  $110\ \mu\text{m}\ \text{Al}_2\text{O}_3$  sandblasting. [141]

Sandblasting is one of the most commonly used surface treatments in zirconia-based implants. It is mostly used to increase surface roughness and favour the osseointegration process [61]. Moreover, Bacchelli *et al.* [142] and Gahlert *et al.* [143] have reported that sandblasting zirconia implants surfaces significantly improved the peri-implant osteogenesis and osseointegration when compared to machined titanium surfaces.

Regarding mechanical properties, Hallmann *et al.* [144] evaluated the effect of different blasting pressures and airborne particle composition and size on phase transformation and surface morphological change of Y-TZP. The results showed higher pressure and particle size led to more



extensive  $t \rightarrow m$  phase transformation as well as increased surface roughness. They concluded that alumina particles of 50 or 110  $\mu\text{m}$  at pressures of 2.5 or 1.5 bar, respectively, were the optimal conditions to reduce the surface defects of Y-TZP ceramic. Furthermore, Kosmac *et al.* [145] obtained that with adequate sandblasting parameters the compressive residual stresses induced by the process can lead to an increase in flexural strength.

However, sandblasting may harm the microstructure of zirconia leading to initial transformation of zirconia surface from the tetragonal to the  $m$ -phase and thereby reducing the resistance to low thermal degradation. In 2008, Kosmac *et al.* [146] investigated the effect of sandblasting on ageing and fatigue behaviour of Y-TZP. In dry conditions, sandblasting resulted in surface strengthening and substantially higher survival rate under cyclic loading. By contrast, when tested in artificial saliva, the survival-strength lowered 10 - 15 %, implying that stress-assisted corrosion plays an important role in the fatigue behaviour of dental zirconia. More recent studies have found an increased resistance to the ageing of zirconia, which is attributed to the recrystallization of the monoclinic grains of the surface into tetragonal nanograins after the treatment [147] [148].

### 1.1.13. Chemical etching

Chemical etching is a surface treatment where baths of temperature-regulated etching chemicals are used to remove material from the surface. It is usually followed by a heat treatment that helps to smoothen the sharp edges caused by the etching process. Acid etching can be performed by hydrofluoric acid (HF), nitric acid ( $\text{HNO}_3$ ), or sulfuric acid ( $\text{H}_2\text{SO}_4$ ) [5]. Chemical etching can induce surface roughness values down to the nanoscale, which is why it is often combined with micro-roughening treatments (e.g., sandblasting) [15].

The **main advantage** of using chemical etching is that, regardless of the material's shape and size, homogenous surface roughening is obtained. Also, the treatment does not induce any stress on the material, so there is no risk of delamination. However, its main **drawback** is it may cause undesirable chemical changes in the surface of the material [140].

The topography formed after the acid etching treatment depends on the composition of the type of acid used and its composition, temperature, and etching time [15]. Flamant *et al.* [149] assessed the effect of HF concentration (5, 10 and 40 %) and etching times of 30min, 1 and 2h on the surface topography of 3Y-TZP. The experimental results showed that a concentration of 40 % leads to the fastest and most uniform etching, and therefore, the most appropriate conditions for the treatment of zirconia dental implants (see **Figure 30**). Similarly, Oh *et al.* [150] also tested HF in two diluted concentrations (10 and 20 %) and in different etching times (1, 2, 10, and 60min) on pure zirconia and

other zirconia-based materials. The results obtained indicated that, in the case of zirconia, the roughness was not affected by those etching times and HF concentrations.

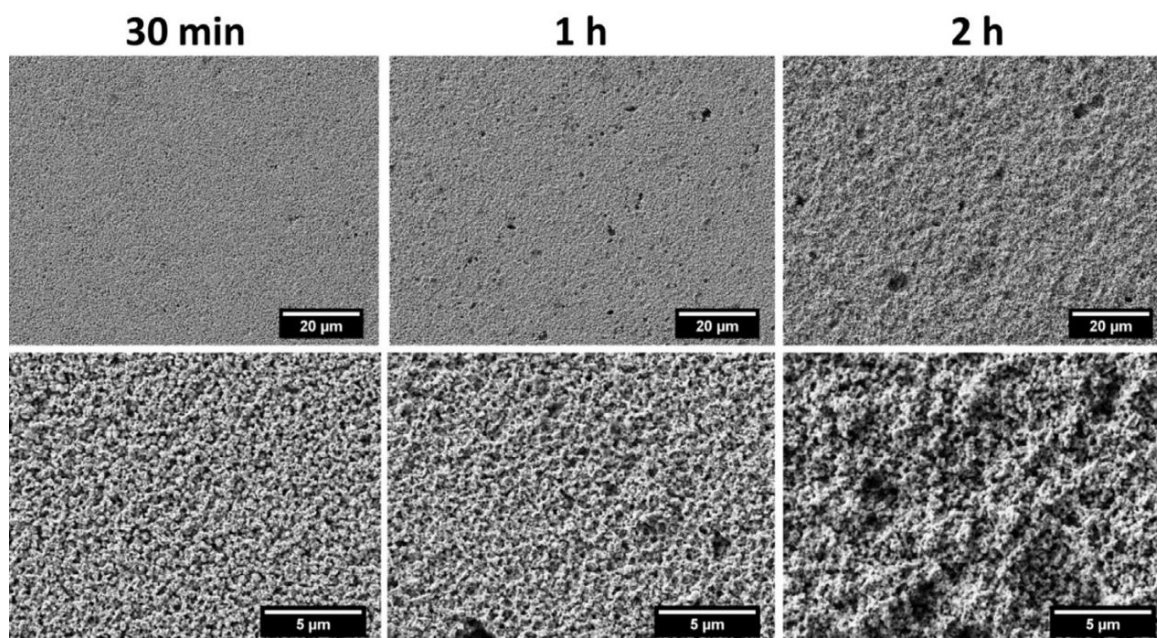


**Figure 30.** SEM micrographs of the surface at different magnifications and for different etching times in HF 40 % [149].  
Low magnification on top, high magnification on the bottom.

The most promising etching reagent for zirconia implants is HF since it presents the advantage to be a fast etchant at room temperature. Besides, the incorporation of fluoride at the surface could enhance osteoblastic differentiation and interfacial bone formation and inhibit bacterial growth, as it does for titanium [151] [152]. Additionally, as previously mentioned, chemical etching can be successfully associated with micro-roughness treatments, as sandblasting. The combination of both surface treatments enhanced the osseointegration. In this sense, Ito *et al.* [153] showed that the combination of sandblasting with chemical etching treatments with HF leads to an increase in the proliferation rate and expression of ALP activity of osteoblast-like cells (MC3T3-E1); Bergemann *et al.* [154] found that it enhanced the human primary osteoblast maturation, and Saulacic *et al.* [155] showed that acid etching but not alkaline etching of sandblasted zirconia increased bone-to-implant contact. Finally, there are even commercialized zirconia dental implants with an acid-etched surface (CeraRoot) which has shown similar or higher success rates compared to titanium implants after five years of follow-up [149].

Even though chemical etching surface treatment has provided surface topography and biological advantages, the long-term reliability of acid-etched dental zirconia also must be assessed. Regarding the mechanical properties, Flamant *et al.* [156] investigated the effect of HF etching on flexural strength and ageing behaviour of Y-TZP. They used HF (40%) and times up to 2h. The results showed no sign of ageing in any case, and there was no decrease in the biaxial strength for etching times below

1h. Accordingly, they concluded that dental zirconia etched with HF (40%) should be reliable for long-term implantations provided that the etching duration does not exceed one hour. Moreover, Xie *et al.* [157] also evaluated the effect of acid treatment on dental zirconia, but on this study, 5 and 40 % HF concentration and etching times between 2h and 5 days were tested. The results suggest that the adverse effects of HF are aggravated by higher concentrations: The flexural strength, surface finish, and surface Vickers hardness of Y-TZP were significantly deteriorated by immersion in 40 % HF, but not with the chemical etching in 5 % HF. Thus, from these two studies it can be summarized that: *(i) higher HF concentrations induces higher surface modification, and (ii) for HF 40% the immersion time must be lower than 1h.*

#### 1.1.14. Laser treatment

A laser is an electromagnetic source that, depending on the wavelength and intensity of the emitted radiation, causes different interactions with materials and can be exploited for diverse purposes. Low energy interactions are used as a source of information (spectroscopy techniques), while higher energies can lead to material modifications like phase change, microstructural modifications and thermal stresses inside the material. Therefore, laser treatment can be applied as a surface modification technique. Since the material response is very sensitive to laser beam characteristics, tuning this device parameters would result in very different material modifications. Laser parameters that influence the most are pulse duration, wavelength and fluence [21].

When using the laser to modify the surface of a material, the high energy pulse delivered maximum intensity position locally melts, evaporates and ablates the substrate. Thus, a distinct **advantage** of laser technology is that, unlike previous techniques, it allows the production of defined patterns (smaller than 100  $\mu\text{m}$ ) in a faster, more accurate, and easier way (**Figure 31**). Furthermore, since it is a non-contact technology there is no risk for surface contamination [140].

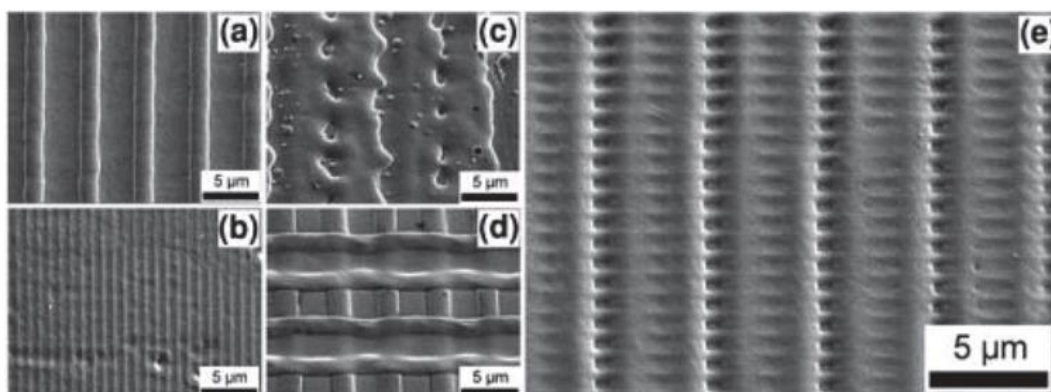


**Figure 31.** Periodic line (a-c), cross (d) and hierarchical patterns (e) fabricated on stainless steel and titanium. Different optical setup and laser parameters result in very different topographies [21].

By contrast, the **major problem** of laser treatment is that it can produce severe surface damage and microstructural or compositional modifications due to the thermal loads caused by laser-materials interaction [21]. As an example, Roitero *et al.* [158] characterized the microstructural changes and collateral damage induced by laser patterning of Y-TZP surface. The laser treatment generated a  $\sim 1\ \mu\text{m}$  thick heat affected zone where microcracking, directional recrystallization, and grain deformation took place. The study also revealed nanometric-size twins sign of the  $t \rightarrow m$  phase transformation (as depicted in **Figure 32**). It is therefore of paramount importance to evaluate the changes induced by the laser treatment.

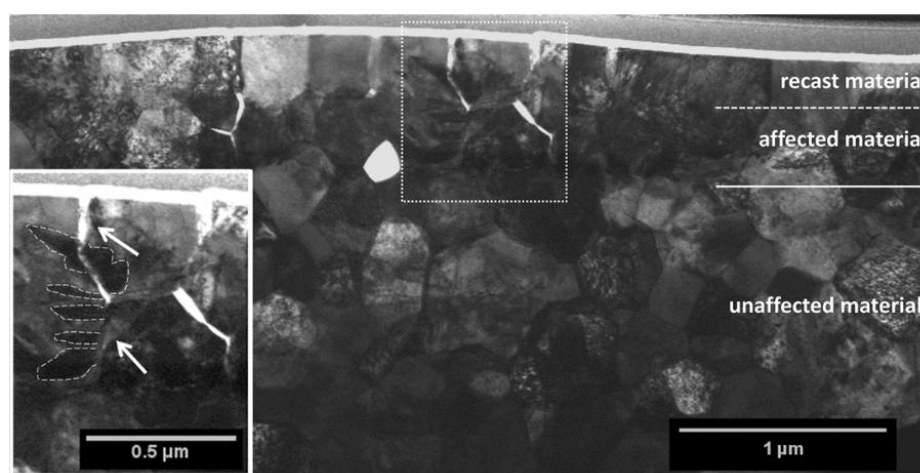


**Figure 32.** STEM micrograph of the region of material below a peak. A zoom of the region around a crack (square dash line) is depicted in the inset: twins (marked with dash lines) depart from crack (marked with arrows).

Laser surface processing in zirconia has gained interest due to its ability to improve material wettability by altering surface properties, which in turn plays a key role in determining cell adhesion [87,] [88]. Good osteoblast cell adhesion and other cellular responses have been observed in various studies of laser modified zirconia-based bioceramics with a defined micro-range geometry. As an example, Rezaei *et al.* [161] evaluated the osseointegration capability of hierarchically (meso-/micro- and nano-scale) roughened zirconia created by solid-state laser sculpting. All rough zirconia samples showed increased capability for bone-implant integration compared to machine-surfaced zirconia, which was associated with accelerated osteogenic differentiation and preserved attachment, spread, and proliferation of osteoblasts on the surface. Carvalho *et al.* [162] also used femtosecond laser ablation technique to develop strike-pattern roughened ATZ samples and evaluated its biological performance. The results indicated that cells adhered much stronger to roughened ATZ, and oriented accordingly to the surface micropatterns. Similarly, Stancius *et al.* [163] fabricated multi-patterned 3Y-TZP samples by femtosecond laser, but in this case, the patterns consisted of interspaced pits with a defined diameter (10, 20, 30  $\mu\text{m}$ ) and depth (3 and 9  $\mu\text{m}$ ). The results indicated that the pattern 30  $\mu\text{m}$  diameter/10  $\mu\text{m}$  depth pits patterns induced the strongest osteoblastic commitment compared to the machined and other patterned zirconia samples. Finally, Hoffmann *et al.* [164] compared the degree of early bone

apposition around various surfaces: (1) zirconia as sintered, (2) zirconia with laser-modified surface, (3) zirconia with sandblasted surface, and (4) titanium with an acid-etched surface. The study revealed a slightly higher bone apposition around the laser-modified zirconia surface in comparison to the others.

Laser patterning induces several microstructural modifications that may affect the mechanical properties and LTD resistance of dental zirconia. Parry *et al.* investigated the effect of nanosecond [165] and picosecond [166] pulse laser sources in Y-TZP and evaluated the impact on materials strength. Both cases resulted in a reduction in material strength. However, when comparing both cases, ns-machined samples showed a substantial reduction in strength as a result of the surface cracks introduced; while the ps-machined samples showed a much smaller strength reduction since no surface cracking was observed. Same way, Roitero *et al.* evaluated the mechanical properties [167] and ageing [168] of 3Y-TZP after laser patterning. Regarding the mechanical properties, they obtained a minor decrease in strength, hardness and elastic modulus. They also obtained a reduction in LTD resistance because of the presence of monoclinic phase and residual stresses, induced by the thermal shock during laser-material interaction. However, they proved that thermal treatment of 1h at 1200 °C anneals the affected microstructure and increase the resistance to LTD of laser patterned 3Y-TZP. Contrary, Daniel *et al.* [169] obtained an increase of flexural strength of laser-treated zirconia and alumina samples. In the study, the maximum efficiency was reached with a laser fluency around 500 mJ/cm<sup>2</sup> increasing the fluency strength by 50 and 40 % for zirconia and alumina samples, respectively.

The investigations mentioned in the paragraph above show contradictory results regarding the mechanical properties and LDT resistance of laser-modified dental zirconia. However, the laser parameters applied in each case slightly differ, indicating that they must be chosen carefully. Therefore, these studies emphasize the necessity of more complete microstructural and mechanical studies addressing the influence of the laser parameters on the reliability of zirconia material for dental applications.

### 1.1.15. Ultraviolet light treatment

Ultraviolet (UV) light is an electromagnetic radiation of shorter wavelength than visible light that is classified into four distinct spectral areas, according to the wavelength: *vacuum-UV* (100–200 nm), *UVC* (200–280 nm), *UVB* (280–315 nm), and *UVA* (315–400 nm). Within the biomedical field, the applications of UV light include sterilization, medical treatments, and surface modification of implants. Besides, the available UV sources used in biomedicine are light-emitting diodes, lasers, and microwave-generated UV plasma [170].

As a surface modification technique, UV light treatment has the **distinctive characteristic** of altering the physicochemical properties of the surface by inducing a photocatalytic activity, which at the same



time, enhances the bioactivity capability of the implant [171]. This phenomenon, termed “UV light-mediated photofunctionalization”, is characterized by the removal of hydrocarbons from the surface, the alteration of the surface electrostatic properties and the generation of hydrophilicity (or super hydrophilicity); and consequently can produce photo-induced biological effects as accelerated and enhanced protein absorption and cell attachment [172]. The photocatalytic effect on UV-treated zirconia implants has been widely investigated, and several studies have reported the decreased amount of surface carbon and the generation of super hydrophilic zirconia after UV treatment [173]–[176]. The increased bioactivity of UV light treated zirconia has also been confirmed: Tuna *et al.* [173] showed that UV light pre-treatment of zirconia surfaces augmented primary human alveolar bone osteoblasts (PhABO) cell attachment and spreading after 24h (see **Figure 33**); and Att *et al.* [175] concluded that UV treatment enhanced the bioactivity of 3Y-TPZ on osteoblasts, in terms of their attachment, proliferation, and mineralization.

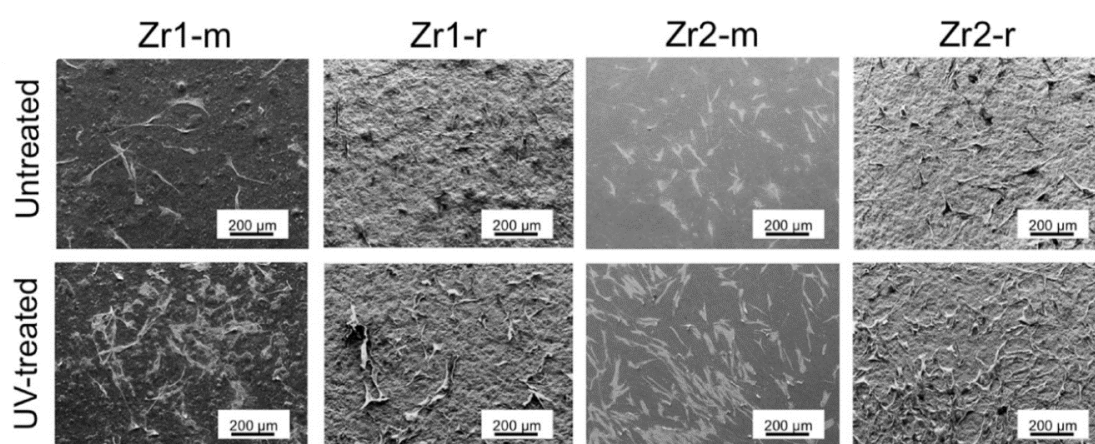


**Figure 33.** Morphology, attachment and spreading of osteoblasts on zirconia discs after UV treatment. Representative scanning electron microscope images showing that after 24h cell number of PhABO on UV-treated surfaces is constantly higher compared to untreated surfaces. Zr1 and Zr2 represent the two biomedical grade zirconia used with smooth (m) or roughened (r) surfaces [173].

It is important to highlight that photofunctionalization and its induced biological effects depend on the UV-light properties as wavelength, intensity and exposure time. In particular, UV light wavelength plays an important role: a wavelength of approximately 360 nm is needed to induce the photocatalytic activity of zirconia, while a lower range wavelength at around 250 nm is of interest for the direct decomposition of hydrocarbons [172]. Those values correlate with the study performed by Tuna *et al.* [177], where they demonstrated that a mixed-wavelength of 360 and 250 nm for as little as 15 min can accelerate healing and increase bone-to-zirconia implant contact. Similarly, Han *et al.* [178] investigated the effects of UV irradiation on zirconia after UV-A (365 nm) or UV-C (243 nm) photofunctionalization for different times (15 min, 3 and 24h). The results showed improved proliferation and differentiation after UV-C irradiation on dental zirconia for 24h. However, in that study, they also observed significant colour change from white to yellow in UV-C treated zirconia. The aesthetic properties were especially compromised in prolonged 14h UV-C treated zirconia sample.

Thus, this indicates that the colour change induced on zirconia after the treatment is one of the **major problems** associated with UV light surface modification technique.

Furthermore, UV light treatment does not induce any changes in the topographic appearance [173], [174], meaning that it could be considered an easy approach to maximize the osseointegration capacity of zirconia without altering the topography, roughness or other morphological features of the implant. However, some studies indicated that not introducing any roughness can be a **disadvantage** over other techniques when analysing the osseointegration capability of the treated samples. As an example, Shalaby *et al.* [126] evaluated the influence of laser and ultraviolet surface modification strategies to enhance osseointegration of zirconia implants and revealed superior osseointegration for the laser modified implants. They attributed this observation to the highest roughness and enhanced surface wettability obtained in laser irradiated samples, while UV altered zirconia surfaces reflected the highest wettability but non-significant surfaces topographical modification. Similarly, Iinuma *et al.* [179] investigated the tissue response to zirconia implant surfaces treated with UV, a combination of large-grit sandblasting and HF acid etching (blastedHF), and a combination of blastedHF and UV (blastedHF+UV). They obtained significantly higher BIC ratio for blastedHF and blastedHF+UV compared to non-treated controls and UV-treated implants. Therefore, to maximize the osseointegration, it is preferable to use the UV light treatment in combination with other treatments that increase the roughness of the surface.

Finally, although UV light technique might provide a promising alternative to other methods, the influence of UV light modification to the mechanical properties of zirconia has not been investigated yet, so further research is needed to understand and to evaluate the risk of such a technique.

#### **1.1.16. Coatings**

Surface coating stands out as one of the best strategies to improve the biological and mechanical properties of implants. In this regard, many coatings on zirconia surfaces have been developed to enhance their biocompatibility, antibacterial potential, bioactivity, surface hardness/wear resistance, and fatigue properties [180].

The coating technique has the **advantage** of being able to introduce changes on both physical and chemical properties of the surface (see **Figure 34**). On one side, it can modify the surface topography by increasing the roughness to enhance the micro-mechanical interlocking and cellular response. On the other side, it can alter the surface chemistry to activate the surface toward the adhesion to other materials and enhance the biological activity to implant fixation [181]. By contrast, a **general limitation** related to coatings is the poor adherence to the substrate and the associated residual stresses that may provoke delamination.

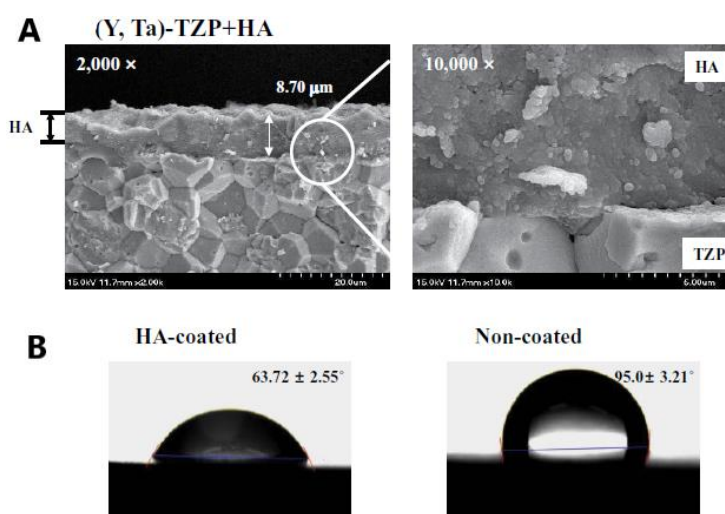


**Figure 34.** (A) Surface analysis of hydroxyapatite (HA)-coated zirconia. SEM Images are magnified 2,000× (left) and 10,000× (right). (B) The contact angle between the water drop and the substratum: (a) HA-coated zirconia surface and (b) non-coated zirconia surface [182].

For a coating to achieve its intended functions successfully, several factors must be considered: the deposition method, the coating material, the properties of the coated film (thickness, porosity, and surface topography) [183]. Regarding the thickness of the film, thin coatings are preferable for two main reasons: (i) *thin coatings adhere much more strongly to the substrate than thicker coatings*, and (ii) *in case of rapid dissolution of the coating, the use of ultrathin coatings prevents the implants from loosening* [184]. Also, microtopography with pores are known to allow easy penetration of bone-forming cells, and attachment and proliferation of vascularized new bone, thus providing a strong and durable implant-bone interaction [185].

Moreover, the deposition method significantly affects the physical and chemical properties and, consequently, the biological response of the implant. Some of the most effective methods for producing a bioactive coating on implants surfaces are plasma spraying, electrodeposition, sol-gel method, Physical Vapor Deposition (PVD), Chemical Vapor deposition (CVD) and aerosol deposition. A summary of the advantages and disadvantages of each process related to osseointegration is shown in **Table 3**.

**Table 3.** A critical assessment of microstructured and nanostructured deposition techniques [186] [187].

Process	Advantages	Disadvantages
Plasma spray	<ul style="list-style-type: none"> <li>i. High deposition rate</li> <li>ii. Low cost</li> <li>iii. Wide range of coating materials</li> </ul>	<ul style="list-style-type: none"> <li>i. High concentration of amorphous coating and residual stress</li> <li>ii. Weak adhesion between the substrate and the coating</li> <li>iii. Difficulty coating complex components</li> </ul>



<b>Electrodeposition</b>	<ul style="list-style-type: none"> <li>i. High deposition rate</li> <li>ii. Ability to coat complex substrates</li> <li>iii. Controlled nanostructured and microstructured coatings</li> </ul>	Caustic waste
<b>Sol-Gel</b>	<ul style="list-style-type: none"> <li>i. Controlled composition and homogeneity</li> <li>ii. Uniform coating</li> <li>iii. Great adhesion power on a complex substrate</li> </ul>	Due to the difference in thermal expansion coefficient (CTE) between substrate and coating, post heat treatment introduces internal stress
<b>PVD (thermal)</b>	Dense coatings of nanoscale thickness	<ul style="list-style-type: none"> <li>i. Difficulty coating complex components</li> <li>ii. Difficulty producing nanoporous coatings</li> </ul>
<b>PVD (sputter)</b>	<ul style="list-style-type: none"> <li>i. Ability to coat complex components</li> <li>ii. Uniform coating</li> </ul>	<ul style="list-style-type: none"> <li>iii. High cost</li> <li>iv. Low deposition rate</li> </ul>
<b>CVD</b>	<ul style="list-style-type: none"> <li>i. Ability to coat complex components</li> <li>ii. Uniform coating</li> </ul>	<ul style="list-style-type: none"> <li>iii. High-temperature process</li> <li>iv. Use of volatile gases</li> <li>v. Limited coating composition</li> </ul>
<b>Aerosol deposition</b>	<ul style="list-style-type: none"> <li>i. Low cost</li> <li>ii. Manufacturing of nanoporous and nanostructured coating</li> </ul>	Very low deposition efficiency

The coating material also plays an important role in the integration between the bone tissue and the implant. One approach is to deposit a coating of the same substrate material (zirconia, in this case) with a porosity that promotes osseointegration. Nevertheless, porosity can decrease the mechanical properties and ageing resistance of zirconia [15]. A second approach is to coat the implant with a bioactive material that promotes cell attachment, differentiation and induces hydroxyapatite (HA) formation. In literature, different bioactive coating materials have been used on zirconia, such as HA, bioactive glass (BG), and dopamine, between others [180].

- **Hydroxyapatite:**

Hydroxyapatite (HA) is the most widely used biomaterial in implant coating due to its chemical similarity to human bone and teeth [181]. Numerous studies have reported the bioactive properties of HA favouring osseointegration [188]–[191]. To this end, several methods have been studied for coating HA on implants (plasma-spraying, electrodeposition, magnetron sputtering, aerosol deposition). Even though most of the investigations refer to HA-coated metallic implants, there are few about zirconia implants. For example, Cho *et al.* [182]

evaluated the *in vitro* osteogenic potential of HA-coated zirconia by an aerosol deposition method, where the result suggested favoured osteogenesis when compared to non-coated zirconia.

- **Bioactive glass:**

Bioactive glass (BG), a silicate-based glass of composition  $\text{SiO}_2\text{-CaO-P}_2\text{O}_5$ , has been reported to be able to bond to tissue cells by the formation of a HA surface layer [181]. Because of their great bioactivity, “Bioglasses” are one of the best coating materials for improved osseointegration of metallic [192], [193] and ceramic implants [194]–[196]. Also, several techniques have been used for bioactive glass coatings, including sol-gel, plasma spraying, and electrophoretic deposition.

As mentioned above, however, a major concern is the adhesion strength between the coating and the substrate. In this field, Lung *et al.* [197] evaluated the bond strength of sol-gel coated silica after different deposition times and compared against the sandblasting method. They obtained an increase of the shear bond strength with the deposition time, but in all cases, it was lower when compared to the sandblasting technique.

- **Polydopamine:**

Dopamine, the precursor of 3,4-dihydroxy-L-phenylalanine (L-DOPA), is an important component in the adhesive structure of mussels that have inspired a new simple approach to surface coating [140]. The technique is based on the self-polymerization capacity of dopamine, where a thin coating can be achieved by dipping the substrate in a dopamine solution [198].

Because L-DOPA coating does not require a complex procedure, is solvent-free and non-toxic, it is particularly suitable for biomaterial application. As bioactive coating, it has been demonstrated that it decreases significantly the bacterial activity and enhances fibroblasts adherence, accelerating biological processes such as osseointegration [180]. In 2013, Liu *et al.* [199] studied for the first time L-DOPA coatings to improve the biocompatibility of  $\text{ZrO}_2$  and concluded that the coating improved osteoblast responses such as cell adhesion and cytoskeleton development. Lately, Liu *et al.* [198] also suggested that L-DOPA coating significantly reduced bacterial adhesion compared to uncoated zirconia (about 40% less).

## State of the art

In this section, a review on the current status of the most relevant topics of the project has been carried out, so the objectives of the Master's thesis can be defined further on. Besides, it summarizes the most relevant published papers that will be of great value for the discussion of the results.

In this Master's thesis, the main covered subjects are (i) *zirconia-based materials* (ii) *surface modification techniques and their impact on the mechanical properties and cellular response*, and (iii) *cell-material interactions and subsequent osseointegration*. To evaluate the relevance of these topics in the field and the interest this research project may have for the scientific community, the number of the articles available on zirconia, surface treatments and osseointegrations during the last two decades is represented in **Figure 35**, **Figure 36**, and **Figure 37**, respectively. The three graphs show an increase in the number of publications with each passing year, meaning that those topics are of great and increasing interest in the research field.

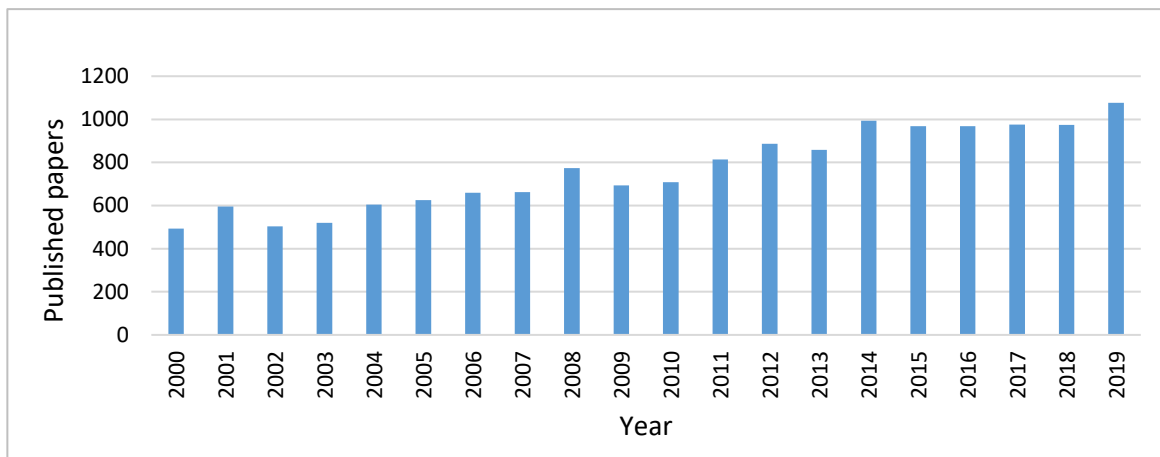


Figure 35. Number of articles published about zirconia over the last 20 years

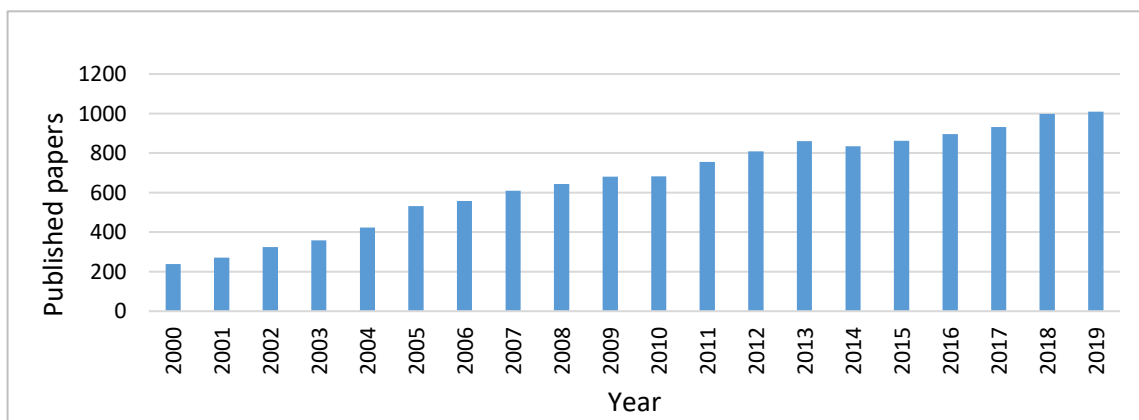
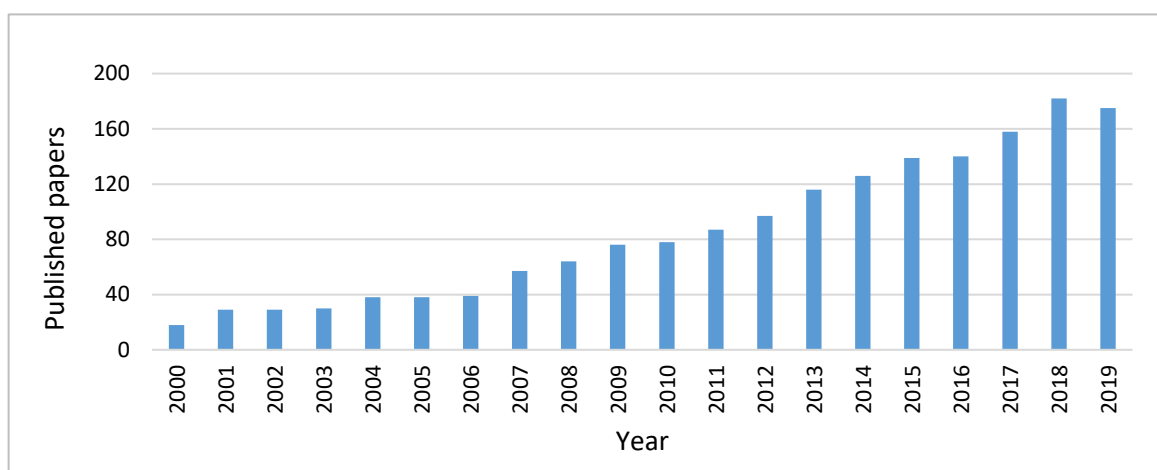
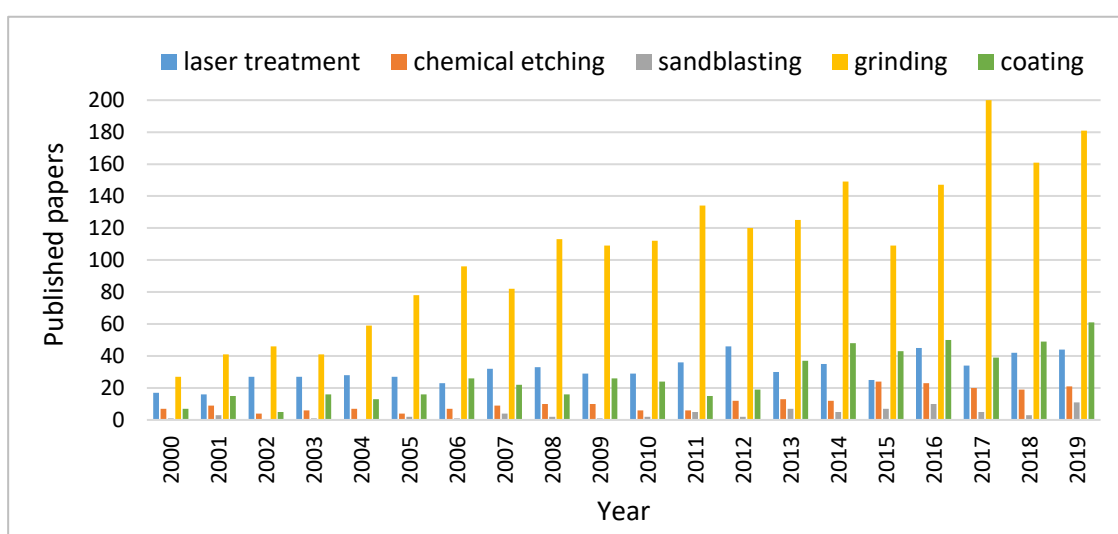


Figure 36. Number of articles published about surface modification over the last 20 years.



**Figure 37.** Number of articles published about osseointegration over the last 20 years.

Furthermore, **Figure 38** compares how the number of publications on various surface modification techniques has evolved over the last 20 years. It includes laser treatment, chemical etching, sandblasting, grinding, and coatings. A first remark to be made is that all the techniques show a more or less pronounced increasing tendency on the published paper with the years, which indicates that the surface modification of material is gaining attention among scientists. The reason for the great interest in this topic is that this approach allows for achieving improved surface characteristics, and therefore, it is possible to develop new applications of the modified materials. A second comment to be made on the graph is that grinding has been undoubtedly the most investigated technique. This may be because it is the most simple, costless and easy to implement one. However, new advances in technology in recent years may lead to the development and facilitate the implementation of the other surface modification methods.



**Figure 38.** Number of publications comparing the different surface modification techniques presented in **section 2.3** over the last 20 years.

Within this Master's project, laser treatment has been selected to be implemented in dental zirconia in order to improve its osseointegration capacity. Laser technique outstands from the rest since it can produce defined patterns on the sample surface in a fast and accurate way. This is of great interest because, as discussed above, it has been demonstrated that building topographical cues on material surfaces has significant influence on regulating cells behaviour, including cellular adhesion and differentiation [200]. Furthermore, it will be of great interest to combine it with chemical etching surface modification for introducing homogeneous roughness to the patterned surface at the nanometric scale. Nanometric-length scale modification is relevant because it can also trigger specific cellular phenomena as adhesion, spreading, proliferation, and differentiation [201]. In addition, chemical etching has been used in combination with other techniques such as sandblasting showing improved values of osseointegration of zirconia implants [153]–[155]. Nevertheless, to the best of our knowledge, there are no investigations reported in which chemical etching is combined with laser treatment, neither for zirconia, nor for any other material, highlighting the novelty of this project.

Based on the above, it has been considered of interest to investigate the cellular response on laser patterned zirconia to evaluate the potential osseointegration capability of the surfaces. Moreover, a posterior chemical etching would also be of great interest as future work. As mentioned above, these two treatments in zirconia have not been studied in combination. However, if these two surface modification techniques are analysed separately, there are publications reporting their positive influence in the osseointegration capability/cellular response on treated zirconia. In **Figure 39** are shown the number of publications regarding osseointegration of laser modified zirconia (blue) and chemical-etched zirconia (orange). In the graph, it can be seen that, even though in both cases most of the investigations are from the last decade, there are just a few publications dealing with this topic. This means that much more research is still necessary in the field.

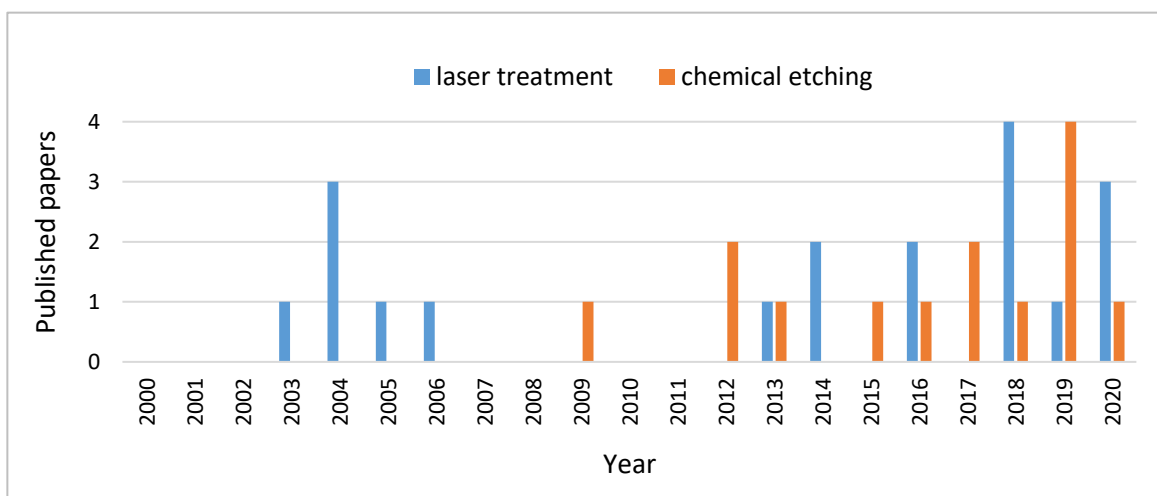


*Figure 39. Number of articles published in the last 20 years about cellular response to both laser-treated and chemical etched zirconia.*

Finally, **Table 4** presents the most relevant articles published about laser treatment and chemical etching of zirconia over the last 20 years, in which both the mechanical properties and cellular-response to the material had been evaluated. The treatment conditions and main results of those studies are summarized in the table, and represent a valuable information for the discussion of the results obtained in this Master Thesis.

Table 4. Summary of the most relevant articles related to this Master's thesis.

Ref	Material	Treatment	Conditions	Conclusion	
[149]	3Y-TZP	HF etching	<ul style="list-style-type: none"> <li>• 5, 10, 40%</li> <li>• 30min, 1h, 2h</li> </ul>	<b>Surface topography</b>	
				<ul style="list-style-type: none"> <li>• 40 % leads to the fastest and most uniform etching</li> <li>• High increase rate of <math>S_a</math> and <math>S_q</math> until one hour, and then became much lower (for HF 40%)                             <ul style="list-style-type: none"> <li>- <math>S_a</math> (30min) ~ 90nm, <math>S_a</math> (1h) ~ 200nm, <math>S_a</math> (2h) ~ 210nm.</li> <li>- <math>S_q</math> (30min) ~ 125nm, <math>S_q</math> (1h) ~ 300nm, <math>S_q</math> (2h) ~ 310nm</li> </ul> </li> </ul>	
[150]	Zirconia	HF etching	<ul style="list-style-type: none"> <li>• 10, 20%</li> <li>• 1min, 2min, 10min, 1h</li> </ul>	<b>Surface topography</b>	<b>Cellular study</b> (compared to polished)
				<ul style="list-style-type: none"> <li>• <b>Roughness:</b> not affected by the etching times or concentrations</li> </ul>	<ul style="list-style-type: none"> <li>• Osteoblast density (24h): + 10%</li> <li>• Flat and well-distributed osteoblast</li> </ul>
[153]	5Y-TZP	Sandb. + HF etching	<ul style="list-style-type: none"> <li>• HF: 46%</li> <li>• 15min</li> </ul>	<b>Surface topography</b>	<b>Cellular study</b> (compared to polished)
				<ul style="list-style-type: none"> <li>• <b>Roughness:</b> homogeneous (0.35<math>\mu</math>m)</li> <li>• <b>Wettability:</b> contact angle (50°)</li> </ul>	<ul style="list-style-type: none"> <li>• <b>Cell attachment</b> (3, 6h): similar</li> <li>• <b>Cell proliferation:</b> + 40% (7 days)</li> </ul>
[154]	Y-TZP	Sandb. + HF etching	<ul style="list-style-type: none"> <li>• HF: 40%</li> <li>• 1 hour</li> </ul>	<b>Surface topography</b>	<b>Cellular study</b> (compared to machined)
				<ul style="list-style-type: none"> <li>• <math>R_a</math> = 1.31 <math>\mu</math>m (SA+HF)</li> <li>• <math>R_a</math> = 0.59 <math>\mu</math>m (machined)</li> </ul>	<ul style="list-style-type: none"> <li>• <b>Cell area:</b> - 50% (24h)</li> <li>• <b>Cell adhesion:</b> High increase (24h)</li> </ul>
[156]	3Y-TZP	HF etching	<ul style="list-style-type: none"> <li>• <b>40HF30:</b> 40%, 30min</li> <li>• <b>40HF60:</b> 40%, 60min</li> <li>• <b>40HF120:</b> 40%, 120min</li> </ul>	<b>Mechanical properties</b>	
				<ul style="list-style-type: none"> <li>• Etching increases the %<i>m</i>-phase: HF40-30 (+15%), HF40-60 (+10%); HF40-120 (+23%)</li> <li>• Etching induces localized depth porous.</li> <li>• Etching induce average <b>strength</b> decrease: HF40-30 &amp; HF40-60 (-15%); HF40-120 (-29%)</li> </ul>	
				<b>Ageing</b>	
				<ul style="list-style-type: none"> <li>• The influence of etching in ageing is limited: <i>m</i>-phase increased the same as control.</li> <li>• <b>Strength</b> after ageing: control (-14%), HF40-30 (+0%), HF40-60 (+5%), HF40-120 (+20%)</li> </ul>	

Table 4. Summary of the most relevant articles related to this Master's thesis. (continuation)

[157]	Y-TZP	HF etching	<ul style="list-style-type: none"> <li>• <b>40HF0:</b> 40%, 2h</li> <li>• <b>40HF1:</b> 40%, 1 day</li> <li>• <b>40HF5:</b> 40%, 5 days</li> <li>• <b>5HF1:</b> 5%, 1 day</li> <li>• <b>5HF5:</b> 5%, 5 days</li> </ul>	<b>Roughness (<math>\mu\text{m}</math>)</b>	<b>Flexural strength (MPa)</b>	<b>H<sub>v</sub> (9.807N for 10s)</b>
				<ul style="list-style-type: none"> <li>• Control: 0.23</li> <li>• 40HF0: 0.44</li> <li>• 40HF1: 0.59</li> <li>• 40HF5: 1.15</li> <li>• 5HF1: 0.35</li> <li>• 5HF5: 0.26</li> </ul>	<ul style="list-style-type: none"> <li>• Control: 1232</li> <li>• 40HF0: 889</li> <li>• 40HF1: 694</li> <li>• 40HF5: 541</li> <li>• 5HF1: 1071</li> <li>• 5HF5: 1164</li> </ul>	<ul style="list-style-type: none"> <li>• Control: 1335</li> <li>• 40HF0: 1129</li> <li>• 40HF1: 1083</li> <li>• 40HF5: 1084</li> <li>• 5HF1: 1220</li> <li>• 5HF5: 1231</li> </ul>
[202]	ATZ	Laser patterns (Parallel lines)	Testing of different laser parameters	<b>Spirit laser</b> ( $\lambda = 1040\text{nm}$ , 100KHz, $v = 1\text{mm/s}$ and fluency ( $0.9, 1.8, 2.4 \text{ J/cm}^2$ ), $N = 1, 2, 5, 10$ )		
				<ul style="list-style-type: none"> <li>• By decreasing the number of pulses (N) the strike like pattern become a grooves structure.</li> <li>• By increasing the fluency, the patterning is more pronounced.</li> </ul>		
				<b>Femtosecond laser</b> ( $\lambda = 800\text{nm}$ , 1KHz, $v = 0.5\text{--}16 \text{ mm/s}$ and fluency ( $0.2 \text{ J/cm}^2$ ))		
				<ul style="list-style-type: none"> <li>• By decreasing the speed, the stripes pattern becomes more pronounced.</li> </ul>		
[161]	Y-TZP	Laser patterns (Parallel lines)	The laser introduced hierarchical scale roughness	<b>Roughness</b>	<b>Cellular study (compared to machined)</b>	
				meso ( $50 \mu\text{m}$ width, $6\text{--}8 \mu\text{m}$ depth) micro ( $1\text{--}10 \mu\text{m}$ width, $0.1\text{--}3 \mu\text{m}$ depth) nano ( $10\text{--}400\text{nm}$ widths, $10\text{--}300\text{nm}$ heights)	<ul style="list-style-type: none"> <li>• <b>Osteoblast proliferation (6, 24h):</b> similar</li> <li>• <b>Differentiation (6, 24 h):</b> 7-25 times higher</li> <li>• <b>Bone-implant integration:</b> 2.2 times higher</li> </ul>	
[162]	ATZ	Laser patterns (Parallel lines)	<ul style="list-style-type: none"> <li>• <b>Pulse width:</b> <math>875 \mu\text{s}</math></li> <li>• <b>Repetition:</b> 2 kHz</li> <li>• <b>Speed:</b> <math>1\text{mm/s}</math></li> </ul>	<b>Surface topography</b>	<b>Cellular study (compared to machined)</b>	
				<ul style="list-style-type: none"> <li>• Interspacing: <math>10 \mu\text{m}</math></li> <li>• Peak to valley distance: <math>2.6 \mu\text{m}</math></li> <li>• The laser-ablated nanogrooves: <math>R_a = 140\text{nm}</math></li> </ul>	<ul style="list-style-type: none"> <li>• <b>Cells adhered</b> much stronger to roughened ATZ</li> <li>• <b>Cell oriented</b> accordingly to micropatterns</li> </ul>	



**Table 4.** Summary of the most relevant articles related to this Master's thesis. (continuation)

[163]	3Y-TZP	Laser patterns (Interspaced pits)	<ul style="list-style-type: none"> <li>• 120fs, <math>\lambda = 795\text{nm}</math>, 1kHz</li> <li>• Diameter (10, 20, 30 <math>\mu\text{m}</math>)</li> <li>• Depth (3 and 9 <math>\mu\text{m}</math>)</li> </ul>	<b>Cellular study</b>		
				<ul style="list-style-type: none"> <li>• <b>Cell area:</b> the number of attached cells increased with the pits diameters</li> <li>• <b>Cell morphology:</b> more elongated cells for smaller diameters</li> <li>• <b>Cell distribution:</b> across pores (10 and 20<math>\mu\text{m}</math> diameter), inside pores (30<math>\mu\text{m}</math> diameter) 30<math>\mu\text{m}</math> diameter/10<math>\mu\text{m}</math> depth pits patterns showed the strongest osteoblastic commitment</li> </ul>		
[167]	3Y-TZP	Laser patterns (Parallel lines)	<ul style="list-style-type: none"> <li>• <b>Wavelength:</b> 532 nm</li> <li>• <b>Repetition rate:</b> 10 Hz</li> <li>• <b>Pulse duration:</b> 10 ns</li> <li>• <b>Fluence:</b> 4 J/cm<sup>2</sup></li> <li>• <b>Interspacing:</b> 10 <math>\mu\text{m}</math></li> </ul>	<b>Strength (MPa)</b>	<b>Hardness (GPa)</b>	<b>Elastic Modulus (GPa)</b>
				Control: 1347 Laser: 1190	Control: 17 (at 150nm penet.) Laser: 12 (at 150nm penet.) <i>*At deeper penetrations the value is similar</i>	Control: 250 (at 150 nm pen.) Laser: 220 (at 150 nm penet.) <i>*At deeper penetrations the value is similar</i>
[168]	3Y-TZP	Laser patterns (Parallel lines)	<ul style="list-style-type: none"> <li>• <b>Wavelength:</b> 532 nm</li> <li>• <b>Repetition rate:</b> 10 Hz</li> <li>• <b>Pulse duration:</b> 10 ns</li> <li>• <b>Fluence:</b> 4 J/cm<sup>2</sup></li> <li>• <b>Interspacing:</b> 10 <math>\mu\text{m}</math></li> </ul>	<b>Ageing</b>		
				<ul style="list-style-type: none"> <li>• Laser patterning decreased the LTD resistance</li> <li>• The laser introduced damage: <math>t \rightarrow m</math> transformation, microcracking, residual stresses</li> <li>• The initial monoclinic content augmented (+9%), but the transformation rate is reduced</li> <li>• An annealing treatment of 1 h at 1200 °C is recommended to ensure long-term stability</li> </ul>		
[137]	3Y-TZP	Grinding/polishing	Samples with increasing roughness and unidirectional patterns	<b>Roughness (<math>S_a</math>)</b>		
				<b>Control</b> = non-treated ; <b>U1</b> = 14 nm ; <b>U2</b> = 41 nm ; <b>U3</b> = 183 nm ; <b>U4</b> = 593 nm		
				<b>Hardness (GPa)</b>		
				<b>Control</b> = 12.8 ; <b>U1</b> = 13.1 ; <b>U2</b> = 13 ; <b>U3</b> = 13.3 ; <b>U4</b> = 13.2		
				<b>Fracture toughness (MPa·m<sup>1/2</sup>)</b>		
				<b>Control</b> = 4.8 ; <b>U1</b> = 4.9 ; <b>U2</b> = 5.3 ; <b>U3</b> = 5.5 ; <b>U4</b> = 6.2		
				<b>Ageing</b>		
				<ul style="list-style-type: none"> <li>• All grounded samples exhibited improved LTD resistance compared to the non-treated one</li> <li>• U2 and U3 showed the best result</li> </ul>		
				<b>Cellular study</b>		
				<ul style="list-style-type: none"> <li>• <b>Cell adhesion</b> slightly increased in the treated samples.</li> <li>• U3 and U4 produced <b>cell elongation and alignment</b> in the grinding direction.</li> </ul>		



## Objectives

The project is aimed at investigating ***the effect of different surface treatments on zirconia-based ceramic materials to promote bone cells adhesion and growth***. In this sense, the surface modification process will be conducted by using laser treatments to create defined topographical patterns at the micrometric length scale).

Within this context, this master's thesis can be divided into three different parts:

- i. The first part of the project is focused on the sample preparation by mean of laser-assisted treatments. Here in, a design of experiment (DOE) was planned in order to select the laser parameter that adequate better to the desired surface topography.
- ii. Subsequently on the characterization of the density (Archimedes), topography (Confocal laser scanning microscope, Atomic force microscopy, contact profilometry) and the hydrothermal degradation of the samples (RAMAN spectroscopy, XRD, Vickers indentation). These values will be compared with the reference zirconia-based ceramic material.
- iii. Finally, the study of the behaviour of osteoblast-like cells on the modified surfaces in terms of adhesion and proliferation. In order to investigate the effectiveness of the selected surface treatments, *in vitro* cellular assays will be performed on non-treated zirconia samples, laser modified samples, and laser-treated samples.

## Experimental methods

This section includes a clear and concise explanation about the materials and methods used during the project, with particular detail on how the experiments were carried out, thus ensuring, if required, they may be repeated with the highest reproducibility. The section is divided into five main subsections, which are: *Materials*, *Sample preparation*, *Surface treatments*, *Hydrothermal degradation*, *Cell culture* and *Characterization techniques*.

The chapter starts presenting the commercially available zirconia chosen for this project. That is followed by a step by step explanation of how the samples were prepared. The preparation was done by three steps: first, the conformation of the desired sample by using the cold isostatic pressing (CIP) technique; afterwards, the sintering of the obtained green bodies; and finally, the polishing process of the samples to obtain a smooth and of equal roughness surface on all samples.

The third subsection is a detailed explanation of the surface modification techniques used in the project, which is the laser treatment technique. The project aims to obtain samples with the desired pattern and roughness, so the cellular response (e.g. cell adhesion) can be enhanced. The obtained modified-surface highly depends on the parameters selected on the technique; therefore, special attention has been given to this part. In the case of the laser, the first step was to plan a Design of Experiments (DOE) to find out the optimum combination of the laser parameters. That is widely explained in **Annex A.1**.

Subsequently, the hydrothermal degradation condition are explained, as well as how the process was performed.

The next section focused on the characterization techniques used during the whole project. This includes the density calculation and topographical characterization of the laser-modified samples. Furthermore, the microstructural and mechanical characterization of the samples before and after the hydrothermal degradation was evaluated. Special attention has been given to the microstructure of the degraded and non-degraded samples, to determine if the phase transformation phenomenon has occurred. Also, it was of great interest to measure the hardness of both degraded and non-degraded samples to see the decrease in the mechanical properties. Finally, the cellular response to different patterns at different time-periods was evaluated by immunostaining and observation of the samples by fluorescence microscopy.

In the last part the procedure followed in the stage of cell culture is explained. Cell adhesion was studied after 6h of adhesion by mean of number of cells attached, focal adhesion, and actin filaments. Also, cell morphology and orientation was determined.

## Materials

Yttria stabilized polycrystalline zirconia powder with 3 mol. % of  $Y_2O_3$  (3Y-TZP) is the material chosen for this project. This material was provided by Tosoh (Tokyo, Japan) grade TZ-3YSB-E as shown in **Figure 40**.



*Figure 40. Zirconia TZ-3YSB-E powder used for the sample preparation.*

The crystalline size and particle size of the powder are 36 nm and 600 nm, respectively. The powder granule size is 60  $\mu m$ . The chemical characteristics of Zirconia TZ-3YSB-E powder are presented in **Table 5** [203].

*Table 5. Chemical composition of Zirconia TZ-3YSB-E powder [203].*

Elements	Composition in wt%
$ZrO_2 + HfO_2 + Y_2O_3 + Al_2O_3$	> 99.9
$Y_2O_3$	5.15
$Al_2O_3$	0.25
$SiO_2$	$\leq 0.02$
$Fe_2O_3$	$\leq 0.01$
$Na_2O$	$\leq 0.04$

## Sample preparation

### 4.1.1. Conforming method

The samples used in this Master's thesis were prepared by the conventional Cold Isostatic Pressing (CIP) method. The technique makes use of a high-pressure fluid chamber to compact ceramic powder that is contained inside a flexible mould. CIP technique was chosen because is much more comprehensive in terms of ensuring high and homogeneous density (i.e. less porosity) throughout the zirconia blank [204]. A total of 50 samples were produced to be used in the posterior surface treatment and characterization tests.

The isostatic pressing was performed on the Isostatic Press machine (**Figure 41**). The machine operation principle is based on two steps: *first, making a preform of zirconia by applying pressure into a cylindrical mould; and after, introducing the preform into the cold isostatic press containing the pressurised fluid (such as soluble oil), and applying pressure to the fluid from a pumping system*. As a result, a cylindrical green compact of 15 mm diameter is obtained. Even so, a further step of sintering is required to obtain the final sample.



*Figure 41. Isostatic Press used in the laboratory to make the green compact of zirconia.*

The procedure followed during the isostatic pressing of the zirconia samples is explained with detail below. Also, in **Figure 42** a scheme of the steps followed are shown and briefly mentioned below:

1. Using an electronic balance, 3 gr of zirconia TZ-3YSB-E powder were weight into a watch glass.
2. The powder is placed into the cylindrical mould of the equipment by using a glass funnel. Then a small metallic element is used to close the mould, so the powder can be compacted.
3. The mould is placed in the press and a pressure of 10 bar is applied for 30 seconds to form a compact preform.
4. After the compaction time elapses, the preform is removed from the mould. In this step, it is important to carefully remove the chamber pressure since a sudden removal could result in the expansion of the material and cracking.
5. Introduce the preform inside a neoprene glove. To speed up the process, it is recommendable to introduce 4 preforms into the same glove, each one on one finger.
6. Apply vacuum to the glove and close it using a flange. There must be no air in the glove, so the applied pressure is equal in all directions.
7. Submerge the glove into the pressure vessel that has the pressurised fluid (oil). The glove must be covered-up by oil. The fluid is responsible for the homogeneous compression of the mould and therefore, the zirconia preforms.
8. Apply 30 bar of pressure and then carefully remove the chamber's pressure.
9. Remove the glove from the pressure vessel and take the samples out carefully. They mustn't get dirty with oil, if not, during the posterior sintering clack spots will appear.
10. Green compact samples are obtained after the isostatic pressuring. However, a posterior sintering process is required to have the final samples.

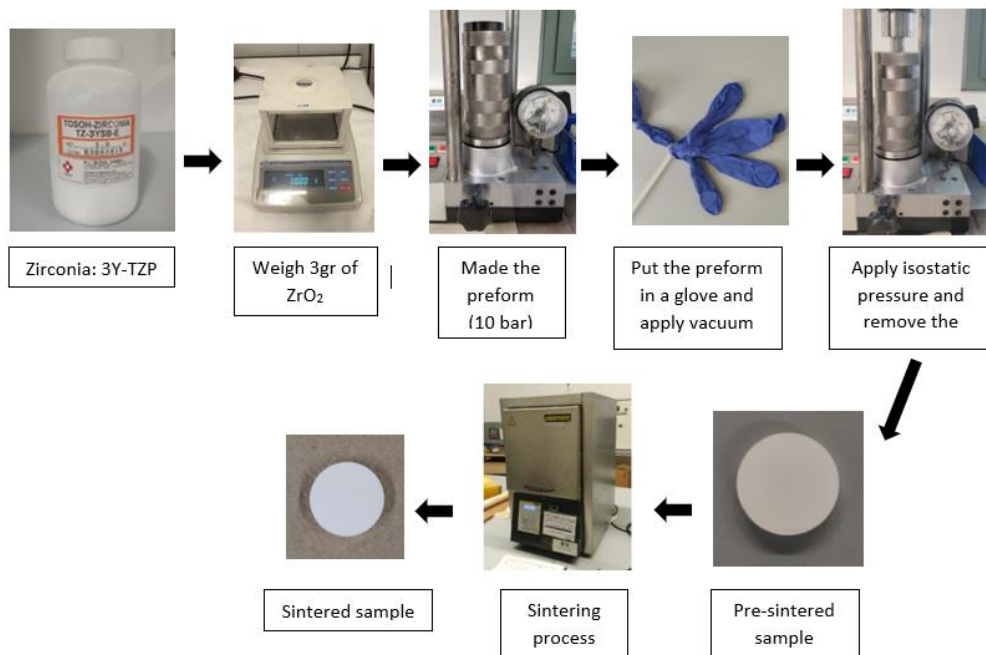


**Figure 42.** Schematic representation of the sample preparation process by Cold Isostatic Pressing (CIP) + sintering process.

#### 4.1.2. Sintering process

After the CIP process, the next step is the sintering of the obtained green bodies. This is a solid-state sintering process, where the particles are bonded and the compact densified by the application of heat below the melting point of a material. As a result, the surface area of the compact is decreased, and this is normally accompanied by an increase in the density. Besides, there will be changes in other properties of the compact, such as increased strength, a drop in electrical resistance, or an increase in thermal conductivity [205].

From the structural point of view of the zirconia, the solid-state sintering process consists of compacting the material without melting it. This involves the diffusion mechanism of the atoms which is enhanced at high temperature [8]. The sintering is generally divided into three stages [205]:

1. **Initial stage (Figure 43a):** There is a rearrangement of the particles and formation of contact points or “necks” between the individual powder particles in the compact. The density is up to 75 % of the theoretical one.
2. **Intermediate stage (Figure 43b):** Necks between particles have grown, resulting in a structure that contains continuous pore channels through the compact. The density is up to 75 – 95 % of the theoretical one.
3. **Final stage (Figure 43c):** The pore channels break up into isolated pores that are generally located on the grain boundaries. The density is higher than 95 % of the theoretical one.

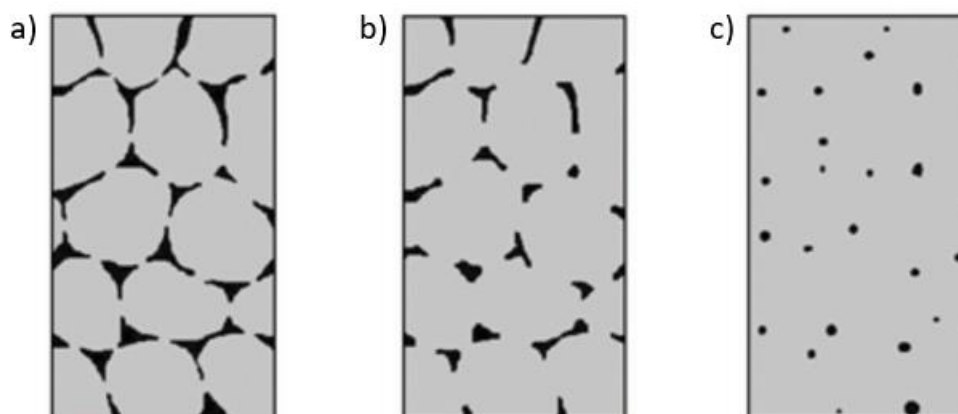


*Figure 43. The three stages of solid-state sintering: a) initial stage, b) intermediate stage, c) final stage [205].*

One important parameter to take into consideration is the treatment temperature. It will influence on the grain size, and thus, on the mechanical properties of the final sample. For example, Stawarczyk *et al.* [206] investigated the effect of sintering temperatures on the grain size and flexural strength of zirconia. The study was made the temperature range of 1300 – 1700 °C where they observed that the grain size increases with the temperature in the whole range, as is shown in **Figure 44**.



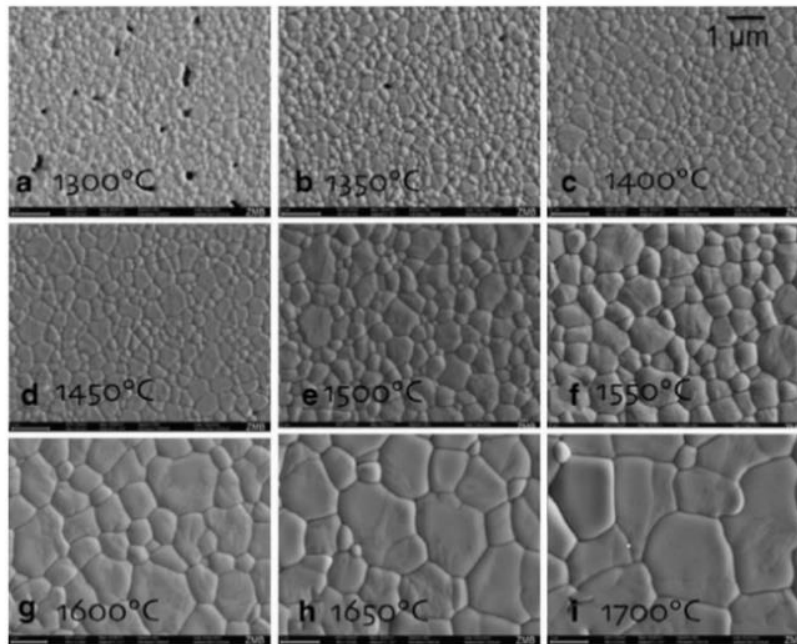


**Figure 44.** Zirconia grain size after different sintering temperatures ( $\times 50,000$ ), a) 1,300°C, b) 1,350°C, c) 1,400°C, d) 1,450°C, e) 1,500°C, f) 1,550°C, g) 1,600°C, h) 1,650°C, i) 1,700°C [206].

However, in the case of the flexural strength, the highest flexural strength was observed in groups sintered between 1400 and 1550°C (see **Figure 45**). This was attributed to the presence of porosity between the grains at low sintering temperatures, because of poor atom diffusion; while at the high sintering temperature, the high size of the grains reduces the mechanical properties. In the study, they concluded that “when a compromise needs to be made for the optical and mechanical properties, the sintering temperature should not exceed 1550 °C”.

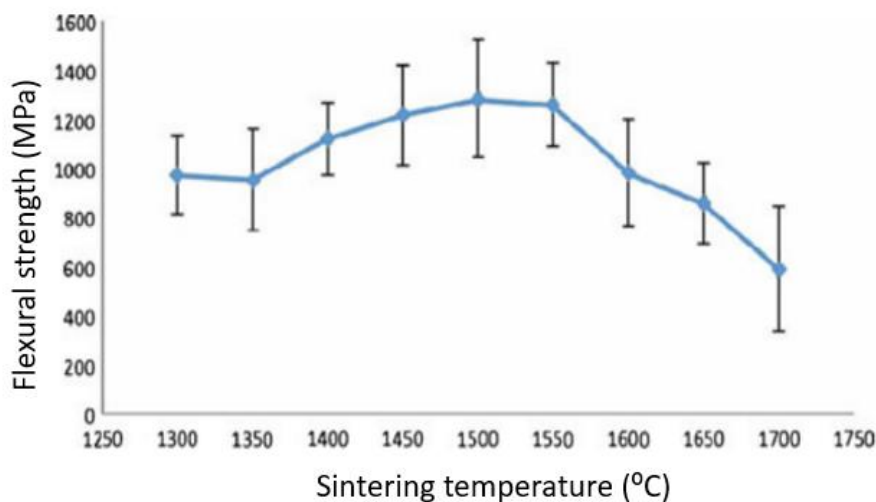


**Figure 45.** Mean flexural strength of zirconia after different sintering temperatures[206].

In this investigation, the solid-stage sintering process was realized in a Nabethern furnace, shown in **Figure 46**. Considering the study explained above, the green bodies were sintered up to 1450 °C, following the thermal treatment presented in **Figure 47**.



**Figure 46.** Photography of the Nabethern furnace.

This thermal treatment consisted of heating up to 700°C at a heating speed of 6 °C·min<sup>-1</sup> and then maintaining at that temperature for 1 hour. After this first step, the temperature was increased with a heating speed of 6 °C·min<sup>-1</sup> up to 1450 °C and maintained constant for 2 hours. Finally, the specimens were cooled with a speed of – 6°C·min<sup>-1</sup> until reaching ambient temperature.

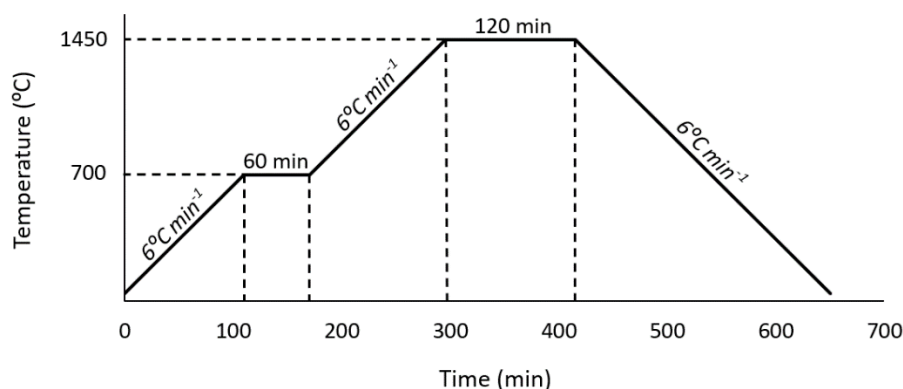


**Figure 47.** Thermal treatment used to sinter the green bodies.

Once carried out, this process of sintering allows to obtain the final geometry, microstructure and mechanical properties. There was a decrease in the dimensions of the final sample compared with the green body, as represented in **Figure 48**. The microstructure and mechanical properties were characterized further on.

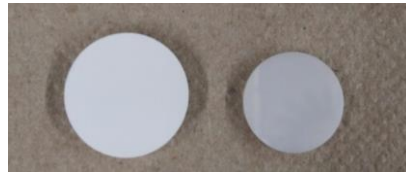


**Figure 48.** Sample before and after the 1450°C sintering process (left and right, respectively)

#### **4.1.3. Polishing of the samples**

Once the samples have been sintered, their surface must be polished to eliminate the roughness and imperfections. The polishing stage is essential within the sample preparation since it will considerably influence on the obtained results. Firstly, A great surface finish is required to successfully analyse the microstructure and mechanical properties of the sample, since a non-flat sample or the presence of scratches on the surface may produce unreliable results. Secondly, the surface finish of the samples after polishing must be good enough to not interfere with the surface modification treatments. Lastly, cell behaviour is greatly affected by roughness; therefore, smooth samples are required to avoid interferences and ensure that the cellular response is only accordingly to our patterns.

A Buehler sander polishing machine was used, specifically, the Alpha model, *2-speed grinder polisher* (**Figure 49**) This machine enables to set the rotating velocity of the disc. Furthermore, it has the option of performing an automatic polishing, by adding a plate that holds the samples. When using it in this mode, it allows selecting the applied load as well as the rotation direction.



**Figure 49.** Automatic polishing machine BUEHLER used for the polishing process.

The polishing of the samples is conducted in two stages, the first one being the grounding stage and the second one being the polishing stage. At the same time, five different discs were used in total, two for the first stage and three for the next one. In **Figure 50** the five discs used are presented. As the discs change, they become less rough.



**Figure 50.** From left to right: MD-Piano 120, MD-Piano 220, MD-Plan, MD-Dac, and MD-Nap [207].

Considering the high amount and the small size of the samples, polishing the samples individually would have been a very complicated and time-consuming process. However, the machine has the option of performing a fully automatic polishing by using an add-in plate, so that eased the work. For the automatic polishing, the samples were first glued equidistantly in the border of the plate, and then, the plate was placed in the machine. Due to the high number of samples, the polishing was done in two rounds, first 25 samples and then the others.

The samples were polished by using the polishing process protocol described in **Table 6**. The important parameters to consider on each step are the disc type and suspension material used, the rotational speed and direction, the rotating time and the applied force. An important point here is that the force is proportional to the number of samples used.

**Table 6.** Polishing process protocol.

Order	Disc	Suspension	Rotation speed	Direction	Time	Force
1	MD-Piano 120	Tap water	300 rpm	Contrary *	15 min	1 LB/sample
2	MD-Piano 220	Tap water	300 rpm	Contrary *	15 min	1 LB/sample
3	MD-Plan	Diamond (30 $\mu\text{m}$ )	150 rpm	Contrary *	15 min	1 LB/sample
4	MD-Dac	Diamond (6 $\mu\text{m}$ )	150 rpm	Contrary *	10 min	1 LB/sample
5	MD-Dac	Diamond (3 $\mu\text{m}$ )	150 rpm	Contrary *	10 min	1 LB/sample
6	MD-Nap	OPA (0,5 $\mu\text{m}$ )	150 rpm	In favour **	5 min	0,2 LB/sample

\*Contrary – The disc and the plate rotate in opposite directions.

\*\*In favour – The disc and the plate rotate in the same direction.

## **Design of Experiments (DoE)**

Before the laser surface modification of the zirconia samples, it was necessary to find out the combination of the laser parameters that would give the desired surface laser pattern. Therefore, it was of great interest to analyse how the variation of different laser parameters impact on the sample surface. For that, a Design of Experiment (DoE) was planned where various combinations of laser parameters were tested. Subsequently, the depth and thickness of the generated laser pathways were measured to identify the most suitable laser parameters combination according to the objective of the project.

### **4.1.4. Concept and definition**

*Design of Experiments* (DoE) is defined as a systematic method to determine the relationship between factors affecting a process and the output of that process. In other words, it is used to find a cause-and-effect relationship [208]. In general, the main purposed of a DoE consists of [209]:

- *Reduce the number of needed experiments.*
- *Verify all factors that affect an experiment (i.e. more than one variable).*
- *Define a strategy to obtain reliable results after a set of experiments.*

The key of a good DoE is to design the most adequate set of experiments to obtain the desired information. Thus, the first thing to do is to determine the research goal. Then, the experimental responses that may be representative to evaluate the defined objective must be identified, as well as the possible variable that can affect the results [209]. A simplified process model applicable to all DoE is shown in **Figure 51**, which is a typical process with several controllable (and uncontrollable) factors that affect one or more measured response [210].

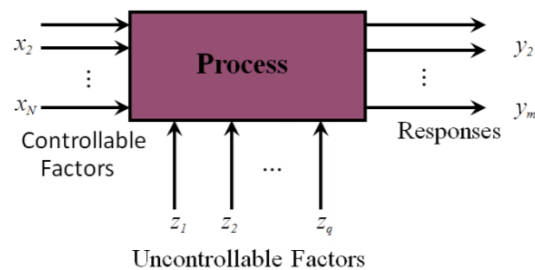


*Figure 51. Schematic representation of a simplified DoE process model [210].*

#### 4.1.5. Methodology

Different approaches and models can be chosen in a DoE. Each model is represented with a different *design space*, which can be interpreted as an n-dimensional geometrical shape defined by the investigating variables [211]. From the experimental results of the running tests, a specific *response function* ( $Y$ ) can be defined. This  $Y$  represents the response trend and can be used for predicting a result of an experiment in untested conditions over the experimental domain, which is called the *response surface*. The area where the *response surface* is constructed is known as *factor space*. For instance, when two variables ( $X_1$  and  $X_2$ ) are explored in an experiment, the resulting factor space is the one represented in **Figure 52** [209].

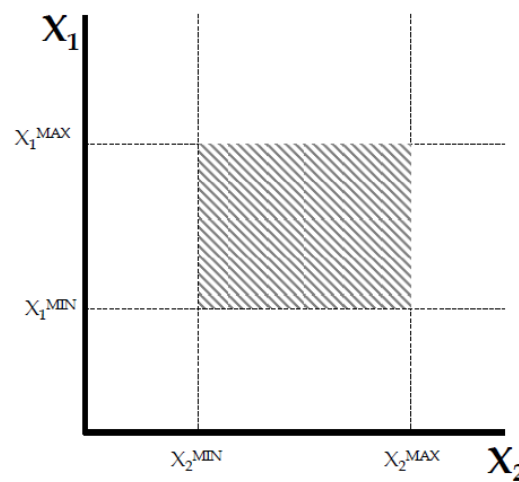


**Figure 52.** Representation of the experimental domain investigation when two variables ( $X_1$  and  $X_2$ ) are considered. The area filled with the diagonal lines represents the factor space [209].

The most suitable models depend on the number of selected variables and the capacity to fabricate samples and to perform experiments. The most common models are full factorial design and partial factorial design, which are described below.

- **Full Factorial Design**

This approach performs the experiments for all the possible combinations of levels of factors. The number of *experiments runs* ( $N$ ) is expressed as  $N = k^m$ , where  $m$  is the number of *factors* or variables and  $k$  is the number of *levels* [210].

The main drawback of this design model is that it implies a large number of experiments because  $N$  grows very quickly as the number of variables or levels increases. Thus, it is appropriate to use it when working with reduced numbers of variables, and a high degree of control in the regression is needed [209].

As stated before, each model can be interpreted as a different geometrical inspection of the experimental domain. In the case of the full factorial design, the geometrical shape is defined by the minimum and maximum values of the variables tested. However, in some cases, it may be useful to perform some additional experiment with intermediate values for a better understanding [210]. In the following figure is possible to see how the maximum and minimum values form a rectangle (Figure 53A) or a cube (Figure 53B), in a 2 or 3 variable design, respectively.

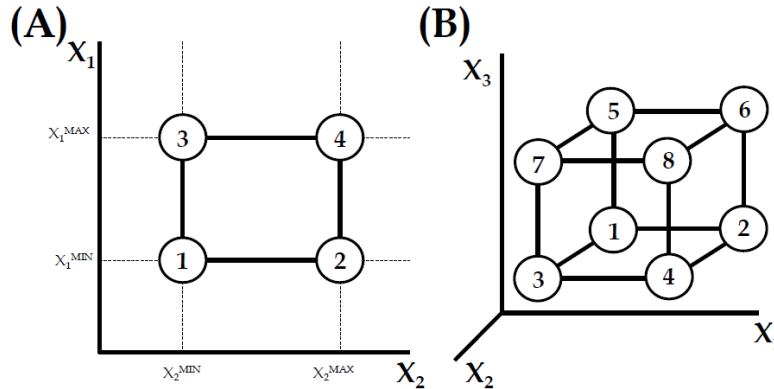


**Figure 53.** Geometrical distribution of the experiments in a 2 (a) and 3 (b) variable design [209].

#### • Partial Factorial Design

The partial factorial design is an alternative approach where the number of experimental runs is reduced. It is the best option when there are limitations performing the experiments, such as technical, economic, or time restrictions. Nevertheless, it is often impossible to predict which variables will significantly affect the response. Therefore, to avoid the risk of excluding important factors, it is recommended to use the maximum possible variables [209].

For example, the design of (Figure 54a) allows to directly investigate system responses to extreme values of the controllable variables. On the other hand, the design of (Figure 54b) yields data that can be more straightforwardly used in fitting the experimental results to a theoretical model.

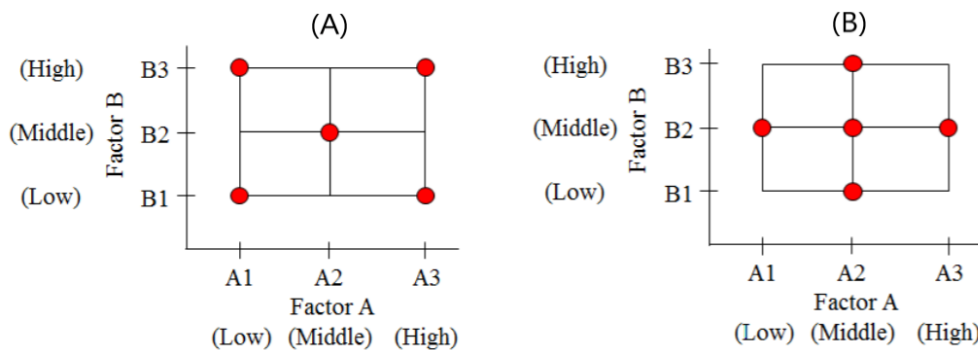


**Figure 54.** Examples of partial factorial designs for an experiment with two controllable factors A and B and three levels for each factor. Each red circle represents an experimental run [210].

#### 4.1.6. Design of the laser experiments

Regarding the experimental design of the laser conditions, the goal of the research is to find the optimum laser parameters that adequate most the surface roughness patterns in order to enhance the cell adhesion. A full factorial approach was followed for the design of the laser experiments. The critical parameters to take into consideration for this analysis are: laser beam intensity, frequency, and mark speed, and the measured responses was depth of the laser pathway, as indicated in **Figure 55**.

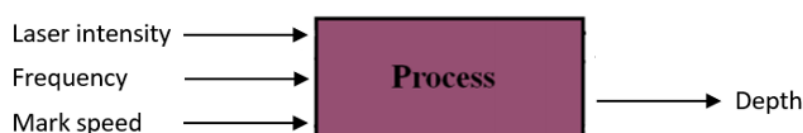


*Figure 55. Schematic representation of design of the laser experiment.*

The minimum and maximum values selected were 2 and 3A for laser intensity, 250 and 1000Hz for frequency, and 1 and 5 bit/mseg for the mark speed. However, in this case, it was considered useful to perform additional experimental runs with intermediate values to better understand the observed change. A summary of the group of tests planned and done along this Master's thesis are presented in **Table 7**.

*Table 7. Conditions for the laser tests.*

Test number	Intensity (A)	Mark speed (bits/mseg)	Frequency (Hz)
<b>Test 1</b>	1.1	2	1
	1.2	2	2
	1.3	2	5
<b>Test 2</b>	2.1	2,5	1
	2.2	2,5	2
	2.3	2,5	5
<b>Test 3</b>	3.1	3	1
	3.2	3	2
	3.3	3	5

*\*250Hz, 500Hz, 750Hz and 1000Hz*

The experimental plan is divided into three main test groups to determine the influence of the laser intensity: test 1, test 2 and test 3 for intensities of 2, 2,5 and 3A, respectively. Also, the impact of the laser mark speed was analysed, meaning that each intensity was tested for speeds of 1, 2 and 5



bit/mseg (test x.1, x.2 and x.3, respectively). Finally, it was of great interest to observe how changes in the frequency influence the obtained surface pathway. Hence, for all combinations of intensity and mark speed, frequencies of 250, 500, 750 and 1000 Hz were tested.

In total, the DoE consists of 36 tests, which were all done in the same sample to facilitate the posterior analysis. As one of the parameters to study is the mark speed of the laser, it was not possible to represent the DoE as a matrix of points. In contrast, a line of 1200  $\mu\text{m}$  in length was drawn for each test. The resulting matrix of the DOE consists of 36 lines organized in 3 columns and 3 rows. Additionally, for ease of identification of each line, the respective laser parameters were represented around the matrix. A scheme is shown in **Figure 56**.

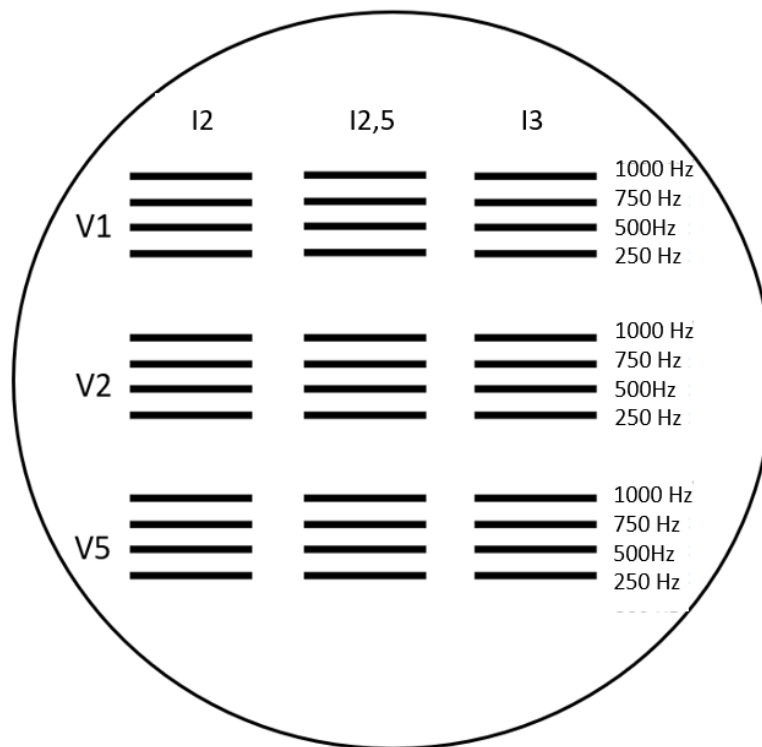


**Figure 56.** Line matrix is drawn on the sample surface together with the laser parameters used.

Once the matrix of 36 lines was made, the sample was cleaned with ethanol and sonicated for 20 minutes. Then, it was cleaned again with ethanol and let it dry. This process facilitates the removal of the particles of dirt.

Finally, the depth of all the 36 laser paths were measured. The depth variation in function of the laser intensity, frequency and scan speed was represented. This facilitate the choice of the best laser parameter combination considering the application of the project. All the process of laser parameter selection is widely explained in **Annex A.1**.

## Surface treatment

As stated in the introduction (see **section 2.3.4**), the modification of the zirconia surface is one feasible approach to enhance its osseointegration behaviour. In this section, the experimental procedure followed for the surface modification of the zirconia samples is explained. The process was conducted by using laser treatments to create defined topographical patterns at the micrometric length scale. Subsequently, some samples were also chemically etched by using HF (40%) to generate a homogeneous roughness gradient along with the specimens (from nano- up to micrometric length scale).

### 4.1.7. Laser treatment

The Spectra-Physics Explorer One 349-120 laser equipment was used for the surface modification of the samples, which generates a beam with a diameter of  $0.16 \pm 0.025$  mm. The output characteristics of the laser are summarized in **Table 8**.

*Table 8. Specification of Spectra-Physics Explorer One 349-120 Laser. [212]*

Output characteristics	
Wavelength (nm)	349
Pulse Energy ( $\mu\text{J}$ @ 1 kHz)	120
Output Power (mW @ 1 kHz)	120
Pulse width (ns)	< 5

In **Figure 57** is shown the experimental set-up, which includes a laser generator equipment, 3 optical devices (two reflective mirrors and a converging lens), and the sample holder. All those elements are placed on a support table that allows setting the optimum configuration for the tests. The operating system of the set-up consists of laser equipment generating a laser beam that strikes the two reflective mirrors (first one mirror and then the other one). These two reflective mirrors are positioned so that they direct the laser beam towards the converging lens. Finally, this lens will adjust the intensity and focus the laser beam on the surface of the sample holder, where the sample is placed. The sample holder has three micrometres that allow changing the x, y and z directions so that the laser beam is applied onto the sample surface.

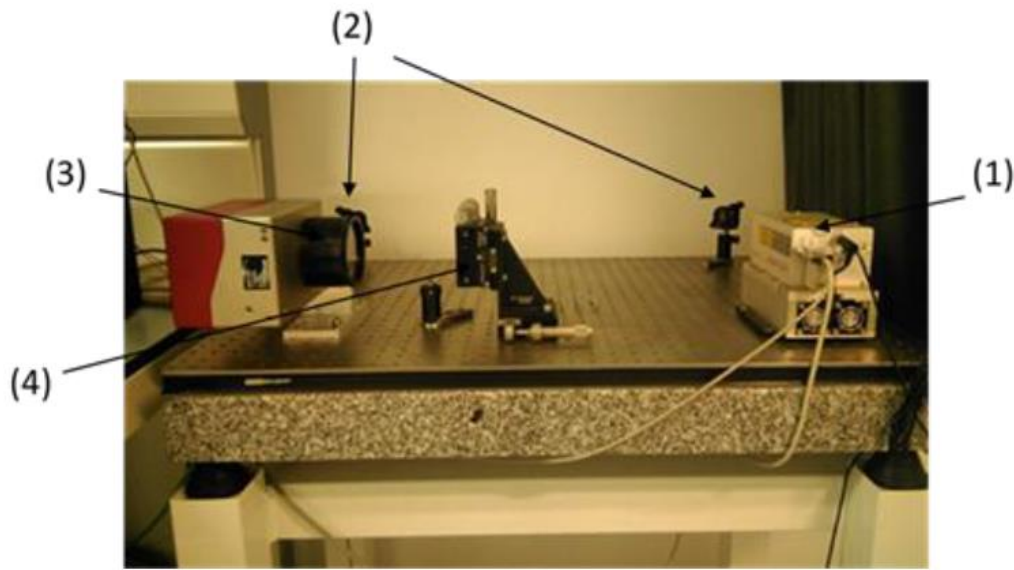


**Figure 57.** Laser equipment and optical devices composing the experimental set-up, where (1) denotes the laser, (2) the reflecting mirrors, (3) the converging lenses and (4) the sample supporting system.

Both the laser and the lens are connected to a computer, so it is possible to modify the laser parameters and draw the shape of the laser pattern. On one side, the L-Win software enables to set the intensity and frequency of the generated laser beam. On the other side, the software WeldMARK is used to draw the shape to be applied to the surface of the sample. Moreover, this second one allows to focus and adjust other parameters of the laser beam, as is the case of the mark speed. The interfaces of L-Win and WeldMARK are added in **annex A.2**.

## ***Hydrothermal degradation***

Accelerated degradation tests in water steam were performed at 134 °C and 2 bars of pressure (Micro8, Selecta). The samples were degraded for 10h. Then the  $V_m$  (%) was quantified by X-ray Diffraction (XRD) and Raman spectroscopy. Furthermore, the  $V_m$  (%) distribution along the samples surface was analysed by Raman spectroscopy mapping. Finally, the hardness of the samples was measured by Vickers indentation.

## Characterization techniques

### 4.1.8. Microstructural characterization

#### 4.1.8.1. Density

The Archimedes method was used to measure the bulk density of the samples and to calculate the amount of open porosity. The measurement of those parameters allows to get a first estimation about mechanical properties of the material, as the porosity directly affects the mechanical strength, fatigue strength and the elongation to rupture [213].

Archimedes method was chosen because it is non-destructive, simple and the most economic one; however, it must be taken into account that the measured density is an estimation since the method does not contemplate the closed porosity (because the fluid cannot penetrate inside). It relies on the Archimedes principle [214], who stated that: “any body completely or partially submerged in a fluid (gas or liquid) at rest is acted upon by an upward or buoyant force, the magnitude of which is equal to the weight of the fluid displaced by the body.” Deriving from this physical law, it is possible to calculate the density of an object from its mass difference in normal air and the fluid (**Figure 58**).

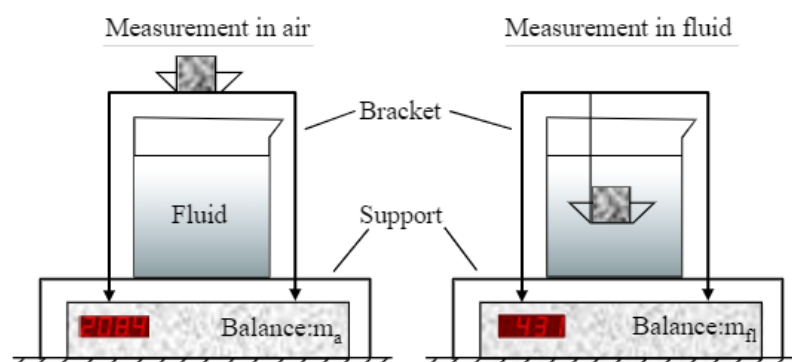


**Figure 58.** Archimedes method, showing the measurement of the mass in air and the fluid [213].

The calculation of the density ( $\rho$ ) follows the **Equation 1**, where  $m_a$  and  $m_f$  represent the weight of the object in air and in the fluid, and  $\rho_a$  and  $\rho_f$  are the densities of the air and the fluid, respectively. The mass is expressed in g and the densities in  $g \cdot cm^{-3}$  [213].

$$\rho = (\rho_{fl} - \rho_{air}) \times \frac{m_a}{m_a - m_{fl}} + \rho_{air} \quad \text{Equation 1}$$

The measurements were performed with an Archimedes machine Mettler Toledo XS-204, shown in **Figure 59**. This device allows the direct calculation of the material density with a 5 digits accuracy. For that, first, it is necessary to install the accessories into the device: *a beaker filled with water, the basket and the balance*. The next step is to weight the object, first in the air and then in a liquid of known density (water was selected  $\rho_{water} = 1 \text{ g}\cdot\text{cm}^{-3}$ ). From here, all calculations, including temperature adjustment of the fluid, are performed automatically by the device, and it is also possible to evaluate multiple samples at the same time [215]. A major problem is that accuracy of the measured density is affected by the open-porosity of the sample since it will absorb water. Thus, the first value observed after submerging the sample in the water is taken as the right measure.

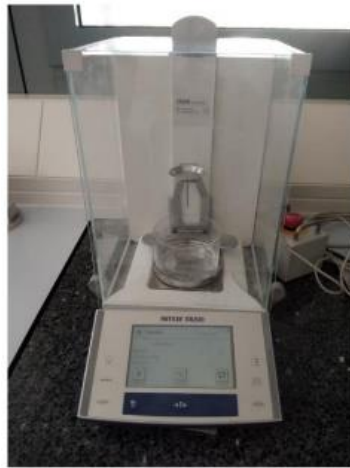


*Figure 59. Analytical balance Mettler Toledo XS-204 employed to determine the density of the samples by using the Archimedes method.*

#### 4.1.8.2. Optical microscope

Various optical microscopes (OM) have been used to evaluate the surface condition of the samples during the polishing process and obtain general images of the sample surfaces. This way it was possible to control the surface roughness and evaluate the presence of scratches on the samples before moving forward to the next polishing step.

The functioning of an OM is based on the use of visible light and a system of lenses to magnify images of small objects. One of the microscopes used during the master thesis for the surface evaluation of the sample during the polishing is an Olympus BX53M microscope presented in **Figure 60**, which relies on LED illumination and allowed magnifications of 5X, 10X, 20X, 50X and 100X [216].



Figure 60. OM Olympus BX53M [216].

#### 4.1.8.3. Laser Scanning Confocal Microscope

The Laser Scanning Confocal Microscope (LSCM) has been used to visualize the surface of the samples and extract results after the surface treatments and the mechanical and tribological tests were performed.

Confocal microscopy is an optical methodology used for recording 3D images with resolution equal or superior to that of the conventional light microscope. It consists of two diaphragms: a lighting diaphragm that emit the laser beam, and a detection diaphragm to detect the light reflected by the sample, as shown in **Figure 61**. The detection diaphragm plays a significant role since it eliminates the out-of-focus light, so the brightness and resolution of the image are augmented. Base on this, it is possible to obtain optical sections of the sample, and then, by the superposition of those sections, a focus 3D image can be reconstructed [13].

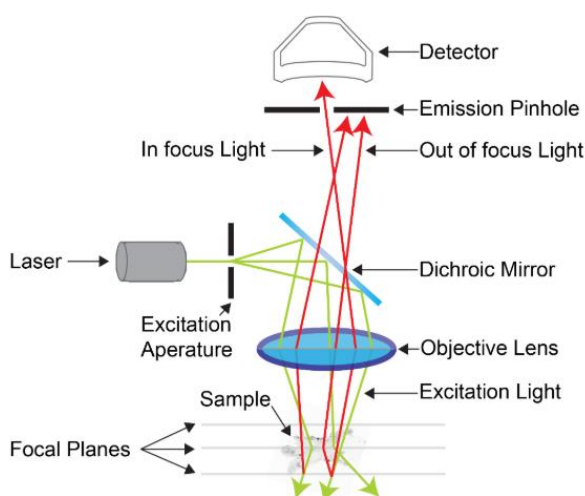
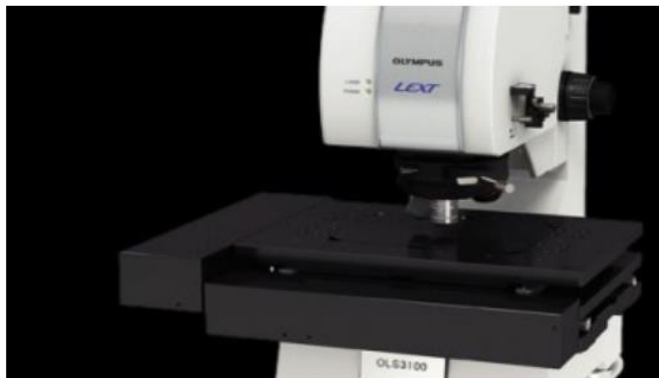


Figure 61. Schematic of the laser scanning confocal microscope [217].

Laser confocal microscope Olympus LEXT OLS 3100 was used for obtaining surface topographic images of the samples after the laser and chemical etching surface treatments, as well as for characterizing the residual imprints of the Vickers indentations performed to the samples. This device, which is shown in **Figure 62**, allows images up to 5000 magnifications and it can be used in both optical and confocal mode. Besides, it is equipped with an image analysis software that can be used for: (i) *facilitating the image visualization by applying filters to the acquired images (contrast change, smoothing, etc.); and (ii) image analysis such as point to point measurement, roughness profile, depth measurement, etc.*



**Figure 62.** Laser scanning confocal microscope Olympus LEXT OLS 3100 [218].

The image analysis feature was used several times to analyze the surface of the sample. Initially, the LSCM was the first choice to characterize the laser tests performed to the sample during the DoE. However, the DoE consists of 45 experiments that combine various laser parameters, so it was very time-consuming to measure one by one the roughness profile and thickness of all those lines. Thus, later on, once the optimal laser parameters were decided, this method was used to measure the distances between the parallel lines of the laser pattern.

#### **4.1.8.4. X-Ray diffraction**

The functioning of the X-Ray diffraction (XRD) technique is based on constructive interference of monochromatic X-rays and a crystalline sample. These X-rays are generated by a cathode ray tube, filtered to produce monochromatic radiation, collimated to concentrate, and directed toward the sample. Then, when the ray strikes the surface of a crystal at any angle, a part is scattered by the layer of atoms on the surface. The undispersed portion penetrates the second layer of atoms where again a fraction is dispersed and so on. The cumulative effect of this scattering from the centre of the crystals is the diffraction of the beam [219].

The measurement of the elastic scattering is based on Bragg's law, see **Equation 2** [219]:

$$2 \times d \times \sin(\theta) = n \times \lambda$$

Equation 2

where  $d$  is the space between two successive planes,  $\vartheta$  the incident angle of the X-ray beam,  $\lambda$  the wavelength of the beam, as it is shown in **Figure 63**.

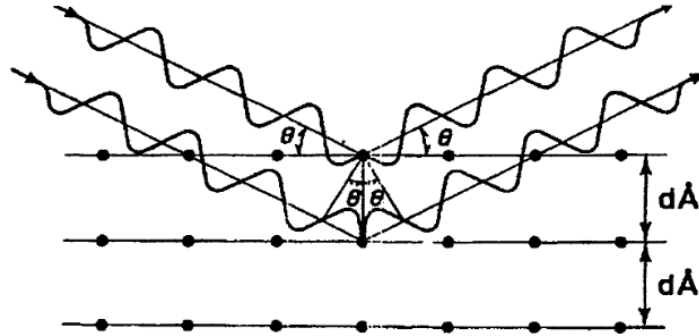


Figure 63. Schematic representation of Bragg's Law [219].

The XRD in a polycrystalline sample makes it possible to identify the different crystalline phases since each crystalline structure have a characteristic XRD spectrum. Thus, the phase structure of the sample can be determined from the peaks detected in the XRD analysis and by knowing the characteristic peaks of each phase. In this Master's project, monoclinic phase ( $m$ -phase) was quantified by XRD in Bragg-Brentano symmetric geometry using Cu  $K_\alpha$  radiation (40 kV and 40 mA) with  $0.02^\circ$  step size, 1s/step and a  $2\theta$  range of  $26^\circ \leq 2\theta \leq 37^\circ$ . A PIXcel3D detector was used for the investigation, see **Figure 64**. Moreover, the volume fraction of the monoclinic phase ( $V_m$ ) was calculated with the **Equation 3** proposed by Toraya *et al.* [220], as follows:

$$Vm (\%) = \frac{1.311 [Im(\bar{1}11)+Im(111)]}{1.311 [Im(\bar{1}11)+Im(111)]+It(101)}$$

Equation 3

where  $I_m$  and  $I_t$  correspond to the intensities of the monoclinic and tetragonal peaks, respectively. These peaks of the zirconia phases are identified according to the literature [221], [222].



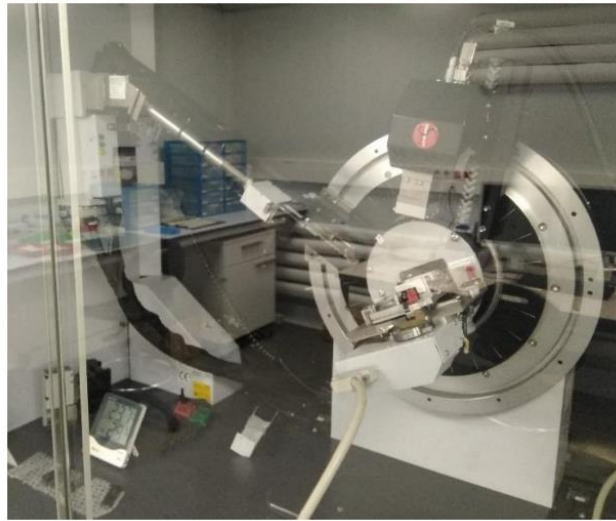


Figure 64. XRD equipment employed in this Master's thesis.

#### 4.1.8.5. Raman spectroscopy

Raman spectroscopy is a molecular spectroscopic technique. It is based on the Raman Effect that utilizes the interaction of light. The Raman principle is based on the inelastic scattering of the light due to the interaction with vibrating matter. When the sample is illuminated with a monochromatic laser light, it is possible to collect the backscattered light through a microscope objective and analyze it with a monochromator getting a spectrum [223].

In the present project, Raman spectroscopy was used to characterize the *m*-phase content of the samples before and after the hydrothermal degradation. Phase maps under the surface were obtained with confocal micro-Raman spectroscopy (inVia Qontor, Renishaw) with a Nd:YAG laser (wavelength 532 nm, integration time 0.1 s) (see **Figure 65**). After, the volume fraction of *m*-phase ( $V_m$ ) was quantified by using the **Equation 4** proposed by Katagiri *et al.* [224] as follows:

$$Vm(\%) = \frac{I_m^{181} + I_m^{190}}{2.2(I_t^{247} + I_m^{181} + I_m^{190})} \quad \text{Equation 4 [225]}$$

where  $I_m$  and  $I_t$  correspond to the integrated intensities of the monoclinic and tetragonal bands, respectively.



*Figure 65. micro-Raman spectroscopy (inVia Qontor, Renishaw)*

#### 4.1.8.6. Scanning Electron Microscope

Scanning Electron Microscopy (SEM) is one of the most advanced techniques when it comes to the nanometric scale topographic analysis of the materials. It enables high-resolution images (20 nm or more) compared to optical microscopes that have a resolution of about 200-250 nm [226]. This is because it uses a focused beam of high-energy electrons source, which generates a variety of signals from the electron-sample interaction. These signals reveal information about the sample: external morphology (texture), chemical compositions (using EDS), crystal structure and crystal orientations (using EBSD) [227].

The working principle of SEM consists of generating high-energy electrons and directing them into the sample so they interact with the atoms of the surface. A schematic of the major components in a SEM is shown in **Figure 66**. On top of the column, there is the electron gun that produces and accelerates the electrons to an energy level of 0.1–30 keV. However, the diameter of the electron beam produced by the gun is too large to generate a high-resolution image, so electromagnetic lenses and apertures are used to form a small focused electron spot on the specimen. This process demagnifies the size of the electron source ( $\sim 50\ \mu\text{m}$  for a tungsten filament) down to the final required spot size (1–100 nm). Furthermore, a high-vacuum environment is needed, which allows electron travel without scattering by the air. Finally, one important characteristic is that the samples must be conductive, and if they are not, they must first be coated with a layer of a conductive material as carbon, gold, or platinum [228].

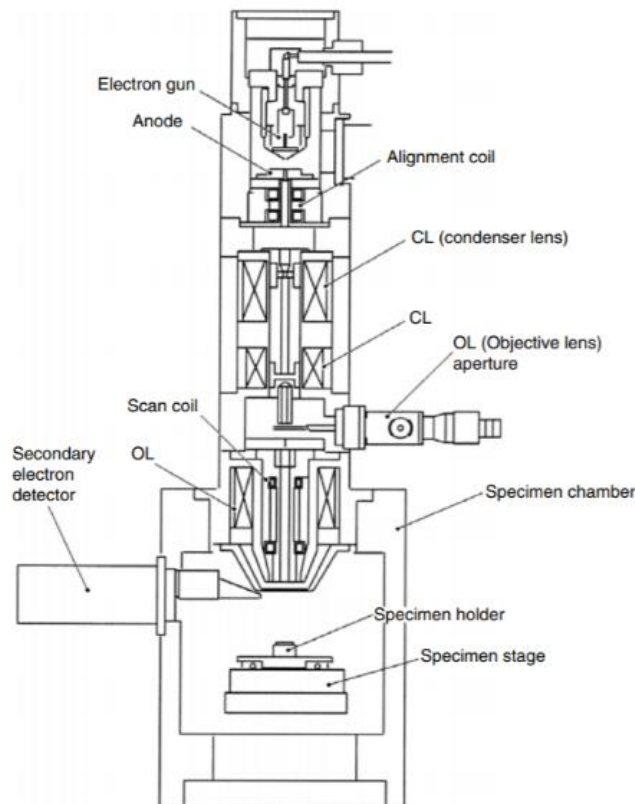


Figure 66. Schematic diagram of a scanning electron microscope [228].

Image formation in the SEM is dependent on the acquisition of signals produced from the electron beam and specimen interactions. These signals include detection of secondary electrons (for topography images), detection of backscattered electrons (to determine the crystallographic structure), and X-ray microanalysis (for chemical composition analysis of the specimen), among others [8].

In this research project, SEM Phenom XL (resolution  $\leq 20$  nm) was used for the characterization of the surface topography of the zirconia samples after laser treatment (see **Figure 67**). Furthermore, the microstructure of the samples after Vickers indentation was also evaluated by this technique in order to clearly see the damage induced under different stresses. Finally, it was also used to acquire images after the cell adhesion study. In all cases, sample surfaces were prepared with a thin layer of carbon coating before introducing them in the SEM chamber to improve the electron conductivity for better imaging.



*Figure 67. SEM Phenom XL [229].*

#### 4.1.8.7. Atomic Force Microscope

Atomic Force Microscopy (AFM) is a powerful imaging technique that, by scanning a sharp tip (typically end diameter 5-10nm) over small areas on the surface, can produce topographical images that quantify the surface morphology. Depending on the interaction between the tip and the sample surface, it reveals information about the topography, magnetic structure, electric charge distribution, material contrast, etc. with a resolution below the nanometre.

A schematic of the main component of the AFM includes a cantilever with a sharp tip, a laser beam, and a photodetector, as represented in **Figure 68**. An AFM operates by measuring the force between the tip of the cantilever and the sample. When the tip is approached or touches the surface, the forces produced in the interaction lead to the deflection of the cantilever. This involves mechanical contact forces, van der Waals forces, capillary forces, chemical bonding, electrostatic forces, magnetic forces etc. Furthermore, the deflection can be measured by reflecting a laser beam off the flat top of the cantilever into a split photodiode detector. Thus, it is possible to generate an accurate topographic map of the surface features [230], [231].

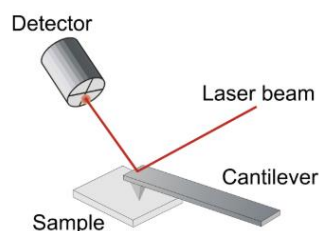


*Figure 68. Schematic drawing of an AFM apparatus [232].*

In **Figure 69** is shown the AFM Veeco Dimension D3100 used in this research for the topographical observation of the zirconia sample surfaces after the laser treatment and chemical etching. This technique has been used in order to measure the depth and width of the laser pattern (with and without chemical etching) for each specimen and to choose the right laser conditions in order to create a micro- and nanometric roughness to enhance the cell adhesion.



*Figure 69. General view of the AFM used in this research (Dimension D3100, Veeco).*

#### **4.1.8.8. Contact profilometer**

The contact profilometer is a common tool used to measure the surface texture. The working principle of this technique consists on tracing the surface with a sharp tip (“stylus”) and recording the tip position using optical or electromechanical methods. A stylus instrument contains a stylus that contacts the surface and an electromechanical transducer that converts its Z coordinate into voltage, followed by an amplifier that makes that voltage easier to digitize, followed by an analogue-to-digital converter that is connected to a computer.

Contact profilometer was used for the topography characterization of the samples during the DoE, which as a tip diamond tip of 2.5  $\mu\text{m}$  radius and a constant applied load of around 3 mg.

#### **4.1.9. Mechanical characterization**

##### **4.1.9.1. Vickers hardness test**

This test is the most conventional methodology used to measure the hardness of the material. It is one of the easier hardness tests since the formula that is used for the hardness calculation is independent of the geometrical properties of the indenter. Furthermore, this method also allows the calculation of the indentation fracture toughness ( $K_{IC}$ ) from the obtained hardness value.

The test method consists of penetrating a square shape pyramid diamond indenter with an angle of  $36^\circ$  between faces, as shown in **Figure 70**. This method is applicable to almost any type of material (both soft and hard), but the samples must be highly polished to enable measuring the size of the impressions. Furthermore, due to its shallow penetration depth, it is a useful and reliable test [233].

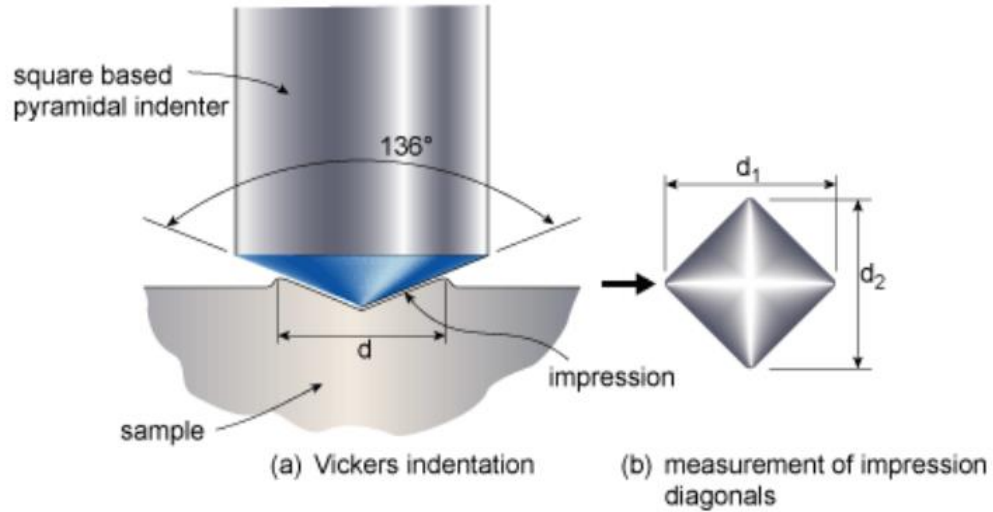


**Figure 70.** Schematic of the Vickers indentation process (left) and the residual imprint (right) [13].

In the present work, the durometer Akashi MVK-H0 with a Vickers tip installed was used to determine the Vickers hardness (HV) and indentation fracture toughness ( $K_{IC}$ ) of the sintered zirconia samples. A load of 10kgf was applied for Vickers hardness calculations. Five indentations were done for each condition and sample type in order to get statistical signification. Furthermore, the indents must be positioned such that there is sufficient clearance from the specimen edge and between the individual indents. Finally, once the indentation was done, the confocal microscope was used to measure the corresponding parameters of the imprints (indentation size and crack length).

Vickers Hardness (HV) of the material is given by **Equation 3**, where  $P$  is the applied load (in kgf) and  $d$  is the mean of the diagonal size (in mm) (see **Figure 71** in blue). Therefore, HV is directly expressed in MPa.

$$H_V = 1.8544 \times \frac{P}{d^2} \quad \text{Equation 5}$$

Finally, the HV is obtained from the average of various measurements and is expressed as **380 HV 10/20**. In that expression, 380 is the hardness number, HV gives the hardness scale (Vickers), 10 indicates the load used in kgf, and 20 is the loading time (used only if it differs from 10 to 15s).

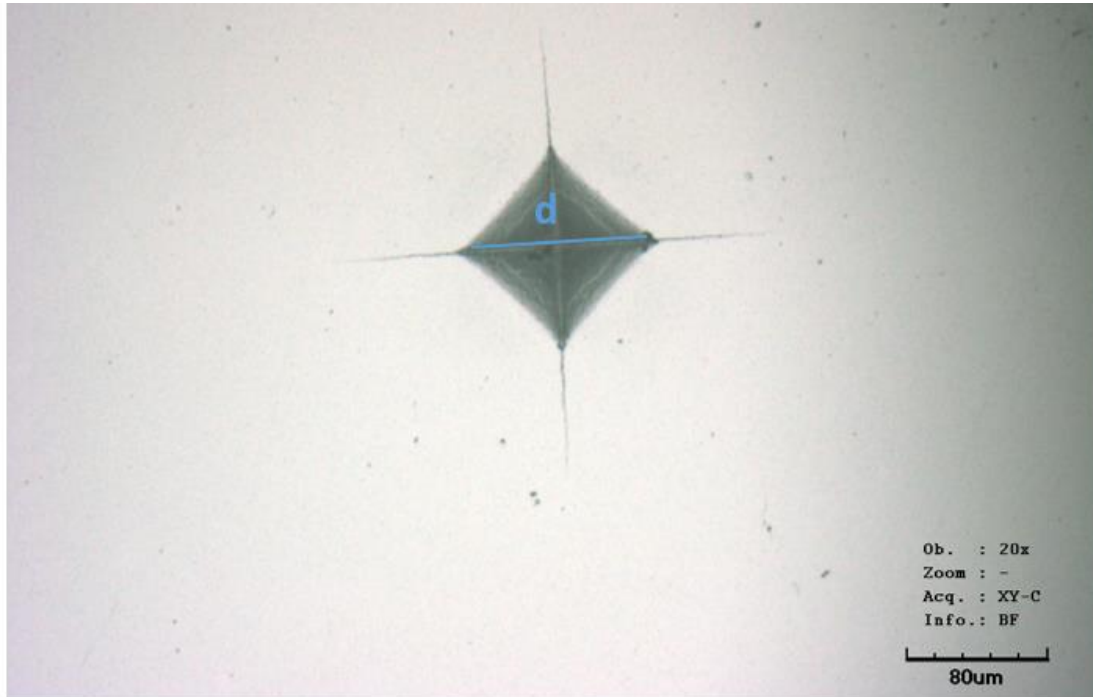


**Figure 71.** LSCM micrograph of a Vicker's hardness imprint conducted at 10 Kgf of maximum applied load. In the figure the diagonal (d) is marked in blue.

## Cellular study

A cellular study was performed to compare the cellular adhesion to non-treated, and laser-treated samples. Human mesenchymal stem cells (hMSCs) were used for the study and immunohistochemistry technique was used to characterize the cell adhesion to the different surfaces. Three samples of each type were used for the study, and the experiment was repeated twice in order to confirm the reproducibility of the results.

### 4.1.10. Cell culture

hMSCs were purchased from ATCC and cultured in Advanced Dulbecco's Modified Eagle's Medium (DMEM) supplemented with 10% (v/v) fetal bovine serum (FBS), 50 U/mL penicillin, 50 U/mL streptomycin and 1% (w/v) L-glutamine. Cells were maintained at 37 °C, in a humidified atmosphere containing 5% (v/v) CO<sub>2</sub>, changing culture medium three times per week. Cells were detached with trypsin-EDTA and replated on a new flask after reaching 80 % confluence. All reagents were purchased from Sigma–Aldrich unless otherwise specified. Before all cellular experiments, samples were sterilized for 15 minutes in 70 % ethanol (v/v) and subsequently washed thrice with phosphate-buffered saline (PBS).

#### 4.1.11. Cell adhesion

hMSCs at passage 4 were seeded at a concentration of 5000 cells/well in serum-free medium and incubated at 37 °C and 5% (v/v) CO<sub>2</sub> containing atmosphere. After 6 hours, the medium was aspirated and non-adherent cells removed by carefully washing with PBS. Cells were fixed with paraformaldehyde (PFA, 4 % w/v in PBS) for 30 min, permeabilized with 0.05% (w/v) Triton X-100 in PBS for 20 min and blocked with bovine serum albumin (BSA, 1 % (w/v) in PBS) for 30 min. Next, actin fibres were stained by incubating with TRITC-conjugated phalloidin (1:300, in permeabilizing buffer) for 1 h, focal adhesions by the subsequent incubation with mouse anti-vinculin (1:100, in BSA 1 %, 1h) and anti-mouse Alexa 488 (1:2000, in triton 0.05 %, 1 h), and nuclei were stained using 4',6-diamidino-2- phenylindole (DAPI) (1:1000, in PBS-glycine 20 mM) for 2 min. All incubations with fluorophores were done in the dark. Between all steps, samples were rinsed three times with PBS-glycine for 5 min. Specimens were mounted in Mowiol 4-88 and examined under a fluorescence confocal laser scanning microscope (CLSM, LSM 800, Carl Zeiss), see **Figure 72**. Finally, the images were processed using Fiji/Image-J package [234] to calculate cell area, circularity and aspect ratio. Typically, 5 pictures per samples were taken, and a number of 15-20 cells per condition analyzed. However, due to the limited amount of time only duplicates were analyzed. In further studies, triplicates and a higher amount of cells e.g. >50 cells/condition should be studied.



*Figure 72. fluorescence confocal laser scanning microscope (CLSM, LSM 800, Carl Zeiss)*



## Results and discussion

### *Selection of the laser parameters*

For the selection of the adequate laser parameters, the **depth** of the laser pathways was considered to be the most significant characteristic to take into consideration. This choice was made based on the fact that the cellular response is strongly influenced by the surface roughness of the sample, as explained in the **section 2.2.4**.

Since several studies agreed that the optimum roughness to promote cellular response is ranged between 1-2  $\mu\text{m}$ , the laser parameters were chosen accordingly to that. Below are summarized the steps followed during the laser parameters selection process, which are explained in detail in **.1**.

1. Initially, the 36 lines of the DoE were characterized by CLSM to measure the depth of each pattern. This allows to obtain the relationship between the laser penetration depth and the main parameters to take into account in this Master's thesis to create a well defined patterns (i.e. frequency, intensity and scan speed of the laser).
2. From all those 36 measures of the DoE, 8 had a penetration depth between 1-2  $\mu\text{m}$ .
3. Those 8 laser paths were then characterized in more detail by mean of AFM, contact profilometry and LCSM. Patterns with parallel lines of 30  $\mu\text{m}$  and 50  $\mu\text{m}$  inter-space were produced for each of the 8 laser combinations. The generated pile-up and repeatability of those patterns was analyzed in order to make the final choice.
4. Finally, the final laser parameters were selected considering 1-2  $\mu\text{m}$  penetration depth, low pile-up induced at the edges of the laser patterns, and high repeatability in all lines. The selected parameters are:
  - *Intensity*: 2.5A
  - *Scan speed*: 2 bit/ms
  - *Frequency*: 500Hz

Once the laser parameters were selected, the next step was to perform the surface modification of the samples. The designed pattern consisted on parallel lines. Three different line spacing were selected: 30, 50 and 100  $\mu\text{m}$ . Also, non-laser treated samples (with flat surface) were used as reference. In **Table 9** is indicated how the samples have been referenced in the tables and graphs presented in the present section.

Table 9. Legend of the samples used.

Space between parallel lines	Legend
Flat surface	Reference
30 $\mu\text{m}$	30um
50 $\mu\text{m}$	50um
100 $\mu\text{m}$	100um

## Microstructurally characterization

### 5.2.1. Density

The bulk density of the sintered samples was measured by the Archimedes method. It is worth to mention the importance of this parameter since it is an indicative of the porosity of the samples, which will directly affect the mechanical response of the specimen.

In this Master's project, 5 different samples were used for the density calculation (see **Table 10**). The average density measured is  $6.08\text{g/cm}^3$ . Furthermore, the comparison of the measured density with the theoretical density of the material enables to calculate the relative density and the porosity rate. Considering that the theoretical density of 3Y-TZP is  $6.10\text{ g/cm}^3$ , the relative density of the samples is 99.70% and the porosity rate is practically negligible, around 0,30%. Finally, since a low porosity rate is attributed to the samples, the mechanical properties may not be decreased because of it.

Table 10. Density of the sintered samples measured by Archimedes method. The relative density and closed porosity of the samples are also calculated.

Sample number	Density [ $\text{g/cm}^3$ ]	Relative density [%]	Porosity rate[%]
1	6.07	99.56	0.44
2	6.09	99.77	0.23
3	6.09	99.77	0.23
4	6.08	99.62	0.38
5	6.08	99.75	0.25
<b>Average</b>	<b><math>6.08 \pm 0.01</math></b>	<b><math>99.70 \pm 0.10</math></b>	<b><math>0.30 \pm 0.10</math></b>

Comparing to other density calculation obtained from the CIP sample preparation technique, the reported values are similar. For example, Camposilvan *et al.* [235] reported relative densities in the range of 97-99%. However, the density of the sample varies depending on the fabrication technique used. If compared to other fabrication techniques, the density of the samples fabricated by CIP is higher, what result in improved mechanical properties [12] [13].

### 5.2.2. Topographical characterization

The laser topography generated along the sample surface was characterized by means of CLSM. A schematic of the parameters measured are represented in **Figure 73** and listed below.

- Valley Height ( $H_v$ ): vertical distance between the flat part and the valley
- Pileup Height ( $H_p$ ): vertical distance between the flat part and the peak.
- Total Height ( $H_t$ ): vertical distance between the valley and the peak.
- Laser width ( $W_v$ ): horizontal distance of the laser pathway, without considering the pile-up.
- Pileup width ( $W_p$ ): horizontal distance of the pile-up.
- Total width: total horizontal distance of the laser pathway, considering both parts the valley and the pile-up.

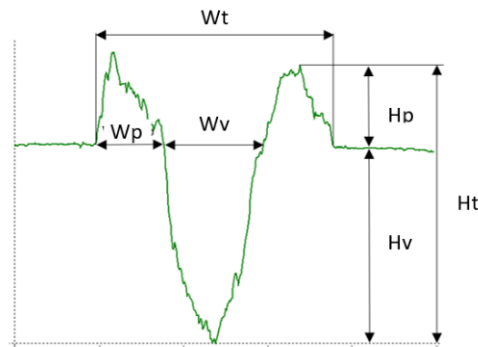


Figure 73. Schematic of the measures performed by LCSM.

Since the laser patterns consist on parallel lines separated by 30, 50 and 100 $\mu\text{m}$  (designated as 30 $\mu\text{m}$ , 50 $\mu\text{m}$  and 100 $\mu\text{m}$ , respectively), the roughness analysis was performed for the 3 different specimens. The results are presented in the **Table 11**.

Table 11. Topography analysis performed by the LCSM. Measurements were done by using x50 objective.

	$H_v$ ( $\mu\text{m}$ )	$H_p$ ( $\mu\text{m}$ )	$H_t$ ( $\mu\text{m}$ )	$W_v$ ( $\mu\text{m}$ )	$W_p$ ( $\mu\text{m}$ )	$W_t$ ( $\mu\text{m}$ )
<b>30<math>\mu\text{m}</math></b>	$1.19 \pm 0.12$	$0.64 \pm 0.10$	$1.75 \pm 0.15$	$14.66 \pm 1.12$	$6.42 \pm 0.78$	$26.20 \pm 0.99$
<b>50<math>\mu\text{m}</math></b>	$1.08 \pm 0.18$	$0.60 \pm 0.15$	$1.64 \pm 0.21$	$15.00 \pm 1.98$	$7.51 \pm 1.34$	$30.60 \pm 2.47$
<b>100<math>\mu\text{m}</math></b>	$1.23 \pm 0.14$	$0.64 \pm 0.13$	$1.81 \pm 0.16$	$13.38 \pm 0.74$	$7.33 \pm 0.95$	$29.44 \pm 1.64$

The total height ( $H_t$ ) measured in the three samples is in the desired range for cellular study (between 1-2 $\mu\text{m}$ ). However, almost 1/3 of the total height is due to the pile-up generated with the laser (about 0.6  $\mu\text{m}$ ) as side effect. Similarly, the pile-up width measured is half of the total width of the laser path:  $\sim 14\mu\text{m}$  of pileup ( $\sim 7\mu\text{m}$  on each side) compared with  $\sim 30\mu\text{m}$  of total width. Ideally, it was intended for the pile-up to be the minimum as possible since it may decrease the mechanical properties of the

material and promote the  $t \rightarrow m$  phase transformation. Compared with other studies where laser surface modification of zirconia has been performed [162, 236], the side effect produced in the work is much higher. This is attributed to the accuracy of the type of laser used: in the present work a nanosecond laser was used while in almost all the published works a pico- or femto-second laser was selected (which is more accurate).

In the following figure are presented CLSM images of 30 $\mu\text{m}$  (**Figure .a**), 50 $\mu\text{m}$  (**Figure .b**) and 100 $\mu\text{m}$  (**Figure .c**) surface patterns. Two parts can be differentiated: the laser path (dark gray) and the non-treated flat surface (light gray). As explained in the paragraph above, the low accuracy of the laser used implies a wider laser path. Therefore, even if the desired interlineated for the cellular study are 30 $\mu\text{m}$ , 50 $\mu\text{m}$  and 100 $\mu\text{m}$ , in real, the non-treated space between to subsequent lines is about 5 $\mu\text{m}$ , 25 $\mu\text{m}$  and 75 $\mu\text{m}$  (deducted from the images by using the scale bar). Furthermore, from the observation of the images it can be said that the laser beam does not only produce micrometer roughness (the valley and pile-up), but also nanoscale roughness along the valley. This may be interesting for the cell adhesion study.

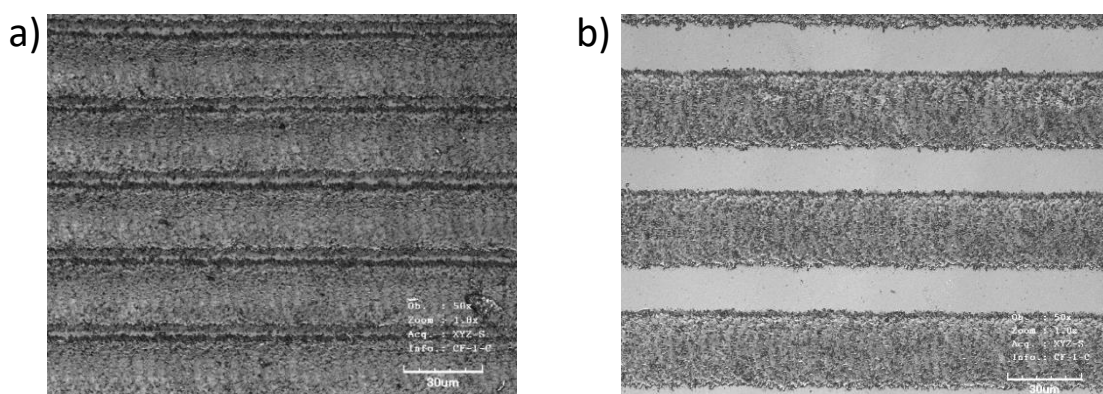
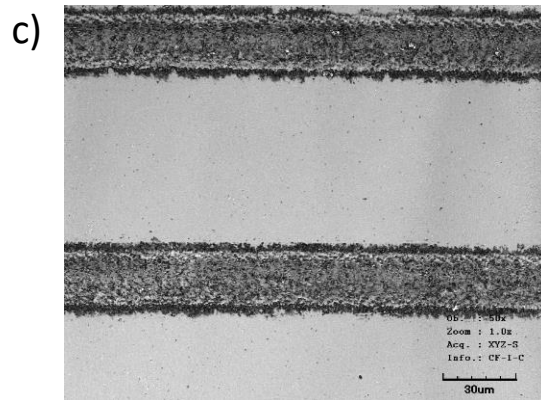


Figure 74. Images of the topography of the 3 samples a) 30 $\mu\text{m}$ , b) 50 $\mu\text{m}$  and c) 100 $\mu\text{m}$ . The images were captured with the x50 objective and using the microscope mode.



**Figure 74.** Images of the topography of the 3 samples a) 30µm, b) 50µm and c) 100µm. The images were captured with the x50 objective and using the microscope mode (continuation).

## Hydrothermal degradation

### 5.3.1. Raman Spectroscopy

The presence of *m*- and *t*-phase contents was evaluated by Raman spectroscopy. **Figure 75** shows a *m*-phase mapping of the samples surface before and after 10 hours degradation in steam. It can be seen that the flat sample (reference) and the laser modified samples (30, 50 and 100µm) do not have any *m*-phase content before the degradation process (left images). By contrast, after 10 hours in steam water, all the samples present *t* → *m*-phase transformation on the surface, where accordingly to the Raman calculation,  $V_m$  (%) varies from 15 - 90% depending of the sample type and surface spot. Herein, the 30µm degraded sample (30µm HD-10h) presented the maximum *m*-phase transformation volume that ranges from 50-90%. However, previous studies have revealed that a penetration of the laser beam can be up to 40µm, leading to Raman signals collected from well below the surface layer, and altering peak intensities [237]. Thus, it must be noted that the monoclinic  $V_m$  (%) calculated may not be accurate, although it can be used for a qualitative analysis of the surface degradation.

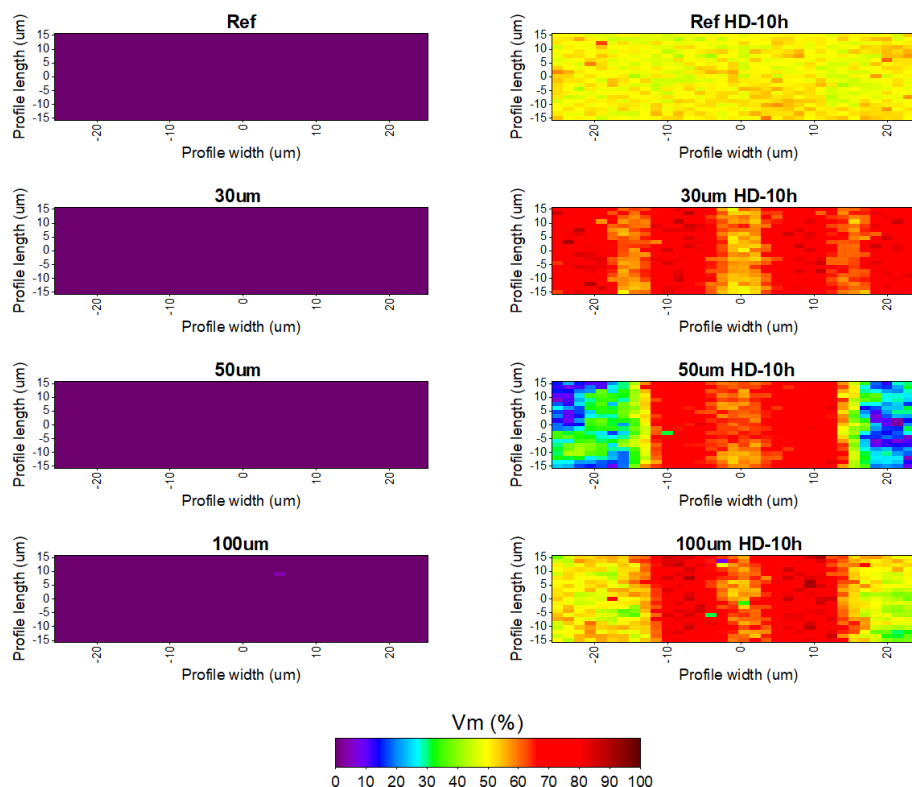


Figure 75. Raman spectroscopy of the samples before (left) and after 10 hours in water steam (right).

Furthermore, in **Figure 75** it is shown that the *m*-phase volume content is not homogeneous among all the surface of the degraded samples (30 $\mu$ m-HD10h, 50 $\mu$ m-HD10h and 100 $\mu$ m-HD10h). In the Raman map of the degraded samples three spots are differentiated: the flat part (non-modified), the laser valley, and the pileup (see **Figure 76**). Regarding  $V_m(\%)$  of each spot, the pileup is the most transformed one while the flat part presents the less *m*-phase content in all the three specimens.

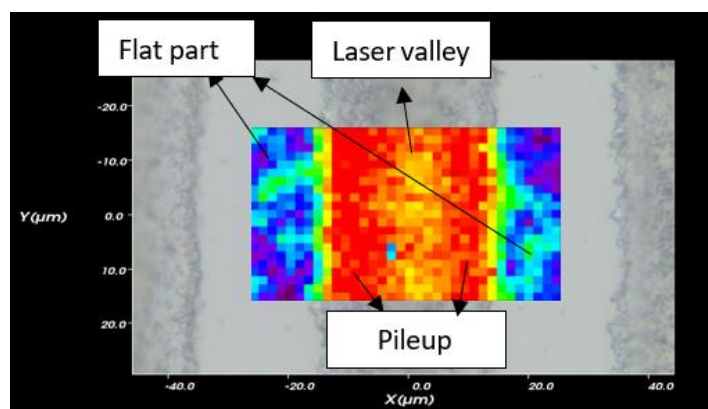
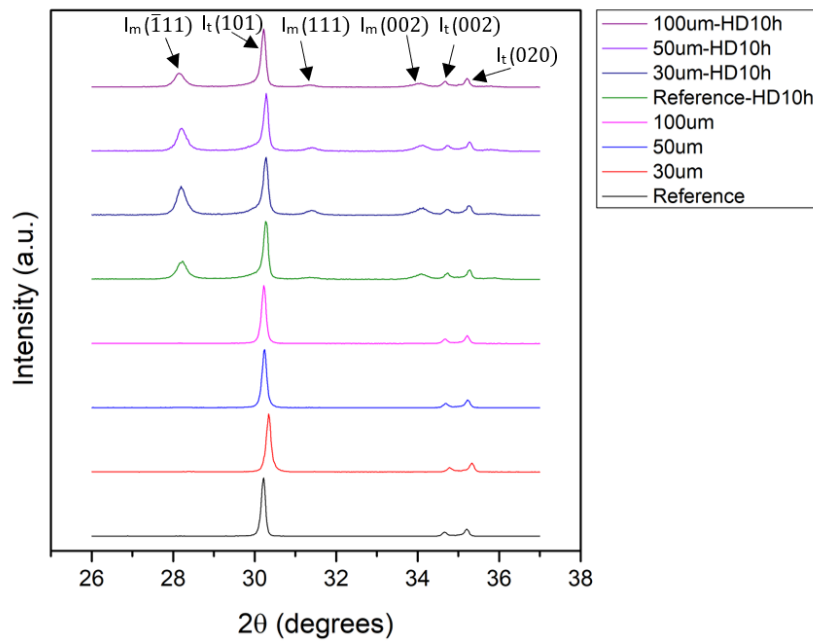


Figure 76. Image with the three spots on the laser modified sample: flat part, laser valley, and pileup.

### 5.3.2. XRD

The normalized XRD spectra of the non-degraded and hydrothermally degraded samples is shown in **Figure 77**. When comparing all the spectra it can be seen that the peaks corresponding to the  $(-111)$ ,  $(111)$  and  $(002)$  planes of the  $m$ -phase are present in all the degraded samples, but absent in the non-degraded ones. Thus, this is an indicative of the  $m$ -phase content created after the degradation process. Moreover, the intensity of those monoclinic peaks varies between the degraded samples, meaning that different  $V_m$  (%) are created on each one.



**Figure 77.** XRD spectra of the samples before and after 10h degradation in steam water.

The  $V_m$  (%) content was calculated according to Toraya *et al.* [220]. In figure **Figure 78a** it is presented a superposition of the 8 normalized XRD spectra for the range of  $2\theta$  between  $27^\circ$  and  $32^\circ$  where the 3 relevant peaks for the calculation appeared. In **Figure 78b** it is shown the  $V_m$  (%) calculated from the equation proposed by Toraya *et al.* [220]. The  $m$ -phase content is negligible in the non-degraded samples (black line) since it is lower than 2 in all cases. However, after 10 hours of degradation in steam water, the  $m$ -phase is present in the four samples (in blue). The  $V_m$  (%) of the degraded samples ranges from 25% (100um-HD10h) to 45% (30um HD10h).

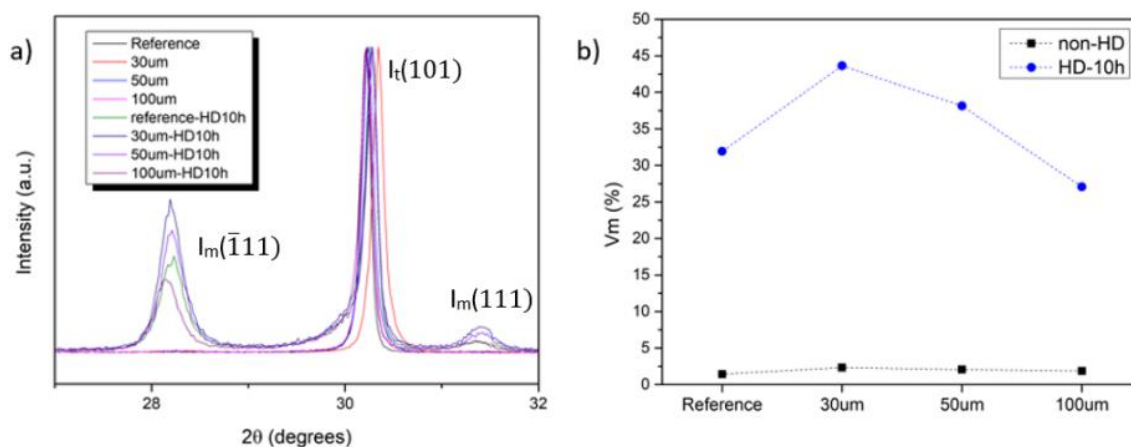


Figure 78. a) Magnification of the  $(\bar{1}11)$ ,  $(111)$  monoclinic and  $(101)$  tetragonal peaks. b)  $m$ -phase volume fraction.

If compared with the Raman data, the  $V_m$  (%) values obtained by XRD are significantly lower. This is because, as mentioned in the previous section, the penetration depth of the Raman laser is up to 40 $\mu$ m, while in the XRD analysis the 63% of the attenuated signal comes from depths less than 2 $\mu$ m and the 95% from depths up to 5  $\mu$ m [238]. Therefore, the  $V_m$  (%) obtained with XRD are more representative for a quantitative analysis of the  $m$ -content on the sample surfaces.

### 5.3.3. Vickers Hardness

Vickers Hardness (HV) was measured in the non-degraded and degraded samples as an indicative of how the degradation affects the mechanical properties of the zirconia. In **Figure 79** are represented the HV values obtained for all the samples before and after 10h degradation. The HV of the non-degraded samples (in black) is similar in the four specimens. The value ranges from 13.8 to 14.1 GPa, which is slightly higher than the reported in the bibliography (~13 GPa) [137]. This may be attributed to the low porosity rate obtained in the density calculation. Furthermore, between the non-degraded samples, 30 $\mu$ m has the higher value, that may indicate that laser pileup agglomeration created in the samples induce a hardening mechanism.



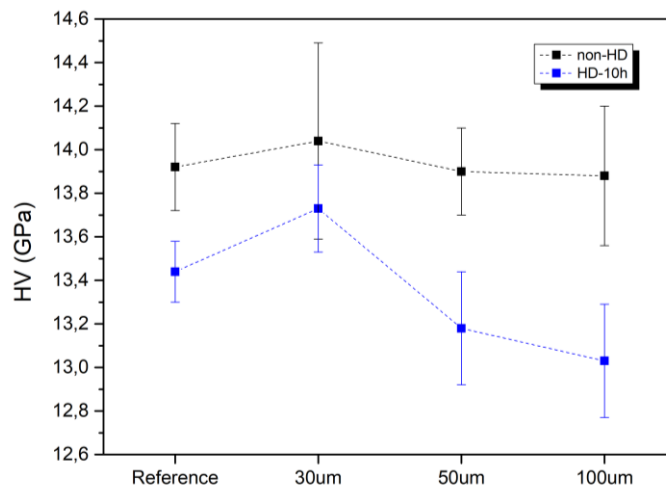


**Figure 79.** Vickers hardness of the specimens before and after 10h of degradation in steam water.

Moreover, the graph clearly shows that the hardness value dropped in all specimens after the hydrothermal degradation (line in blue). This is related with the increase in the  $V_m$  (%) content calculated with Raman and XRD: The volume expansion of the  $t \rightarrow m$ -phase transformation induces compressive stress on the surface that may affect the mechanical properties of the sample [136]. Also, the HV range among the degraded samples is wider compared to the non-degraded ones: 100um-HD has the lower hardness value (13.0 GPa), while 30um-HD has the higher one (13.8 GPa). Even so, the hardness of the degraded samples is still comparable of even higher of the theoretical one.

## Cellular study

### 5.4.1. Qualitative analysis

Herein below are presented the images obtained by the fluorescence LCSM of hMSCs adhered to the samples. The results are divided on 4 sections, each one corresponding to one sample type: reference, 30 $\mu$ m, 50 $\mu$ m and 100 $\mu$ m. In all images actin filaments are stained with phalloidin-rodamine (red), cell nuclei with DAPI (blue), and vinculin (focal adhesions) with anti-vinculin and anti-mouse-Alexa 488 primary and secondary antibodies, respectively.

#### Reference: Flat sample

Two fluorescence LCSM images of the reference sample are presented in **Figure 80**. In both images there is a low number of adherent hMSCs, indicating a low cellular adhesion flat surface. Furthermore, the cells have a circular shape and have not spread along the surface. This characteristic is an indication

of poor attachment to the flat surface, owing to the fact that the surface lacks biochemical or topographical signals [3]. Finally, cells fail to align on the flat surface.

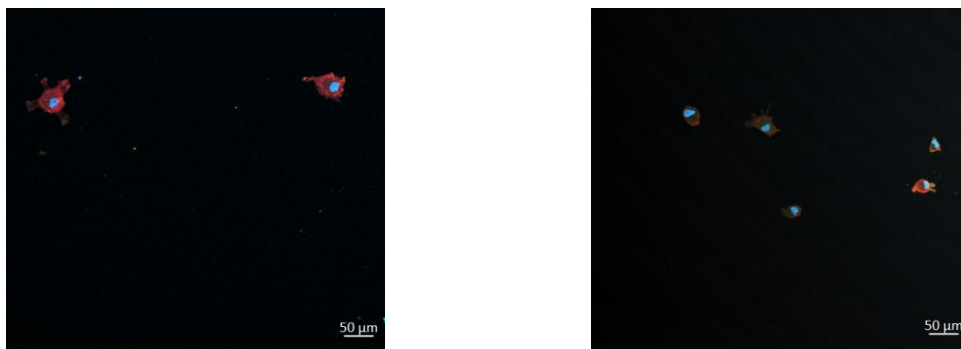


**Figure 80.** Fluorescence LSCM images of the cells cultured on reference (flat) sample. Actin filaments are stained with phalloidin (red), cell nuclei with DAPI (blue), and vinculin (focal adhesion) with anti-vinculin and anti-mouse antibodies.

#### 30μm line spacing sample

Two fluorescence LSCM images of the 30μm inter-spacing sample are presented in **Figure 82**. Compared to the reference, there is a similar number of adhered hMSCs. Regarding the cell morphology, they also presented a rather circular shape. However, there is an increase on the cell area in contrast to reference sample since the cells have spread along the surface, showing clear cytoskeletal elongations. Of note, such extensions seem to interact and attach to the topographies induced by the laser. Finally, a slight cell alignment in the direction of the pattern can be observed.

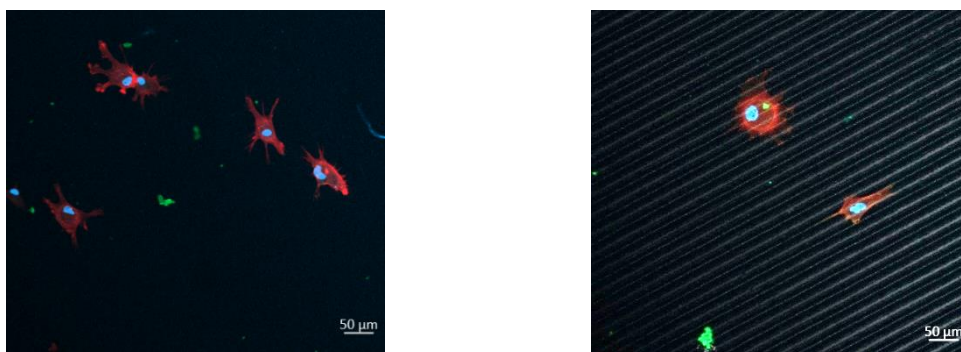


**Figure 81.** Fluorescence LSCM images of the cells cultured on 30μm line spacing sample. Actin filaments are stained with phalloidin (red), cell nuclei with DAPI (blue), and vinculin (focal adhesion) with anti-vinculin and anti-mouse antibodies.

#### 50μm line spacing sample

Two fluorescence LSCM images of the 50μm inter-spacing sample are presented in **Figure 82**. Compared to the reference and 30μm specimens, more hMSCs have adhered to the 50-inter-spacing pattern. Furthermore, like in the 30μm specimens, cell area has notably increased: the cytoskeleton of the cells has spread along various laser pattern to find anchoring points in the induced topography. In

this specimen, the attached cells presented a more elongated shape as compared to the other two cases. Finally, cellular alignment in the direction of the pattern is clearly observed.

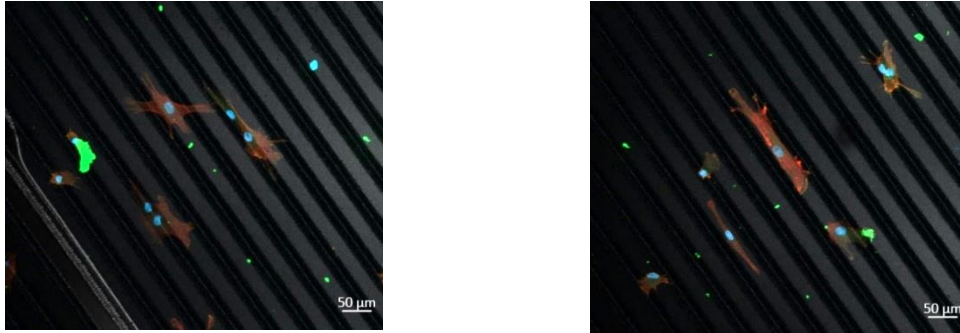


**Figure 82.** Fluorescence LSCM images of the cells cultured on 50µm line spacing sample. Actin filaments are stained with phalloidin (red), cell nuclei with DAPI (blue), and vinculin (focal adhesion) with anti-vinculin and anti-mouse antibodies.

#### 100µm line spacing sample

Two fluorescence LSCM images of the 100µm inter-spacing sample are presented in **Figure 83**. Like in the previous case, the number of cells attached to the 100µm specimen is increased. Furthermore, the 10µm sample presented the cells with higher area. Regarding the morphology, the cells attached presented a rather elongated shape, but not as pronounced as observed in the 50µm samples. Finally, there is a moderate cell alignment along the pattern: the cells are preferentially located in the non modified part of the surface (light gray), spread along various pattern lines, and attached to the laser modified part of the sample surface (black).

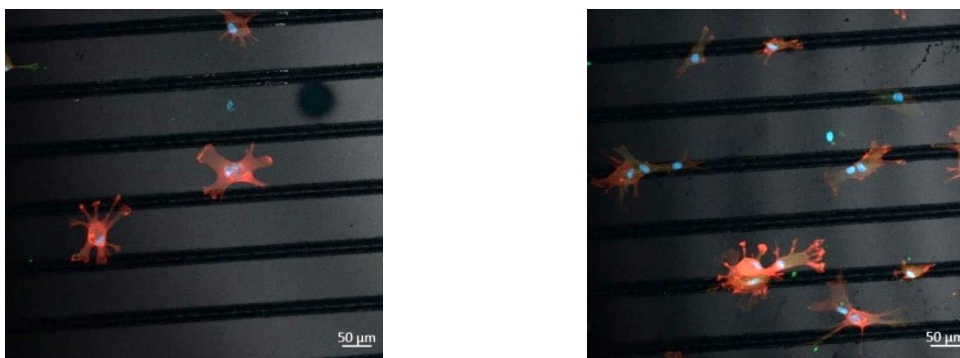


**Figure 83.** Fluorescence LSCM images of the cells cultured on 100µm line spacing sample. Actin filaments are stained with phalloidin (red), cell nuclei with DAPI (blue), and vinculin (focal adhesion) with anti-vinculin and anti-mouse antibodies.

### 5.4.2. Quantitative analysis

The fluorescence LCSM images were analyzed with ImageJ (see Methods section) in order to obtain quantitative data of the cellular study. The cells attached to the four specimens were analyzed in terms of cell area (**Figure 84a**) circularity (**Figure 84b**) and aspect ratio (**Figure 84c**).

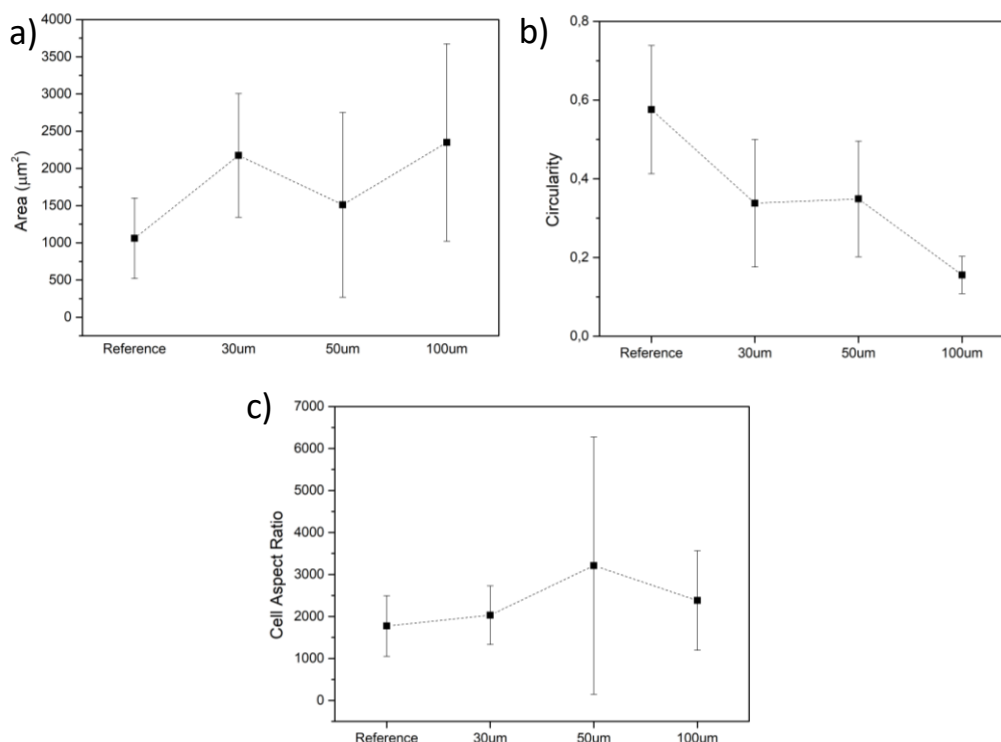


**Figure 84.** hMSCs adhesion result after 6h of incubation in medium without FBS. a) cell area ( $\mu\text{m}^2$ ), b) cell circularity, c) cell aspect ratio.

In the first place, it can be confirmed that the laser patterns increase the cell area as compared to the flat sample (reference). The average cell area is doubled in the 30μm and 100μm samples, and increased by a factor of 1,5 in the case of the 50μm specimen. Furthermore, cell morphology is characterized by the circularity (from 0-1, being 1 the maximum circularity) and aspect ratio (level of cell elongation). Regarding the circularity property of the measured cells, this value is decreased in all laser modified samples in contrast with the reference specimens. More specifically, the cells adhered to the 100μm specimens displayed the lowest circularity, i.e. less rounded cells. Moreover, the aspect ratio graph indicates that the cell elongation is increased on all the laser-patterned samples. Herein, the cells attached to the 50μm inter-spacing pattern appear to have the most pronounced elongation, being this value double as compared to the reference. However, it should be noted that high standard deviation values were obtained in the three graphs and thus the results should be analyzed with caution. This is because, due to the lack of time, only 15-20 cells per condition were considered for the

quantitative analysis. Therefore, in order to reduce the error, a higher number of cells should be taken into consideration.

In general, from both the qualitative and quantitative analysis it can be summarized that the adhesion of the hMSCs is increased on the laser-modified specimens. This finding is in concordance with other studies performed in the field [3], [161]-[163]. Regarding the cell morphology, the patterned surfaces induce more elongated cells with bigger area (spreading). Cell alignment along the direction of the patterns have been also observed. These effects are expected to positively influence cell behavior in terms of proliferation, migration and differentiation [3], and thus improve the biological performance of zirconia-based materials. However, a deeper characterization of the cellular study is required to choose the laser pattern that promotes the best cellular response.

## Environmental impact analysis

During this Master's thesis, the environmental impact caused is related to the use of material for sample preparation (zirconia powder, distilled water, acetone, ethanol, diamond and alumina colloidal suspension, cleaning paper) and cellular study (hMSCs, PBS, FBS, medium, triton, primary and secondary antibodies, DAPI, BSA, triton, glycine, ethanol, trypsin, etc.) the water consumption during the polishing process, and the energy consumed during the diverse processes such as thermal treatment, surface modification or sample characterization.

Regarding the materials used, it can be said that chemicals used during the polishing and cellular assay processes do not have an elevated impact on the environment because they are not acid, bases or aggressive substances. To minimize the environmental impact, the materials were used reasonably and measurably to avoid waste or leftover products. For example, during the sample preparation, a glass tunnel was used to prevent the loose of zirconia powder; also, a wasteful feed of substances as distilled water, acetone, ethanol and diamond and alumina colloidal suspension was tried to avoid; and the cleaning paper was reused as much as possible. Finally, the residues generated were recycled in the corresponding bin provided by the CIEFMA and BBT laboratories to reduce the final environmental impact.

The water consumption during the polishing process has a great environmental impact since it required the use of a continuous flow of water for some steps of the process. More specifically, 30 minutes of continuous water flow is needed for the polishing process, which must be repeated for 50 samples. However, in order to minimize the consumed water, many samples were polished simultaneously by gluing them into a flat and metallic add-in plate of the polishing machine.

Finally, the environmental impact caused by energy consumption is mostly due to the oven used for the thermal treatment and the laser equipment used for the surface patterning. The oven required the largest amount of energy because the thermal treatment lasts a total of 11 hours and 1450 °C are reached for 2 hours. However, to reduce the energy used by the oven, as many possible samples were introduced simultaneously in the oven, so the thermal treatment process was repeated as few times as possible. Regarding the laser machine, it also requires much energy because a high energy pulse is applied to the sample. However, it is an extremely fast process (30s/sample), which reduced the amount of energy consumed. Lastly, the impact caused by the electricity consumed for the characterization tests such as the use of the diverse microscopes and the Vickers indentations as well as the computer was much lower in term of energy consumption compared to the oven and the laser machine.

## Conclusions

In this Master's project, the effect of laser-surface modification on 3Y-TZP has been investigated. The defined topographical pattern consists on parallel lines with interspaces of 30, 50 and 100  $\mu\text{m}$ . In this sense, the density, surface topography and cellular response to those patterns was analyzed. Furthermore, the hydrothermal degradation of the samples after 10 hours in steam water was evaluated: the microstructure of the degraded samples was characterized by XRD and Raman Spectroscopy, and the hardness was measured by Vickers method.

The conclusions drawn from the results presented are listed below.

- **Laser surface modification technique**
  - The depth of the laser tracks can be adjusted by the laser intensity, frequency and scan speed.
  - The laser parameters that adjust better to the project purpose are: 2,5A of laser intensity, 500Hz frequency and 2bit/ms scan speed.
- **Density measurement**
  - The average density measured is 6.08g/cm<sup>3</sup>.
  - The samples presented high relative density (99.70%) and low porosity rate (0.30%).
  - The CIP technique allows to obtain samples with reduced porosity, and there, better mechanical properties.
- **Topographical characterization**
  - The total height measures obtained by LSCM are 1.75 $\mu\text{m}$ , 1.64 $\mu\text{m}$  1.81 $\mu\text{m}$  for 30 $\mu\text{m}$ , 50  $\mu\text{m}$  and 100 $\mu\text{m}$  specimens, respectively. All cases are inside the desired range for the cellular study (1-2  $\mu\text{m}$ ).
  - The pile-up obtained is considerable ( $\sim 0.6\mu\text{m}$  height and  $\sim 7\mu\text{m}$  width).
  - The laser beam generated produce micrometer scale roughness (the valley and pileup) and also nanoscale roughness (along the valley).
- **Hydrothermal degradation**
  - From the Raman spectroscopy maps can be deduced that the  $V_m$  (%) is negligible in all the non-degraded samples, while in the degraded samples ranges from 25-90%.
  - The Raman mapping indicated that the  $V_m$  (%) is not homogeneous along the laser patterned surfaced (after degradation). Herein, the pileup zone is the most affected one.
  - The XRD spectra indicated that there is  $m \rightarrow t$  phase transformation after the HD process. The  $V_m$  (%) is negligible in all the non-degraded samples, while in the degraded ranges from 25% (100 $\mu\text{m}$ -HD10h) to 45% (30 $\mu\text{m}$  HD10h).
  - Vickers Hardness is reduced after the HD process.

- **Cellular study**

- The adhesion of the hMSCs is increased on the laser-modified specimens.
- The patterned surfaces promoted cell spreading (bigger areas) and more elongated cells
- Cell alignment is observed, specially in 50µm and 100µm samples.
- The obtained results are not enough to choose the pattern that promotes the best cellular response

On a personal note, this work has given me invaluable insights into the operation and constraints of numerous different characterization techniques. I have worked with the laser equipment, where I learned how to modify the parameters in order to get the desired surface topography. I have become familiar with numerous microstructural characterization techniques (CLSM, OM, Contact and Optical Profilometer, AFM, SEM and Raman), and mechanical characterization techniques (Vickers). Finally, I have learned how to perform a cell adhesion study, which implies cell culture and posterior immunohistochemistry procedure.



## Future work

During this project an extensive study has been carried out on the topography, microstructure and cellular response to laser patterned samples. Although many properties have been studied, there are still other areas to which future work can be directed. Furthermore, the project was intended to submit in November, so more experiments were intended to be performed, which can be now considered as future work.

- It would be interesting to perform a more extensive characterization of the topography of the patterned surface by FIB cross section, SEM observation as well as evaluating the residual stresses induced during the laser patterning.
- It was intended to characterize the mechanical properties of the patterned sample by nanoscratch and nanoindentation techniques.
- Regarding the qualitative and quantitative analysis of the cellular study, it would be more appropriate to consider more images. Thus, the obtained result would be more accurate. Also, it would be of great interest to observe the cell by SEM technique.
- Finally, one of the objectives was to chemically modify the laser patterned samples in order to induce nanoscale roughness. Also, it would be of great interest to analyze the cellular response to the chemically etched sample and evaluate how the nanoscale roughness influence in the cell attachment.

## Bibliography

- [1] Y. Smith, "History of Dental Implants," 26-Feb-2019. [Online]. Available: <https://www.news-medical.net/health/History-of-Dental-Implants.aspx>. [Accessed: 02-Apr-2020].
- [2] International Congress of Oral Implantologies, "History of Dental Implants," 2016. [Online]. Available: <http://www.dentalimplants.com/history-of-dental-implants.php>. [Accessed: 02-Apr-2020].
- [3] C. Mas-Moruno, B. Su, and M. J. Dalby, "Multifunctional Coatings and Nanotopographies: Toward Cell Instructive and Antibacterial Implants," *Adv. Healthc. Mater.*, vol. 8, no. 1, 2019.
- [4] R. Rajput, Z. Chouhan, M. Sindhu, S. Sundararajan, R. Raj, and S. Chouhan, "A Brief Chronological Review of Dental Implant History," *Int. Dent. J. Students Res.*, vol. 4, no. 3, pp. 105–107, 2016.
- [5] B. Poojar *et al.*, "Surface Modification Techniques for Zirconia-Based Bioceramics: A Review," *Asian J. Pharm. Clin. Res.*, vol. 11, no. 2, pp. 131–134, 2019.
- [6] A. More, "Global Dental Market Size," *Market Reports World*, 16-Jan-2020. [Online]. Available: [https://www.theexpresswire.com/pressrelease/Global-Dental-Market-Size-Share-2020-Development-Market-Trends-Key-Growth-Factors-Segmentation-and-Forecast-to-2024-Says-Market-Reports-World\\_10549107?mod=article\\_inline](https://www.theexpresswire.com/pressrelease/Global-Dental-Market-Size-Share-2020-Development-Market-Trends-Key-Growth-Factors-Segmentation-and-Forecast-to-2024-Says-Market-Reports-World_10549107?mod=article_inline). [Accessed: 02-Apr-2020].
- [7] S. Group, "Markets - Leadership strengthened in a CHF 7 billion market," 2016.
- [8] P. Claude, "3D-Printing of 8Y-TZP solid oxide fuel cell electrolytes," Politechnic University of Catalonia, 2019.
- [9] M. M. Abdul-Monem, "Zirconia overview," *Health and medicine*, 2017. [Online]. Available: <https://es.slideshare.net/MohamedMahmoud443/zirconia-overview>. [Accessed: 23-Mar-2020].
- [10] C. Holzhammer, "Micromechanics of laser modified dental zirconia ceramics," Universidad Polit cnica de Catalu a, 2015.
- [11] M. C. S. Sajjan, "An Overview on Zirconia," *TPDI*, vol. 2, no. 1, pp. 32–39, 2015.
- [12] A. Moreno Fina, "" Caracteritzaci  microestructural i mec nica de multicapes base zirc nia per," Universitat Polit cnica de Catalunya, 2016.
- [13] D. L. Moreno, "Impressi  3D de materials cer mics base zirc nia per aplicacions dentals," Universitat Polit cnica de Catalunya, 2016.
- [14] J. O. Burgess, "Zirconia: The Material, Its Evolution, and Composition | Special Issues," *Compend. Contin. Educ. Dent.*, vol. 39, no. 4, Oct. 2018.
- [15] Q. Flamant, "Surface modification of zirconia- based bioceramics for orthopedic and dental

applications,” Politechnic University of Catalonia, 2016.

- [16] C. Monaco, “Zirconia in Dentistry,” Alma Mater Studiorum Universita’ Di Bologna, 2014.
- [17] I. Denry and J. R. Kelly, “State of the art of zirconia for dental applications,” *Dent. Mater.*, vol. 24, no. 3, pp. 299–307, 2008.
- [18] R. H. J. Hannink, P. M. Kelly, and B. C. Muddle, “Transformation Toughening in ZrO<sub>2</sub>-Containing Ceramics,” *J. Am. Ceram. Soc.*, vol. 83, no. 3, pp. 461–487, 2000.
- [19] A. Della Bona, O. E. Pecho, and R. Alessandretti, “Zirconia as a dental biomaterial,” *Materials (Basel)*, vol. 8, no. 8, pp. 4978–4991, 2015.
- [20] M. Turon Viñas, “Mechanical properties of yttria-stabilized zirconia ceramics,” Universitat Politècnica de Catalunya (UPC), 2011.
- [21] E. Roitero, “Laser micro-patterning of dental zirconia : effects on microstructure and reliability Laser micro-patterning of dental zirconia : effects on microstructure and reliability,” Politechnic University of Catalonia, 2018.
- [22] J. D. Osorio, A. Lopera-Valle, A. Toro, and J. P. Hernández-Ortiz, “Transformaciones de fase en recubrimientos de barrera térmica de zirconia estabilizada con yttria depositados mediante aspersión por plasma atmosférico,” *DYNA*, vol. 81, no. 185, pp. 13–18, 2014.
- [23] J. A. Muñoz-tabares, “An overview of zirconia ceramics - structure, properties and applications,” pp. 1–18.
- [24] T. R. Ramesh, M. Gangaiah, P. V. Harish, U. Krishnakumar, and B. Nandakishore, “Zirconia Ceramics as a Dental Biomaterial,” *Trends. Biomater. Artif. Organs*, vol. 26, no. 3, pp. 154–160, 2012.
- [25] H. Qin and X. Huang, “Microstructure and Bending Strength of 3Y-TZP/12Ce-TZP Ceramics Fabricated by Liquid-Phase Sintering at Low Temperature,” *J. Am. Ceram. Soc.*, vol. 83, no. 11, pp. 2881–2883, 2004.
- [26] D. Casellas, A. Feder, L. Llanes, and M. Anglada, “Fracture toughness and mechanical strength of Y-TZP / PSZ ceramics,” *Scr. Mater.*, vol. 45, pp. 213–220, 2001.
- [27] R. H. J. Hannink and A. J. Hill, *Nanostructure Control of Materials*, Woodhead publishing. 2006.
- [28] P. M. Kelly and L. R. F. Rose, “The martensitic transformation in ceramics and its role in transformation toughening,” vol. 47, pp. 463–557, 2002.
- [29] S. Deville, A. Chevalier, and L. Gremillard, “Influence of surface finish and residual stresses on the ageing sensitivity of biomedical grade zirconia,” *Biomaterials*, vol. 27, pp. 2186–2192, 2006.
- [30] J. R. Kelly and I. Denry, “Stabilized zirconia as a structural ceramic,” *Dent. Mater.*, vol. 24, pp. 289–298, 2008.
- [31] S. Ban, “Reliability and properties of core materials for all-ceramic dental restorations,” *Jpn.*

*Dent. Sci. Rev.*, vol. 44, no. 1, pp. 3–21, 2008.

- [32] Q. Qin and J. Ye, *Toughening Mechanisms in Composite Materials*. Elsevier, 2015.
- [33] V. Gopal and G. Manivasagam, “Zirconia-alumina composite for orthopedic implant application,” *Appl. Nanocomposite Mater. Orthop.*, pp. 201–219, 2019.
- [34] E. P. Butler, “Transformation-toughened zirconia ceramics,” *Mater. Sci. Technol.*, vol. 1, no. 6, pp. 417–432, 1985.
- [35] R. O. Ritchie, J. H. Kinney, J. J. Kruzic, and R. K. Nalla, “A fracture mechanics and mechanistic approach to the failure of cortical bone,” *Fatigue Fract. Eng. Mater. Struct.*, vol. 28, no. 4, pp. 345–371, 2005.
- [36] A. O. Zhigachev, A. V. Umrikhin, and V. V. Rodaev, “Theoretical description of zirconia ceramics aging kinetics,” *J. Aust. Ceram. Soc.*, 2018.
- [37] K. Ěástková, H. Hadraba, and J. Cihlák, “Hydrothermal ageing of tetradonal zirconia ceramics,” *cERAMICS*, vol. 48, no. 3, pp. 85–92, 2004.
- [38] K. Kobayashi, H. Kuwajima, and T. Masaki, “Phase change and mechanical properties of ZrO<sub>2</sub>-Y<sub>2</sub>O<sub>3</sub> solid electrolyte after ageing,” *Solid State Ionics*, vol. 4, no. 3, pp. 489–493, 1981.
- [39] J. Chevalier, “What future for zirconia as a biomaterial?,” *Biomaterials*, vol. 27, pp. 535–543, 2006.
- [40] E. Jiménez-Piqué *et al.*, “Focused ion beam tomography of zirconia degraded under hydrothermal conditions,” *J. Eur. Ceram. Soc.*, vol. 32, no. 10, pp. 2129–2136, 2012.
- [41] Y. Gaillard, E. Jiménez-Piqué, F. Soldera, F. Mücklich, and M. Anglada, “Quantification of hydrothermal degradation in zirconia by nanoindentation,” *Acta Mater.*, vol. 56, pp. 4206–4216, 2008.
- [42] F. Zhang *et al.*, “3Y-TZP ceramics with improved hydrothermal degradation resistance and fracture toughness,” *J. Eur. Ceram. Soc.*, vol. 34, no. 10, pp. 2453–2463, 2020.
- [43] D. Tovar-vargas, M. Turon-vinas, M. Anglada, and E. Jimenez-pique, “Enhancement of mechanical properties of ceria-calcia stabilized zirconia by alumina reinforcement,” *J. Eur. Ceram. Soc.*, pp. 1–9, 2020.
- [44] K. Dorado-bustamante and S. Leal-marin, “Electrochemical analysis of the degradation of nitrated zirconia 3Y,” vol. 85, no. 206, pp. 9–15, 2018.
- [45] B. Wójtowicz, W. Pyda, and A. Labuz, “Monoclinic zirconia sintered bodies prepared via two-step sintering and characterisation of selected mechanical properties,” *Ceram. - Silikaty*, vol. 57, no. 3, pp. 185–189, 2013.
- [46] J. Eichler, U. Eisele, and J. Rödel, “Mechanical properties of monoclinic zirconia,” *J. Am. Ceram. Soc.*, vol. 87, no. 7, pp. 1401–1403, 2004.

- [47] C. Piconi and G. Maccauro, "Zirconia as a biomaterial," *Biomaterials*, vol. 20, pp. 1–25, 1997.
- [48] J. D. Lin and J. G. Duh, "Fracture toughness and hardness of ceria- and yttria-doped tetragonal zirconia ceramics," *Mater. Chem. Phys.*, vol. 78, pp. 253–261, 2003.
- [49] L. Donzel and S. G. Roberts, "Microstructure and mechanical properties of cubic zirconia (8YSZ)/SiC nanocomposites," *J. Eur. Ceram. Soc.*, vol. 20, pp. 2457–2462, 2000.
- [50] The Royal Society of Chemistry, "What are Densities of Monoclinic, Tetragonal, and Cubic Zirconia?," *Research gate*, 2016. [Online]. Available: [https://www.researchgate.net/post/What\\_are\\_Densities\\_of\\_Monoclinic\\_Tetragonal\\_and\\_Cubic\\_Zirconia](https://www.researchgate.net/post/What_are_Densities_of_Monoclinic_Tetragonal_and_Cubic_Zirconia). [Accessed: 23-Apr-2020].
- [51] "Características y aplicaciones de la cerámica estructural de zirconia," *Textos Científicos*, 2006. [Online]. Available: <https://www.textoscientificos.com/quimica/ceramicas-avanzadas/caracteristicas-aplicaciones-zirconia>. [Accessed: 30-Mar-2020].
- [52] S. Weng, "Zirconia Ceramic Structural Parts VS Auto Parts ," 07-Nov-2018. [Online]. Available: <http://www.zirconiumworld.com/zirconia-ceramic-structural-parts-vs-auto-parts/>. [Accessed: 25-Apr-2020].
- [53] C. Cristache, G. Cristache, and S. Drafta, "Zirconia and its biomedical applications," *Met. Int.*, vol. 16, no. 7, pp. 18–23, 2011.
- [54] Sunrise Refractory Co., "The Application Of Zirconia Refractories In Glass Furnaces," 03-Jun-2015. [Online]. Available: <http://www.fusedazs.com/news/73.html>. [Accessed: 25-Apr-2020].
- [55] "Inch New Hot Sale Zirconia Ceramic Knives Single branch Ceramic Knife Fruit Cutter Kitchen Accessories Knife Watermelon," *Bee Clean Products*. [Online]. Available: <http://beecleanhome.com/product/7-inch-new-hot-sale-zirconia-ceramic-knives-single-branch-ceramic-knife-fruit-cutter-kitchen-accessories-knife-watermelon/>. [Accessed: 25-Apr-2020].
- [56] NGK SPARK PLUG CO, "Zirconia Oxygen Sensor." [Online]. Available: [https://www.ngkntk.co.jp/english/product/sensors\\_plugs/zirconia\\_oxygen.html](https://www.ngkntk.co.jp/english/product/sensors_plugs/zirconia_oxygen.html). [Accessed: 25-Apr-2020].
- [57] C. Y. Hu and T. R. Yoon, "Recent updates for biomaterials used in total hip arthroplasty," *Biomater. Res.*, vol. 22, no. 33, pp. 1–12, 2018.
- [58] S. G. Ghalme, A. Mankar, and Y. Bhalerao, "Biomaterials in Hip Joint Replacement," *Int. J. Mater. Sci. Eng.*, vol. 4, no. 2, pp. 113–125, 2016.
- [59] Y. Kawai, M. Uo, Y. Wang, S. Kono, S. Ohnuki, and F. Watari, "Phase transformation of zirconia ceramics by hydrothermal degradation," *Dent. Mater. J.*, vol. 30, no. 3, pp. 286–292, 2011.
- [60] A. J. Raigrodski, M. B. Hillstead, G. K. Meng, and K. H. Chung, "Survival and complications of zirconia-based fixed dental prostheses: A systematic review," *Journal of Prosthetic Dentistry*, vol. 107, no. 3. Mosby Inc., pp. 170–177, 2012.

- [61] R. K. Chimpatali, "Influence of sandblasting on zirconia in restorative dentistry," Politecnico University of Catalunya, 2012.
- [62] Dental Solutions, "Know more about zirconia crowns | Dental Solutions," *American Dental Association*, 16-Oct-2017. [Online]. Available: <https://dentalsolutionsalgodones.com/know-zirconia-crowns/>. [Accessed: 31-Mar-2020].
- [63] P. F. Manicone, P. Rossi Iommetti, and L. Raffaelli, "An overview of zirconia ceramics: Basic properties and clinical applications," *J. Dent.*, vol. 35, no. 11, pp. 819–826, 2007.
- [64] C. Gautam, J. Joyner, A. Gautam, J. Rao, and R. Vajtai, "Zirconia based dental ceramics: structure, mechanical properties, biocompatibility and applications," *Dalt. Trans.*, no. November, 2016.
- [65] C. Larsson and A. Wennerberg, "The Clinical Success of Zirconia-Based Crowns: A Systematic Review," *Int. J. Prosthodont.*, vol. 27, no. 1, pp. 33–43, Jan. 2014.
- [66] R. Brignardello-Petersen, "High proportion of all-ceramic zirconia tooth-supported crowns survive after 5 years," *Journal of the American Dental Association*, vol. 148, no. 10. American Dental Association, p. e142, 01-Oct-2017.
- [67] Y. Cao, C. Yu, Y. Wu, L. Li, and C. Li, "Long-Term Survival and Peri-Implant Health of Titanium Implants with Zirconia Abutments: A Systematic Review and Meta-Analysis," *Journal of Prosthodontics*, vol. 28, no. 8. Blackwell Publishing Inc., pp. 883–892, 01-Oct-2019.
- [68] A. Zembic and R. J. Kohal, "Performance of Zirconia for Dental Healthcare," pp. 863–896, 2010.
- [69] R. Meshramkar, P. Shetty, A. Nayak, and G. V Anehosur, "Surface Treatment of Zirconia Implant , Its Surface Roughness and Its Effect on Osseointegration - A Review," vol. 04, no. 05, pp. 343–345, 2019.
- [70] A. A. Madfa, F. A. Al-Sanabani, N. H. Al-Qudami, J. S. Al-Sanabani, and A. G. Amran, "Use of Zirconia in Dentistry: An Overview," *Open Biomater. J.*, vol. 5, no. 1, pp. 1–9, 2014.
- [71] B. Y. Farber and G. A. Graves, "Ceramic media with improved efficiency," *PCI Mag.*, 2001.
- [72] N. F. Amat, A. Muchtar, N. Yahaya, M. J. Ghazali, M. A. Aziz, and K. Lumpur, "A Review of Zirconia as a Dental Restorative Material Department of Mechanical and Materials Engineering , Faculty of Engineering and Built Department of Prosthodontic , Faculty of Dentistry , Universiti Kebangsaan Malaysia , Jalan Raja," *Aust. J. Basic Appl. Sci.*, vol. 6, no. 12, pp. 9–13, 2012.
- [73] C. A. Maziero Volpato, L. G. D. Altoe Garbelotto, M. Celso, and F. Bondioli, "Application of Zirconia in Dentistry: Biological, Mechanical and Optical Considerations," *Adv. Ceram. - Electr. Magn. Ceram. Bioceram. Ceram. Environ.*, no. June 2014, 2011.
- [74] I. Denry and J. A. Holloway, "Ceramics for dental applications: A review," *Materials (Basel).*, vol. 3, no. 1, pp. 351–368, 2010.
- [75] D. F. Williams, "On the mechanisms of biocompatibility," *Biomaterials*, vol. 29, no. 20, pp. 2941–2953, Jul. 2008.

- [76] T. Tosiriwatanapong and W. Singhatanadgit, "Zirconia-Based Biomaterials for Hard Tissue Reconstruction," *Bone Tissue Regen. Insights*, vol. 9, pp. 1–9, 2018.
- [77] H. Harianawala, M. Kheur, and A. Bal, "Biocompatibility of Zirconia," *J. Adv. Med. Dent. Sci. Res.*, vol. 4, no. 3, pp. 35–39, 2016.
- [78] I. Dion *et al.*, "Physico-chemistry and cytotoxicity of ceramics. Part I. Characterization of ceramic powders," *J. Mater. Sci. Mater. Med.*, vol. 8, no. 5, pp. 325–332, 1997.
- [79] E. Demir, D. Burgucu, F. Turna, S. Aksakal, and B. Kaya, "Determination of TiO<sub>2</sub>, ZrO<sub>2</sub>, and Al<sub>2</sub>O<sub>3</sub> nanoparticles on genotoxic responses in human peripheral blood lymphocytes and cultured embryonic kidney cells," *J. Toxicol. Environ. Heal. - Part A Curr. Issues*, vol. 76, no. 16, pp. 990–1002, 2013.
- [80] T. Sterner, N. Schütze, G. Saxler, F. Jakob, and C. P. Rader, "Effects of clinically relevant alumina ceramic particles, zirconia ceramic particles and titanium particles of different sizes and concentrations on TNF $\alpha$  release in a human monocytic cell line," *Biomed. Eng. (NY)*, vol. 49, no. 12, Mar. 2008.
- [81] H. M. T. U. Herath, L. Di Silvio, and J. R. G. Evans, "Osteoblast response to zirconia surfaces with different topographies," *Mater. Sci. Eng. C*, vol. 57, pp. 363–370, Dec. 2015.
- [82] Y. Josset, Z. Oum'hamed, A. Zarrinpour, M. Lorenzato, J. J. Adnet, and D. Laurent-Maquin, "In vitro reactions of human osteoblasts in culture with zirconia and alumina ceramics," *J. Biomed. Mater. Res.*, vol. 47, no. 4, pp. 481–493, 1999.
- [83] A. Dalal, V. Pawar, K. McAllister, C. Weaver, and N. J. Hallab, "Orthopedic implant cobalt-alloy particles produce greater toxicity and inflammatory cytokines than titanium alloy and zirconium alloy-based particles in vitro, in human osteoblasts, fibroblasts, and macrophages," *J. Biomed. Mater. Res. Part A*, vol. 100, no. 8, pp. 2147–2158, Aug. 2012.
- [84] Y. Ichikawa, Y. Akagawa, H. Nikai, and H. Tsuru, "Tissue compatibility and stability of a new zirconia ceramic in vivo," *J. Prosthet. Dent.*, vol. 68, no. 2, pp. 322–326, Aug. 1992.
- [85] P. Christel, A. Meunier, M. Heller, J. P. Torre, and C. N. Peille, "Mechanical properties and short-term in vivo evaluation of yttrium-oxide-partially-stabilized zirconia," *J. Biomed. Mater. Res.*, vol. 23, no. 1, pp. 45–61, Jan. 1989.
- [86] A. Scarano, F. Di Carlo, M. Quaranta, and A. Piattelli, "Bone response to zirconia ceramic implants: an experimental study in rabbits," *J. Oral Implantol.*, vol. 29, no. 1, pp. 8–12, 2003.
- [87] O. S. Abd El-Ghany and A. H. Sherief, "Zirconia based ceramics, some clinical and biological aspects: Review," *Futur. Dent. J.*, vol. 2, pp. 55–64, 2016.
- [88] A. B. Bavbek, M. Özcan, and G. Eskitascioglu, "Radioactive potential of zirconium-dioxide used for dental applications," *J. Appl. Biomater. Funct. Mater.*, vol. 12, no. 1, pp. 35–40, 2014.
- [89] A. Giussani, U. Gerstmann, G. Guzzi, C. La Porta, M. C. Cantone, and I. Veronese, "Natural radioactivity in zirconia-based dental ceramics," International Atomic Energy Agency, 2010.

- [90] V. V. Silva, F. S. Lameiras, and Z. I. P. Lobato, "Biological reactivity of zirconia-hydroxyapatite composites," *J. Biomed. Mater. Res.*, vol. 63, no. 5, pp. 583–590, 2002.
- [91] V. Covacci *et al.*, "In vitro evaluation of the mutagenic and carcinogenic power of high purity zirconia ceramic," *Biomaterials*, vol. 20, no. 4, pp. 371–376, Feb. 1999.
- [92] A. G. Gristina, "Biomaterial-centered infection: Microbial adhesion versus tissue integration," *Science (80-. )*, vol. 237, no. 4822, pp. 1588–1595, Sep. 1987.
- [93] G. Subbiahdoss, R. Kuijter, D. W. Grijpma, H. C. van der Mei, and H. J. Busscher, "Microbial biofilm growth vs. tissue integration: 'The race for the surface' experimentally studied," *Acta Biomater.*, vol. 5, no. 5, pp. 1399–1404, Jun. 2009.
- [94] A. T. and J. C., "Osteoinduction, osteoconduction and osseointegration," *Eur. Spine J.*, vol. 10, pp. 96–101, Oct. 2001.
- [95] A. K. Pandey, F. Pati, D. Mandal, S. Dhara, and K. Biswas, "In vitro evaluation of osteoconductivity and cellular response of zirconia and alumina based ceramics," *Mater. Sci. Eng.*, vol. 33, no. 7, pp. 3923–3930, Oct. 2013.
- [96] R. Depprich *et al.*, "Osseointegration of zirconia implants compared with titanium: An in vivo study," *Head Face Med.*, vol. 4, no. 1, pp. 1–8, 2008.
- [97] G. Marques, L. Eduardo Marques Padovan, M. Akemi Matsumoto, P. Domingos Ribeiro Júnior, E. Mattias Sartori, and M. Claudino, "Bone healing in titanium and zirconia implants surface: a pilot study on the rabbit tibia," *RSBO*, vol. 10, no. 2, pp. 110–115, 2013.
- [98] R. J. Kohal, M. Wolkewitz, M. Hinze, J. S. Han, M. Bächle, and F. Butz, "Biomechanical and histological behavior of zirconia implants: An experiment in the rat," *Clin. Oral Implants Res.*, vol. 20, no. 4, pp. 333–339, Apr. 2009.
- [99] I.-S. Yeo, H.-Y. Kim, K. S. Lim, and J.-S. Han, "Implant Surface Factors and Bacterial Adhesion," *Int. J. Artif. Organs*, vol. 35, no. 10, pp. 762–772, Oct. 2012.
- [100] R. M. Donlan, "Biofilm Formation: A Clinically Relevant Microbiological Process," *Healthc. Epidemiol.*, vol. 33, pp. 1387–1392, 2001.
- [101] E. Maunders and M. Welch, "Matrix exopolysaccharides; the sticky side of biofilm formation.," *FEMS Microbiol. Lett.*, vol. 364, no. 13, 2017.
- [102] T. S. O. Silva, A. R. Freitas, M. L. L. Pinheiro, C. Do Nascimento, E. Watanabe, and R. F. Albuquerque, "Oral biofilm formation on different materials for dental implants," *J. Vis. Exp.*, vol. 2018, no. 136, 2018.
- [103] A. Apratim, P. Eachempati, K. Krishnappa Salian, V. Singh, S. Chhabra, and S. Shah, "Zirconia in dental implantology: A review," *J. Int. Soc. Prev. Community Dent.*, vol. 5, no. 3, p. 156, 2015.
- [104] A. S. Meza-Siccha, M. A. Aguilar-Luis, W. Silva-Caso, F. Mazulis, C. Barragan-Salazar, and J. del Valle-Mendoza, "In Vitro Evaluation of Bacterial Adhesion and Bacterial Viability of Streptococcus mutans, Streptococcus sanguinis, and Porphyromonas gingivalis on the



Abutment Surface of Titanium and Zirconium Dental Implants," *Int. J. Dent.*, 2019.

- [105] A. Scarano, M. Piattelli, S. Caputi, G. A. Favero, and A. Piattelli, "Bacterial Adhesion on Commercially Pure Titanium and Zirconium Oxide Disks: An In Vivo Human Study," *J. Periodontol.*, vol. 75, no. 2, pp. 292–296, Feb. 2004.
- [106] L. Rimondini, L. Cerroni, A. Carrassi, and P. Torricelli, "Bacterial Colonization of Zirconia Ceramic Surfaces: An in Vitro and in Vivo Study," *Int. J. oral Maxillofac. Implant.*, vol. 17, no. 6, pp. 793–800, 2002.
- [107] S. Anil, P. S. Anand, H. Alghamdi, and J. A. Jansen, "Dental Implant Surface Enhancement and Osseointegration," in *Implant Dentistry: A Rapidly Evolving Practice*, I. Turkyilmaz, Ed. cROATIA: InTech, 2011.
- [108] L. Sennerby, A. Dasmah, B. Larsson, and M. Iverhed, "Bone Tissue Responses to Surface-Modified Zirconia Implants: A Histomorphometric and Removal Torque Study in the Rabbit," *Clin. Implant Dent. Relat. Res.*, vol. 7, no. 1, pp. 13–20, 2005.
- [109] S. A. Hacking *et al.*, "Surface roughness enhances the osseointegration of titanium headposts in non-human primates," *J. Neurosci. Methods*, vol. 211, no. 2, pp. 237–244, Nov. 2012.
- [110] T. Albrektsson and A. Wennerberg, "Oral Implant Surfaces: Part 1--review Focusing on Topographic and Chemical Properties of Different Surfaces and in Vivo Responses to Them - PubMed," *Int J Prosthodont*, vol. 17, no. 5, pp. 536–543, 2004.
- [111] A. Bravo-Leon, Y. Morikawa, M. Kawahara, and M. J. Mayo, "Fracture toughness of nanocrystalline tetragonal zirconia with low yttria content," *Acta Mater.*, vol. 50, no. 18, pp. 4555–4562, 2002.
- [112] A. L. Rosa and M. M. Beloti, "Effect of cpTi surface roughness on human bone marrow cell attachment, proliferation, and differentiation," *Braz. Dent. J.*, vol. 14, no. 1, pp. 16–21, 2003.
- [113] L. Karygianni *et al.*, "Initial Bacterial Adhesion on Different Yttria-Stabilized Tetragonal Zirconia Implant Surfaces in Vitro," *Materials (Basel)*, vol. 6, no. 12, pp. 5659–5674, Dec. 2013.
- [114] R. Krishna Alla, K. Ginjupalli, N. Upadhy, M. Shammas, R. Krishna Ravi, and R. Sekhar, "Surface Roughness of Implants: A Review," 2011.
- [115] S. Lossdörfer *et al.*, "Microrough implant surface topographies increase osteogenesis by reducing osteoclast formation and activity," *J. Biomed. Mater. Res. - Part A*, vol. 70, no. 3, pp. 361–369, Sep. 2004.
- [116] B. D. Boyan *et al.*, "Osteoblasts generate an osteogenic microenvironment when grown on surfaces with rough microtopographies," *Eur. Cells Mater.*, vol. 6, pp. 22–27, 2003.
- [117] A. Wennerberg and T. Albrektsson, "Effects of titanium surface topography on bone integration: A systematic review," *Clinical Oral Implants Research*, vol. 20, no. SUPPL. 4. Clin Oral Implants Res, pp. 172–184, Sep-2009.
- [118] M. J. P. Biggs *et al.*, "Interactions with nanoscale topography: Adhesion quantification and signal

- transduction in cells of osteogenic and multipotent lineage," *J. Biomed. Mater. Res. - Part A*, vol. 91, no. 1, pp. 195–208, 2009.
- [119] M. J. Dalby, D. McCloy, M. Robertson, C. D. W. Wilkinson, and R. O. C. Oreffo, "Osteoprogenitor response to defined topographies with nanoscale depths," *Biomaterials*, vol. 27, no. 8, pp. 1306–1315, Mar. 2006.
  - [120] D. Karazisis *et al.*, "The influence of controlled surface nanotopography on the early biological events of osseointegration," *Acta Biomater.*, vol. 53, pp. 559–571, Apr. 2017.
  - [121] P. G. Coelho, R. Jimbo, N. Tovar, and E. A. Bonfante, "Osseointegration: Hierarchical designing encompassing the micrometer, micrometer, and nanometer length scales," *Dent. Mater.*, vol. 31, pp. 37–52, 2015.
  - [122] L. Meirelles *et al.*, "Effect of hydroxyapatite and titania nanostructures on early in vivo bone response," *Clin. Implant Dent. Relat. Res.*, vol. 10, no. 4, pp. 245–254, Dec. 2008.
  - [123] M. Lorenzetti *et al.*, "The influence of surface modification on bacterial adhesion to titanium-based substrates," *ACS Appl. Mater. Interfaces*, vol. 7, no. 3, pp. 1644–1651, Jan. 2015.
  - [124] N. Mitik-Dineva, J. Wang, R. C. Mocanasi, P. R. Stoddart, R. J. Crawford, and E. P. Ivanova, "Impact of nano-topography on bacterial attachment," *Biotechnol. J.*, vol. 3, no. 4, pp. 536–544, Apr. 2008.
  - [125] P. Yu, C. Wang, J. Zhou, L. Jiang, J. Xue, and W. Li, "Influence of Surface Properties on Adhesion Forces and Attachment of Streptococcus mutans to Zirconia In Vitro," *Biomed Res. Int.*, vol. 2016, 2016.
  - [126] Y. Shalaby, S. S. Omar, D. Mostafa, and H. M. Fahmy, "Influence of Laser and Ultraviolet Surface Modification Strategies on Zirconia Implants Osseointegration in Rabbits : In vitro -Histological study," *J. Am. Science*, vol. 14, no. 12, 2018.
  - [127] T. Ma, X. Ge, Y. Zhang, and Y. Lin, "Effect of Titanium Surface Modifications of Dental Implants on Rapid Osseointegration," in *Interface Oral Health Science 2016*, Springer Singapore, 2017, pp. 247–256.
  - [128] S. C. Sartoretto, A. T. N. N. Alves, R. F. B. Resende, J. Calasans-Maia, J. M. Granjeiro, and M. D. Calasans-Maia, "Early osseointegration driven by the surface chemistry and wettability of dental implants," *J. Appl. Oral Sci.*, vol. 23, no. 3, pp. 272–278, Jul. 2015.
  - [129] G. Zhao *et al.*, "High surface energy enhances cell response to titanium substrate microstructure," *J. Biomed. Mater. Res. - Part A*, vol. 74, no. 1, pp. 49–58, Jul. 2005.
  - [130] F. E. Pinotti, G. J. P. L. de Oliveira, M. A. T. Aroni, R. A. C. Marcantonio, and E. Marcantonio, "Analysis of osseointegration of implants with hydrophilic surfaces in grafted areas: A Preclinical study," *Clin. Oral Implants Res.*, vol. 29, no. 10, pp. 963–972, Oct. 2018.
  - [131] N. P. Lang, G. E. Salvi, G. Huynh-Ba, S. Ivanovski, N. Donos, and D. D. Bosshardt, "Early osseointegration to hydrophilic and hydrophobic implant surfaces in humans," *Clin. Oral Implants Res.*, vol. 22, no. 4, pp. 349–356, Apr. 2011.

- [132] S. Usami, H. Kimoto, I. Takahashi, and S. Shida, "Strength of ceramic materials containing small flaws," *Eng. Fract. Mech.*, vol. 23, no. 4, pp. 745–761, 1986.
- [133] R. E. Chin, "Grinding and Polishing," in *Ceramography: Preparation and Analysis of Ceramic Microstructures*, OH: ASM International, 2002, pp. 35–44.
- [134] W. Khayat, N. Chebib, M. Finkelman, S. Khayat, and A. Ali, "Effect of grinding and polishing on roughness and strength of zirconia," *J. Prosthet. Dent.*, vol. 119, no. 4, pp. 626–631, 2018.
- [135] B. Asmus, "How to do slag microscopy - sample lapping," *archaeometallurgy*, 26-Jan-2014. [Online]. Available: <http://en.archaeometallurgie.de/tag/how-to/page/3/>. [Accessed: 05-Apr-2020].
- [136] J. A. Muñoz-Tabares, E. Jiménez-Piqué, J. Reyes-Gasga, and M. Anglada, "Microstructural changes in ground 3Y-TZP and their effect on mechanical properties," *Acta Mater.*, vol. 59, no. 17, pp. 6670–6683, 2011.
- [137] J. Minguella, M. P. Ginebra, L. Llanes, C. Mas-Moruno, and J. J. Roa, "Influence of grinding/polishing on the mechanical, phase stability and cell adhesion properties of yttria-stabilized zirconia," *J. Eur. Ceram. Soc.*, 2020.
- [138] H. H. Huang, C. Te Ho, T. H. Lee, T. L. Lee, K. K. Liao, and F. L. Chen, "Effect of surface roughness of ground titanium on initial cell adhesion," *Biomol. Eng.*, vol. 21, pp. 93–97, 2004.
- [139] X. Lai, W. Si, D. Jiang, T. Sun, L. Shao, and B. Deng, "Effects of small-grit grinding and glazing on mechanical behaviors and ageing resistance of a super-translucent dental zirconia," *J. Dent.*, vol. 66, pp. 23–31, 2017.
- [140] G. Soon, B. Pingguan-Murphy, K. W. Lai, and S. A. Akbar, "Review of zirconia-based bioceramic: Surface modification and cellular response," *Ceram. Int.*, vol. 42, no. 11, pp. 12543–12555, 2016.
- [141] J.-H. Lee, H.-S. Kim, A. Pae, and Y.-H. Woo, "Influence of sandblasting and primer on shear bond strength of resin cement to zirconia," *J. Korean Acad. Prosthodont.*, vol. 49, no. 1, pp. 49–56, 2011.
- [142] B. Bacchelli *et al.*, "Influence of a zirconia sandblasting treated surface on peri-implant bone healing: An experimental study in sheep," *Acta Biomater.*, vol. 5, no. 6, pp. 2246–2257, Jul. 2009.
- [143] M. Gahlert, S. Roehling, C. M. Sprecher, H. Kniha, S. Milz, and K. Bormann, "In vivo performance of zirconia and titanium implants: a histomorphometric study in mini pig maxillae," *Clin. Oral Implants Res.*, vol. 23, no. 3, pp. 281–286, Mar. 2012.
- [144] L. Hallmann, P. Ulmer, E. Reusser, and C. H. F. Hämmerle, "Effect of blasting pressure, abrasive particle size and grade on phase transformation and morphological change of dental zirconia surface," *Surf. Coatings Technol.*, vol. 206, pp. 4293–4302, 2012.
- [145] T. Kosmač, C. Oblak, P. Jevnikar, N. Funduk, and L. Marion, "The effect of surface grinding and sandblasting on flexural strength and reliability of Y-TZP zirconia ceramic," *Dent. Mater.*, vol.

15, no. 6, pp. 426–433, 1999.

- [146] T. Kosmač, C. Oblak, and L. Marion, “The effects of dental grinding and sandblasting on ageing and fatigue behavior of dental zirconia (Y-TZP) ceramics,” *J. Eur. Ceram. Soc.*, vol. 28, pp. 1085–1090, 2008.
- [147] C. F. Caravaca, Q. Flamant, M. Anglada, L. Gremillard, and J. Chevalier, “Impact of sandblasting on the mechanical properties and aging resistance of alumina and zirconia based ceramics,” *J. Eur. Ceram. Soc.*, vol. 38, no. 3, pp. 915–925, Mar. 2018.
- [148] N. Ziozios, E. Kontonasaki, N. Kantiranis, L. Papadopoulou, Y. Papadogiannis, and # Petros Koidis, “The influence of sandblasting and aging on Y-TZP ceramic during static and dynamic loading,” *Ceramics-Silikáty*, vol. 61, no. 2, pp. 81–90, 2017.
- [149] Q. Flamant, F. García Marro, J. J. Roa Rovira, and M. Anglada, “Hydrofluoric acid etching of dental zirconia. Part 1: Etching mechanism and surface characterization,” *J. Eur. Ceram. Soc.*, vol. 36, no. 1, pp. 121–134, 2016.
- [150] G.-J. Oh *et al.*, “Surface Characteristics of Bioactive Glass-Infiltrated Zirconia with Different Hydrofluoric Acid Etching Conditions,” *J. Nanosci. Nanotechnol.*, vol. 17, no. 4, pp. 2645–2648, Apr. 2017.
- [151] L. Cooper *et al.*, “Fluoride modification effects on osteoblast behavior and bone formation at TiO grit-blasted c.p. titanium endosseous implants,” *Biomaterials*, vol. 27, no. 6, pp. 926–936, Feb. 2006.
- [152] M. Yoshinari, Y. Oda, T. Kato, and K. Okuda, “Influence of surface modifications to titanium on antibacterial activity in vitro,” *Biomaterials*, vol. 22, no. 14, pp. 2043–2048, Jan. 2001.
- [153] H. ITO, H. SASAKI, K. SAITO, S. HONMA, Y. YAJIMA, and M. YOSHINARI, “Response of osteoblast-like cells to zirconia with different surface topography,” *Dent. Mater. J.*, vol. 32, no. 1, pp. 122–129, 2013.
- [154] C. Bergemann *et al.*, “Microstructured zirconia surfaces modulate osteogenic marker genes in human primary osteoblasts,” *J. Mater. Sci. Mater. Med.*, vol. 26, no. 1, p. 26, Jan. 2015.
- [155] N. Saulacic, R. Erdösi, D. D. Bosshardt, R. Gruber, and D. Buser, “Acid and Alkaline Etching of Sandblasted Zirconia Implants: A Histomorphometric Study in Miniature Pigs,” *Clin. Implant Dent. Relat. Res.*, vol. 16, no. 3, pp. 313–322, Jun. 2014.
- [156] Q. Flamant and M. Anglada, “Hydrofluoric acid etching of dental zirconia. Part 2: effect on flexural strength and ageing behavior,” *J. Eur. Ceram. Soc.*, vol. 36, no. 1, pp. 135–145, Jan. 2016.
- [157] H. Xie, S. Shen, M. Qian, F. Zhang, C. Chen, and F. R. Tay, “Effects of acid treatment on dental zirconia: An in vitro study,” *PLoS One*, vol. 10, no. 8, pp. 1–12, 2015.
- [158] E. Roitero, F. Lasserre, J. J. Roa, M. Anglada, F. Mücklich, and E. Jiménez-Piqué, “Nanosecond-laser patterning of 3Y-TZP: Damage and microstructural changes,” *J. Eur. Ceram. Soc.*, vol. 37, no. 15, pp. 4876–4887, 2017.

- [159] L. Hao and J. Lawrence, "Effects of CO<sub>2</sub> laser irradiation on the wettability and human skin fibroblast cell response of magnesia partially stabilised zirconia," *Mater. Sci. Eng. C*, vol. 23, no. 5, pp. 627–639, Oct. 2003.
- [160] J. Lawrence and L. Li, "On the mechanisms of wetting characteristics modification for selected metallic materials by means of high power diode laser radiation," *J. Laser Appl.*, vol. 14, no. 2, pp. 107–113, May 2002.
- [161] N. M. Rezaei *et al.*, "Biological and osseointegration capabilities roughened zirconia," *Int. J. of Nanomedicine*, vol. 13, pp. 3381–3395, 2018.
- [162] A. Carvalho, L. Canguero, V. Oliveira, R. Vilar, M. H. Fernandes, and F. J. Monteiro, "Femtosecond laser microstructured Alumina toughened Zirconia: A new strategy to improve osteogenic differentiation of hMSCs," *Appl. Surf. Sci.*, vol. 435, pp. 1237–1245, 2018.
- [163] A. M. Stanciuc, Q. Flamant, C. M. Sprecher, M. Alini, M. Anglada, and M. Peroglio, "Femtosecond laser multi-patterning of zirconia for screening of cell-surface interactions," *J. Eur. Ceram. Soc.*, vol. 38, pp. 939–948, 2018.
- [164] O. Hoffmann, N. Angelov, G.-G. Zafiropoulos, and S. Andreana, "Osseointegration of zirconia implants with different surface characteristics: an evaluation in rabbits," *Int. J. Oral Maxillofac. Implants*, vol. 27, no. 2, pp. 352–358, 2012.
- [165] J. P. Parry, J. D. Shephard, F. C. Dear, N. Jones, N. Weston, and D. P. Hand, "Nanosecond-Laser Postprocessing of Millisecond- Laser-Machined Zirconia (Y-TZP) Surfaces," *Int. J. Appl. Ceram. Technol.*, vol. 5, no. 3, pp. 249–257, May 2008.
- [166] J. P. Parry, J. D. Shephard, D. P. Hand, C. Moorhouse, N. Jones, and N. Weston, "Laser Micromachining of Zirconia (Y-TZP) Ceramics in the Picosecond Regime and the Impact on Material Strength," *Int. J. Appl. Ceram. Technol.*, vol. 8, no. 1, pp. 163–171, Jan. 2011.
- [167] E. Roitero, M. Anglada, F. Mücklich, and E. Jiménez-Piqué, "Mechanical reliability of dental grade zirconia after laser patterning," 2018.
- [168] E. Roitero, M. Ochoa, M. Anglada, F. Mücklich, and E. Jiménez-Piqué, "Low temperature degradation of laser patterned 3Y-TZP: Enhancement of resistance after thermal treatment," *J. Eur. Ceram. Soc.*, vol. 38, no. 4, pp. 1742–1749, 2018.
- [169] C. Daniel, J. Drummond, and R. A. Giordano, "Improving Flexural Strength of Dental Restorative Ceramics Using Laser Interference Direct Structuring," *J. Am. Ceram. Soc.*, vol. 91, no. 10, pp. 3455–3457, Oct. 2008.
- [170] A. Han, J. K. H. Tsoi, J. P. Matinlinna, Y. Zhang, and Z. Chen, "Effects of different sterilization methods on surface characteristics and biofilm formation on zirconia in vitro," *Dent. Mater.*, 2017.
- [171] Y. A. Hag Elkhidir and Y. Cheng, "Achieving Superosseointegration: The Photofunctionalization Effect," *Dentistry*, vol. 7, no. 435, 2017.
- [172] H. E. Blum, "Effect of UV treatment on the osteoconductivity of a zirconia-based implant

material,” Albert-Ludwigs-Universität, 2012.

- [173] T. Tuna, M. Wein, B. Altmann, T. Steinberg, J. Fischer, and W. Att, “Effect of ultraviolet photofunctionalisation on the cell attractiveness of Zirconia implant materials,” *Eur. Cells Mater.*, vol. 29, pp. 82–96, 2015.
- [174] M. Brezavšček, A. Fawzy, M. Bächle, T. Tuna, J. Fischer, and W. Att, “The effect of UV treatment on the osteoconductive capacity of zirconia-based materials,” *Materials (Basel)*, vol. 9, no. 958, 2016.
- [175] W. Att, M. Takeuchi, T. Suzuki, K. Kubo, M. Anpo, and T. Ogawa, “Enhanced osteoblast function on ultraviolet light-treated zirconia,” *Biomaterials*, vol. 30, no. 7, pp. 1273–1280, Mar. 2009.
- [176] A. Henningsen *et al.*, “Changes in surface characteristics of titanium and zirconia after surface treatment with ultraviolet light or non-thermal plasma,” *Eur. J. Oral Sci.*, pp. 1–9, 2018.
- [177] T. Tuna, M. Wein, M. Swain, J. Fischer, and W. Att, “Influence of ultraviolet photofunctionalization on the surface characteristics of zirconia-based dental implant materials,” *Dent. Mater.*, no. 2, 2014.
- [178] A. Han, H. Ding, J. K. H. Tsoi, S. Imazato, J. P. Matinlinna, and Z. Chen, “Prolonged UV-C Irradiation is a Double-Edged Sword on the Zirconia Surface,” *ACS Appl. Mater. Interfaces*, 2020.
- [179] Y. Iinuma, M. Hirota, T. Hayakawa, and C. Ohkubo, “Surrounding tissue response to surface-treated zirconia implants,” *Materials (Basel)*, vol. 13, no. 30, pp. 1–14, 2020.
- [180] F. H. Schünemann *et al.*, “Zirconia surface modifications for implant dentistry,” *Mater. Sci. Eng. C*, vol. 98, pp. 1294–1305, 2019.
- [181] C. Ying Kei Lung, “Surface coatings of titanium and zirconia,” *Adv. Mater. Sci.*, vol. 2, no. 2, pp. 1–3, 2017.
- [182] Y. Cho, J. Hong, H. Ryoo, D. Kim, J. Park, and J. Han, “Osteogenic responses to zirconia with hydroxyapatite coating by aerosol deposition,” *J. Dent. Res.*, vol. 94, no. 3, pp. 491–499, 2015.
- [183] D. Mostafa and M. Aboushelib, “Bioactive–hybrid–zirconia implant surface for enhancing osseointegration: an in vivo study,” *Int. J. Implant Dent.*, vol. 4, no. 20, 2018.
- [184] A. I. Kozelskaya *et al.*, “Modification of the ceramic implant surfaces from zirconia by the magnetron sputtering of different calcium phosphate targets: A comparative study,” *Materials (Basel)*, vol. 11, no. 10, 2018.
- [185] M. Ortiz-Hernandez *et al.*, “Two different strategies to enhance osseointegration in porous titanium: Inorganic thermo-chemical treatment versus organic coating by peptide adsorption,” *Int. J. Mol. Sci.*, vol. 19, no. 2574, 2018.
- [186] B. Moore, E. Asadi, and G. Lewis, “Deposition methods for Microstructured and Nanostructured coatings on metallic bone implants: A review,” *Adv. Mater. Sci. Eng.*, 2017.
- [187] K. Zhang and Q. Van Le, “Bioactive glass coated zirconia for dental implants,” *Compos. Compd.*,

vol. 2, pp. 10–17, 2019.

- [188] H. Wang, N. Eliaz, Z. Xiang, H. P. Hsu, M. Spector, and L. W. Hobbs, “Early bone apposition in vivo on plasma-sprayed and electrochemically deposited hydroxyapatite coatings on titanium alloy,” *Biomaterials*, vol. 27, no. 23, pp. 4192–4203, Aug. 2006.
- [189] J. H. Sørensen *et al.*, “Biomimetic Hydroxyapatite Coated Titanium Screws Demonstrate Rapid Implant Stabilization and Safe Removal &lt;i>In-Vivo&/i>,” *J. Biomater. Nanobiotechnol.*, vol. 6, pp. 20–35, 2015.
- [190] G. L. Darimont, R. Cloots, E. Heinen, L. Seidel, and R. Legrand, “In vivo behaviour of hydroxyapatite coatings on titanium implants: A quantitative study in the rabbit,” *Biomaterials*, vol. 23, no. 12, pp. 2569–2575, 2002.
- [191] R. Bloebaum, M. Merrell, K. Gustke, and M. Simmons, “Retrieval analysis of a hydroxyapatite-coated hip prosthesis. - PubMed - NCBI,” *Clin. Orthop. Relat. Res.*, vol. 267, no. 97, pp. 97–102, 1991.
- [192] S. Omar *et al.*, “Sol-gel hybrid coatings with strontium-doped 45S5 glass particles for enhancing the performance of stainless steel implants: Electrochemical, bioactive and in vivo response,” *J. Non. Cryst. Solids*, vol. 425, pp. 1–10, Oct. 2015.
- [193] A. Merolli, C. Gabbi, M. Santin, B. Locardi, and P. Leali, “Bioactive Glass Coatings on Ti6Al4V Promote the Tight Apposition of Newly-Formed Bone In Vivo | Request PDF,” *Key Eng. Mater.*, pp. 789–792, 2004.
- [194] V. Stanic *et al.*, “Osteointegration of bioactive glass-coated zirconia in healthy bone: An in vivo evaluation,” *Biomaterials*, vol. 23, pp. 3833–3841, 2002.
- [195] P. Torricelli *et al.*, “Biological glass coating on ceramic materials: in vitro evaluation using primary osteoblast cultures from healthy and osteopenic rat bone.,” *Biomaterials*, vol. 22, no. 18, pp. 2535–43, Sep. 2001.
- [196] M. Yamada, A. Valanezhad, T. Egoshi, Y. Tashima, I. Watanabe, and H. Murata, “Bioactive glass coating on zirconia by vacuum sol-dipping method,” *Dent. Mater. J.*, vol. 38, no. 4, pp. 663–670, 2019.
- [197] C. Y. K. Lung, E. Kukk, and J. P. Matinlinna, “The effect of silica-coating by sol-gel process on resin-zirconia bonding,” *Dent. Mater. J.*, vol. 32, no. 1, pp. 165–172, 2013.
- [198] M. Liu, J. Zhou, Y. Yang, M. Zheng, J. Yang, and J. Tan, “Surface modification of zirconia with polydopamine to enhance fibroblast response and decrease bacterial activity in vitro: A potential technique for soft tissue engineering applications,” *Colloids Surfaces B Biointerfaces*, vol. 136, pp. 74–83, 2015.
- [199] Y. T. Liu, T. M. Lee, and T. S. Lui, “Enhanced osteoblastic cell response on zirconia by bio-inspired surface modification,” *Colloids Surfaces B Biointerfaces*, vol. 106, pp. 37–45, 2013.
- [200] X. Yao, R. Peng, and J. Ding, “Cell-material interactions revealed via material techniques of surface patterning,” *Adv. Mater.*, vol. 25, pp. 5257–5286, 2013.

- [201] C. Luo *et al.*, “Modulating cellular behaviors through surface nanoroughness,” *J. Mater. Chem.*, vol. 22, pp. 15654–15664, 2012.
- [202] A. Daskalova *et al.*, “Effect of surface modification by femtosecond laser on zirconia based ceramics for screening of cell-surface interaction,” *Appl. Surf. Sci.*, vol. 513, pp. 1–15, 2020.
- [203] Tosoh Corporation, “Tosoh zirconia powder- Specifications and Typical Properties,” 2004.
- [204] J. Grech and E. Antunes, “Zirconia in dental prosthetics: A literature review,” *J. Mater. Res. Technol.*, vol. 8, no. 5, pp. 4956–4964, 2019.
- [205] J. E. Blendell, “Solid-state Sintering,” *Encycl. Mater. Sci. Technol.*, pp. 8745–8750, 2001.
- [206] B. Stawarczyk, M. Özcan, L. Hallmann, A. Ender, A. Mehl, and C. H. F. Hämmerlet, “The effect of zirconia sintering temperature on flexural strength , grain size , and contrast ratio,” *Clin. Oral Investig.*, vol. 17, no. 1, pp. 269–274, 2012.
- [207] Struers Company, “Metallographic products, knowledge and service | Struers.com.” [Online]. Available: <https://www.struers.com/en>. [Accessed: 16-Mar-2020].
- [208] K. Sundararajan, “Design of Experiments ,” *ISIXSIGMA*. [Online]. Available: <https://www.isixsigma.com/tools-templates/design-of-experiments-doe/design-experiments-primer/>. [Accessed: 18-May-2020].
- [209] J. Calvo-De La Rosa, “Mechanical and functional properties in magnetic materials,” Universitat de Barcelona, 2019.
- [210] Unit Operations Lab, “Introduction to Design of Experiments (DOE).”
- [211] S. F. Wojtkiewicz, M. S. Eldred, A. A. Giunta, S. F. † Wojtkiewicz, and M. S. Eldred, “Overview of modern design of experiments methods for computational simulations ,” *Am. Inst. Aeronaut. Astronaut.*, 2003.
- [212] Spectra-Physics, “Explorer One - Compact and Lightweight UV and Green ns Lasers Datsheet.”
- [213] A. B. Spierings, M. Schneider, and R. Eggenberger, “Comparison of density measurement techniques for additive manufactured metallic parts,” *Rapid Prototyp. J.*, vol. 17, no. 5, pp. 380–386, Aug. 2011.
- [214] “Archimedes’ principle ,” *Encyclopaedia Britannica*, 2019. [Online]. Available: <https://www.britannica.com/science/Archimedes-principle>. [Accessed: 05-May-2020].
- [215] Mettler Toledo, “Density Measurement with Laboratory Balances ,” *YouTube*, 07-Mar-2018. [Online]. Available: [https://www.youtube.com/watch?time\\_continue=121&v=uqnDGa1UN5o&feature=emb\\_logo](https://www.youtube.com/watch?time_continue=121&v=uqnDGa1UN5o&feature=emb_logo). [Accessed: 05-May-2020].
- [216] “Microscopio para la ciencia de materiales BX53M ,” *Olympus*. [Online]. Available: [https://www.olympus-ims.com/es/microscope/bx53m/#!cms\[focus\]=cmsContent13566](https://www.olympus-ims.com/es/microscope/bx53m/#!cms[focus]=cmsContent13566).



[Accessed: 05-May-2020].

- [217] “Confocal Microscopes ,” *University of Queensland*, 27-Aug-2019. [Online]. Available: <https://imb.uq.edu.au/facilities/microscopy/hardware-software/confocal-microscopes>. [Accessed: 06-May-2020].
- [218] “Olympus: LEXT OLS3100 ,” *Olympus*. [Online]. Available: <https://microscopy-news.com/products/systems/olympus-lext-ols3100/>. [Accessed: 06-May-2020].
- [219] A. K. Chatterjee, *Handbook of Analytical Techniques in Concrete Science and Technology*. Elsevier, 2001.
- [220] H. Toraya, M. Yoshimura, and S. Somiya, “Calibration Curve for Quantitative Analysis of the Monoclinic-Tetragonal ZrO<sub>2</sub> System by X-Ray Diffraction,” *J. Am. Ceram. Soc.*, vol. 67, no. 6, p. 119-121, 1984.
- [221] J. J. Roa, M. Turon-Vinas, and M. Anglada, “Surface grain size and texture after annealing ground zirconia,” *J. Eur. Ceram. Soc.*, vol. 36, no. 6, pp. 1519–1525, May 2016.
- [222] M. J. Abden, M. K. Islam, J. D. Afroze, M. J. Abden, M. K. Islam, and J. D. Afroze, “Microstructure and Mechanical Properties of 3YSZ Ceramics Reinforced with Al<sub>2</sub>O<sub>3</sub> Particles,” *Int. J. Mater. Eng.*, vol. 4, no. 4, pp. 129–135, 2014.
- [223] A. Umeri, “Study of Zirconia’s ageing for applications in dentistry 1,” 2010.
- [224] K. G. I. H, I. A, and M. T, “Direct determination by a Raman microprobe of the transformation zone size in Y<sub>2</sub>O<sub>3</sub> containing tetragonal ZrO<sub>2</sub> polycrystals,” *Adv. Ceram.*, vol. 24A, pp. 537–544, 1988.
- [225] J. Minguela *et al.*, “Evolution of microstructure and residual stresses in gradually ground/polished 3Y-TZP,” *J. Eur. Ceram. Soc.*, vol. 40, no. 4, pp. 1582–1591, 2020.
- [226] “Scanning Electron Microscopy - Nanoscience Instruments,” *NanoScience instruments*, 2020. [Online]. Available: <https://www.nanoscience.com/techniques/scanning-electron-microscopy/>. [Accessed: 07-May-2020].
- [227] S. Swapp, “Scanning Electron Microscopy (SEM),” *Science Education Resource Center*, 27-May-2017. [Online]. Available: [https://serc.carleton.edu/research\\_education/geochemsheets/techniques/SEM.html](https://serc.carleton.edu/research_education/geochemsheets/techniques/SEM.html). [Accessed: 07-May-2020].
- [228] W. Zhou, R. Apkarian, Z. L. Wang, and D. Joy, “Fundamentals of scanning electron microscopy (SEM),” *Scanning Microsc. Nanotechnol. Tech. Appl.*, pp. 1–40, 2007.
- [229] “Phenom XL - Microscopio Electrónico de Barrido,” *LabTop*, 2020. [Online]. Available: <https://labtop.pe/productos/analisis-instrumental/microscopio-electronico-barrido-phenom-xl-detail>. [Accessed: 07-May-2020].
- [230] “Atomic Force Microscope Principle,” *Park Systems*. [Online]. Available: <https://parksystems.com/medias/nano-academy/how-afm-works>. [Accessed: 08-May-2020].

- [231] W. Mai, "Fundamental Theory of Atomic Force Microscopy," *Professor Zhong L. Wang's Nano Research Group*. [Online]. Available: <http://www.nanoscience.gatech.edu/zwang/research/afm.html>. [Accessed: 08-May-2020].
- [232] "Scanning Probe Microscopy," *ETH Zürich*, 2020. [Online]. Available: <https://ferroic.mat.ethz.ch/research/methods/atomic-force-microscope.html>. [Accessed: 08-May-2020].
- [233] "Vickers Hardness Testing," *Newage hardness testing*. [Online]. Available: <https://www.hardnesstesters.com/test-types/vickers-hardness-testing>. [Accessed: 08-May-2020].
- [234] J. Schindelin *et al.*, "Fiji - an Open platform for biological image analysis," *Nat. Methods*, vol. 9, no. 7, 2009.
- [235] E. Camposilvan, F. G. Marro, A. Mestra, and M. Anglada, "Enhanced reliability of yttria-stabilized zirconia for dental applications," *Acta Biomater.*, vol. 17, pp. 36–46, 2015.
- [236] E. Roitero, F. Lasserre, M. Anglada, F. Mücklich, and E. Jiménez-Piqué, "A parametric study of laser interference surface patterning of dental zirconia: Effects of laser parameters on topography and surface quality," *Dent. Mater.*, vol. 33, no. 1, pp. e28–e38, 2017.
- [237] A. Paul, B. Vaidhyanathan, and J. Binner, "Micro-Raman spectroscopy of indentation induced phase transformation in nanozirconia ceramics," *Adv. Appl. Ceram.*, vol. 110, no. 2, pp. 114–119, 2011.
- [238] J. A. Muñoz-Tabares, "Cambios microestructurales en 3Y-TZP desbastada y su influencia en la degradación hidrotérmica," 2010.

## Annex A

### Annex A.1 Design of Experiments

Regarding the experimental design of the laser conditions, the goal of the research is to find the optimum laser parameters that adequately most the surface roughness patterns in order to enhance the cell adhesion. A full factorial approach was followed for the design of the laser experiments. The critical parameters to take into consideration for this analysis are: laser beam intensity, frequency, and mark speed. The selection process was made based on the **depth** of the laser paths since the cellular response is strongly influenced by the surface roughness of the sample, as explained in the **section 2.2.4**. A summary of the group of tests planned and done along this Master's thesis are presented in **Table 12**.

*Table 12. Conditions for the laser tests.*

Test number	Intensity (A)	Mark speed (bits/mseg)	Frequency (Hz)
Test 1	1.1	2	Variable*
	1.2	2	Variable*
	1.3	5	Variable*
Test 2	2.1	2,5	Variable*
	2.2	2,5	Variable*
	2.3	5	Variable*
Test 3	3.1	3	Variable*
	3.2	2	Variable*
	3.3	5	Variable*

\*250Hz, 500Hz, 750Hz and 1000Hz

The next step was to characterize the penetration depth (or total height produced on each test). The measurements were performed by CLSM, as represented in **Figure 85**.

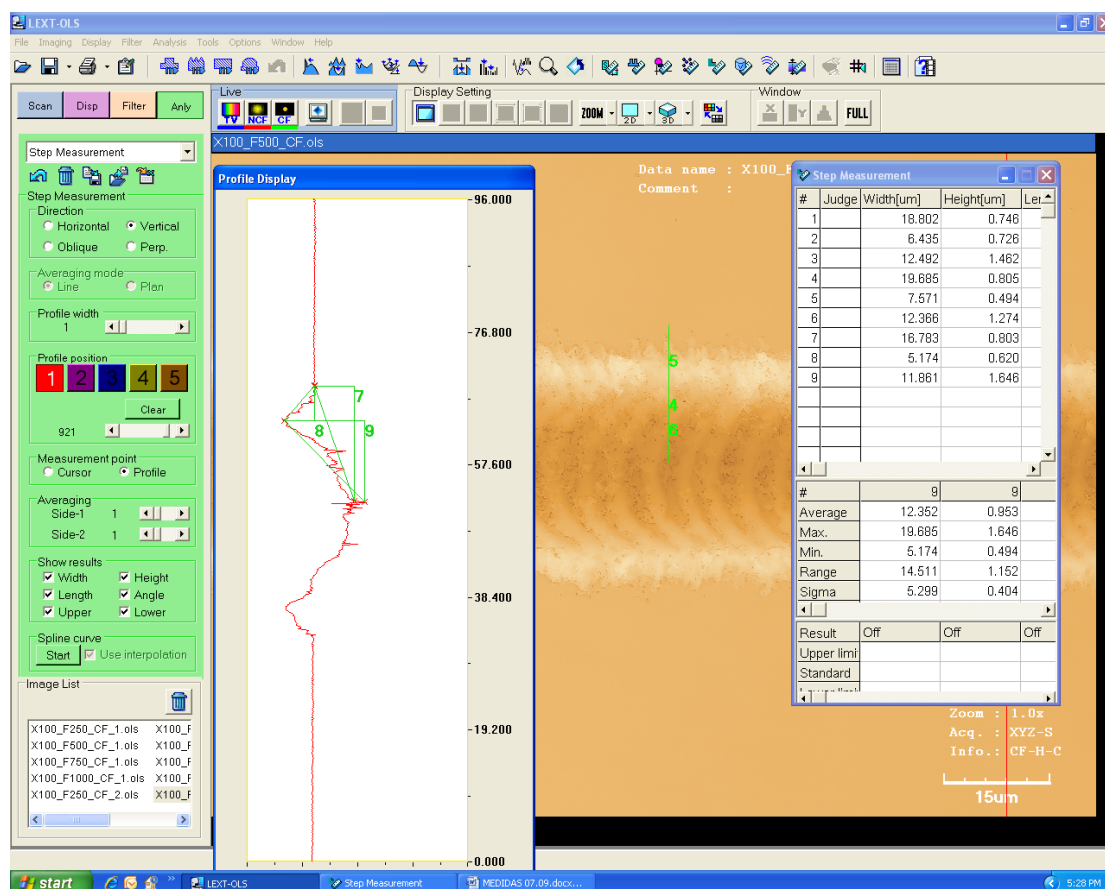


Figure 85. Depth measurement of the tests by CLSM.

Once all the depth of all test were measures, the next step was to plot the tendency lines of the depth in function of the laser intensity, scan speed and frequency. Since several studied agreed that the optimum roughness to promote cellular response is ranged between 1-2 $\mu$ m, the laser parameters were chosen accordingly to that penetration depth. In **Figure 86a**, **Figure 86b** and **Figure 86c** are represented the variation the depth with the laser intensity, frequency and scan speed, respectively. The observation made about the obtained tendencies are:

- The depth is increased when the laser intensity is increased
- The depth is increased when the laser frequency is increased
- The depth is decreased when scan speed is augmented

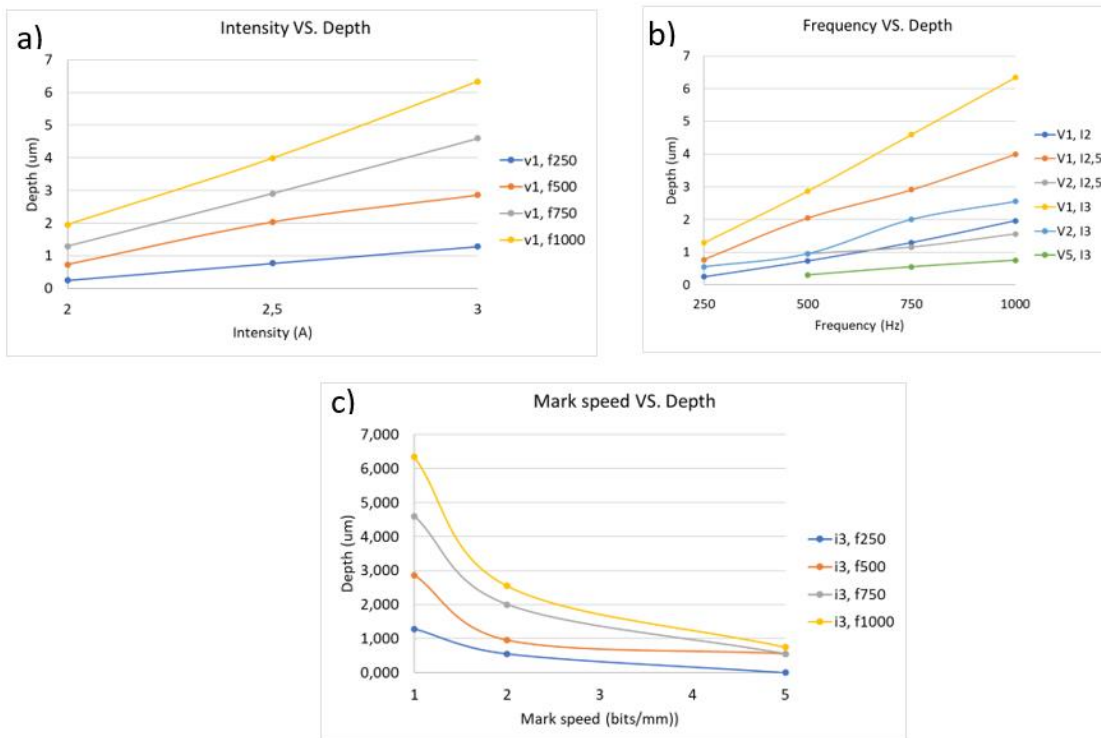


Figure 86. Variation of the depth with a) laser intensity, b) laser frequency, c) scan speed.

Furthermore, as stated above, the desired laser pattern for this project should have a total height between 1-2  $\mu\text{m}$ . From all the 36 tests performed in the DoE, only 8 were in that range.

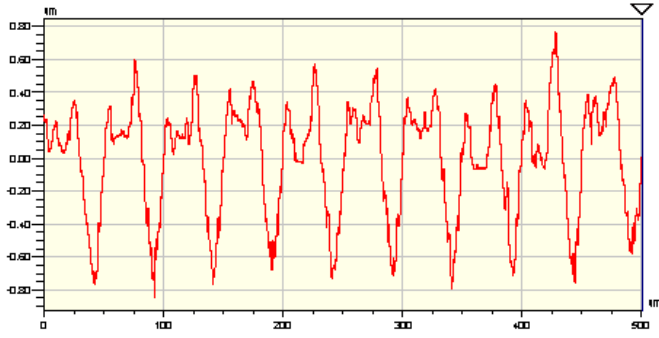
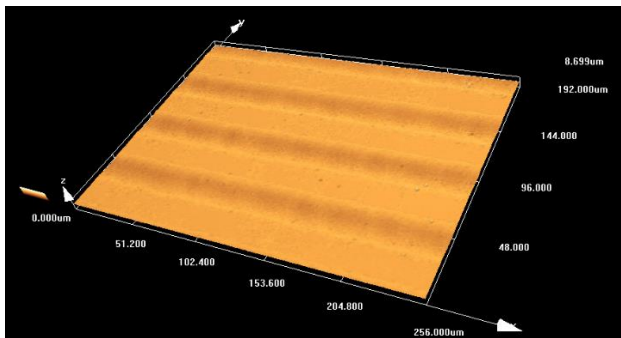
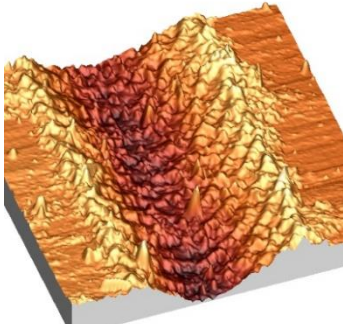
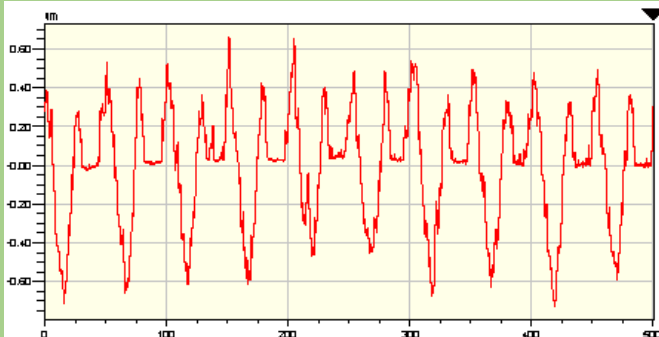
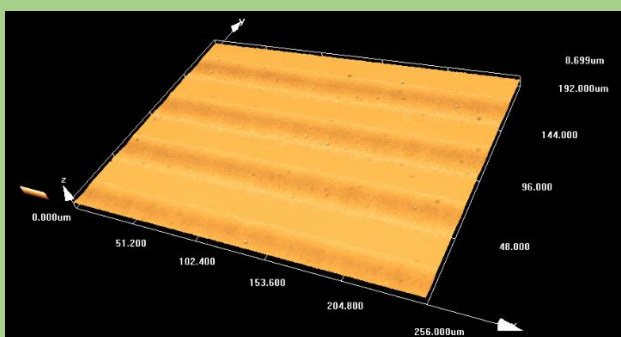
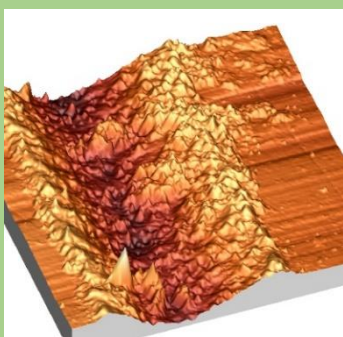
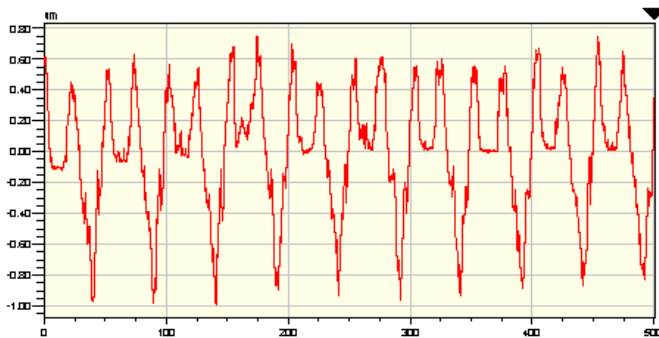
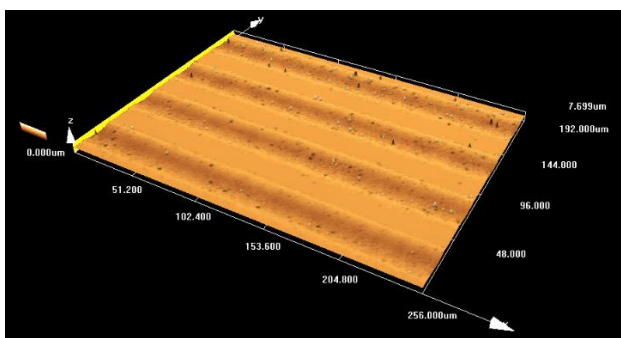
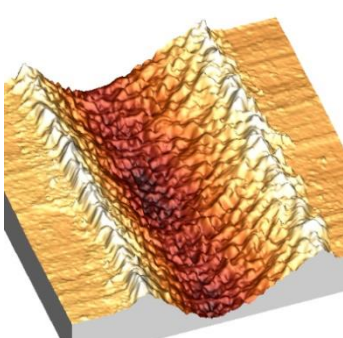
After, those 8 laser paths were then characterized in more detail by mean of AFM, contact profilometry and LCSM. Patterns with parallel lines of 30  $\mu\text{m}$  and 50  $\mu\text{m}$  inter-space were produced for each of the 8 laser combinations. The AFM result allows to analyze the laser topography in more detail, while by using the contact profilometer the repeatability of the laser line measures was evaluated. The results are presented in **Table 13** and **Table 14**, for the 50 $\mu\text{m}$  and 30 $\mu\text{m}$  interspacing, respectively. The final decision of the laser parameter was made by considering:

- Total height (depth) in the range of 1-2  $\mu\text{m}$
- Minimum pileup to minimize the side effect of the laser beam.
- Repeatability of the lines along the parallel lines.

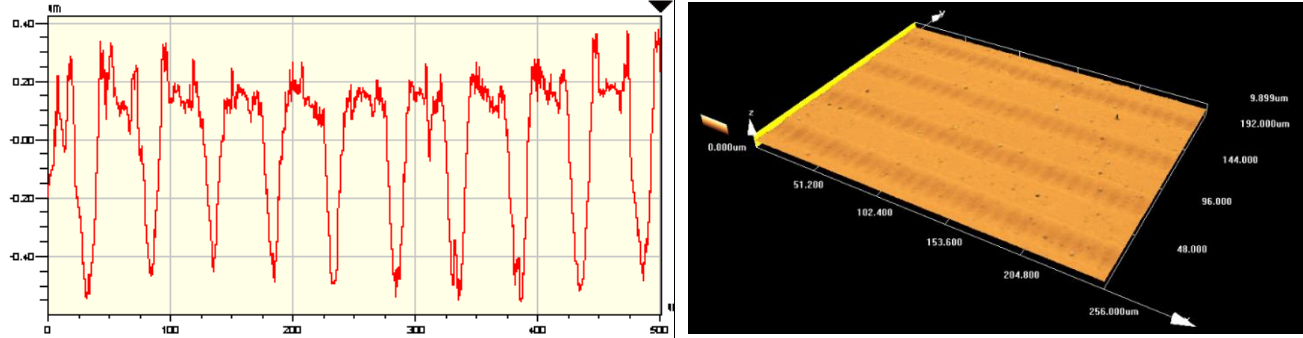
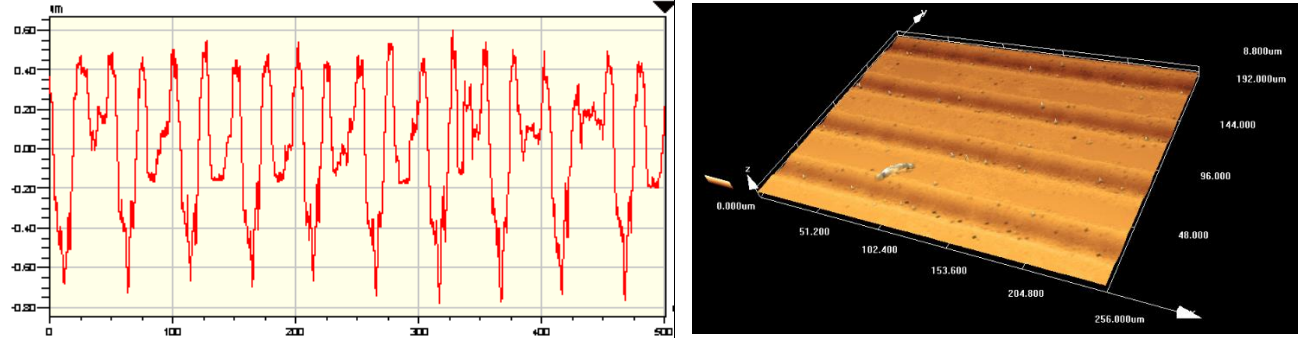
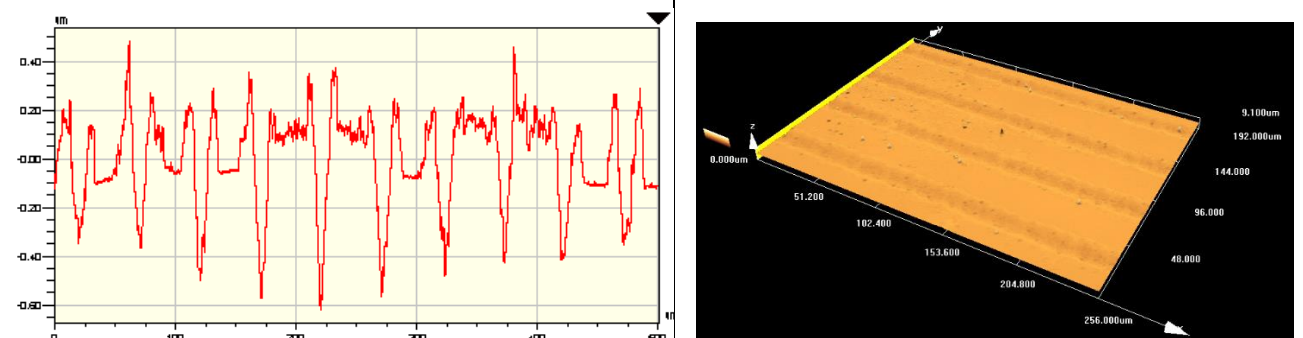
Accordingly to that, the selected parameters are marked:

- *Intensity:* 2.5A
- *Scan speed:* 2 bit/ms
- *Frequency:* 500Hz

Table 13. Contact profilometer, confocal microscope and AFM result of the 50um interspacing samples

Interspacing: 50um														
S	Speed (bits/ms)	I (A)	F (Hz)	Dist. pulse	Contact profilometer			Confocal microscope	AFM					
1	1	2,5	250	4,8	R <sub>v</sub> (um)	R <sub>p</sub> (um)	R <sub>t</sub>	R <sub>t</sub>	h <sub>laser</sub>	h <sub>pil-up</sub>	h <sub>t</sub>	w <sub>laser</sub>	w <sub>pil-up</sub>	w <sub>t</sub>
					0,84	0,77	1,61	1,363 ±0,130	0,74 ±0,04	0,40 ±0,10	1,14 ±0,05	20,69 ±1,66	5,97 ±1,19	34,86 ±0,93
														
2	2	2,5	500	4,8	R <sub>v</sub> (um)	R <sub>p</sub> (um)	R <sub>t</sub>	R <sub>t</sub>	h <sub>laser</sub>	h <sub>pil-up</sub>	h <sub>t</sub>	w <sub>laser</sub>	w <sub>pil-up</sub>	w <sub>t</sub>
					-0,730	0,660	1,390	1,466 ±0,010	0,91 ±0,09	0,31 ±0,11	1,22 ±0,17	19,27 ±0,40	6,47 ±0,87	31,95 ±2,29
														
3	2	2,5	750	3,2	R <sub>v</sub> (um)	R <sub>p</sub> (um)	R <sub>t</sub>	R <sub>t</sub>	h <sub>laser</sub>	h <sub>pil-up</sub>	h <sub>t</sub>	w <sub>laser</sub>	w <sub>pil-up</sub>	w <sub>t</sub>
					-0,990	0,750	1,730	1,859 ±0,103	1,21 ±0,11	0,44 ±0,11	1,63 ±0,07	21,24 ±1,07	5,29 ±1,01	32,67 ±1,78
														



4	2	3	250	9,6	<b>R<sub>v</sub> (um)</b>	<b>R<sub>p</sub> (um)</b>	<b>R<sub>t</sub></b>	<b>R<sub>t</sub></b>	<b>h<sub>laser</sub></b>	<b>h<sub>pil-up</sub></b>	<b>h<sub>t</sub></b>	<b>w<sub>laser</sub></b>	<b>w<sub>pil-up</sub></b>	<b>w<sub>t</sub></b>
					-0,550	0,380	0,930	1,102 ±0,117	0,45 ±0,04	0,23 ±0,04	0,67 ±0,05	16,88 ±0,40	13,51 ±3,01	36,83 ±4,19
														
5	2	3	500	4,8	<b>R<sub>v</sub> (um)</b>	<b>R<sub>p</sub> (um)</b>	<b>R<sub>t</sub></b>	<b>R<sub>t</sub></b>	<b>h<sub>laser</sub></b>	<b>h<sub>pil-up</sub></b>	<b>h<sub>t</sub></b>	<b>w<sub>laser</sub></b>	<b>w<sub>pil-up</sub></b>	<b>w<sub>t</sub></b>
					-0,780	0,530	1,310	2,775 ± 0,027	1,33 ±0,15	0,57 ±0,05	1,91 ±0,17	16,76 ±0,23	11,84 ±1,84	38,03 ±3,38
														
6	5	3	500	12	<b>R<sub>v</sub> (um)</b>	<b>R<sub>p</sub> (um)</b>	<b>R<sub>t</sub></b>	<b>R<sub>t</sub></b>	<b>h<sub>laser</sub></b>	<b>h<sub>pil-up</sub></b>	<b>h<sub>t</sub></b>	<b>w<sub>laser</sub></b>	<b>w<sub>pil-up</sub></b>	<b>w<sub>t</sub></b>
					-0,620	0,480	1,100	0,995 ±0,066	0,60 ±0,05	0,35 ±0,09	0,96 ±0,03	13,65 ±0,58	5,78 ±0,39	23,39 ±6,90
														

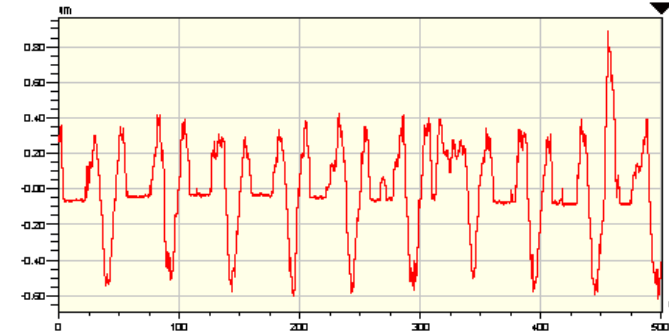
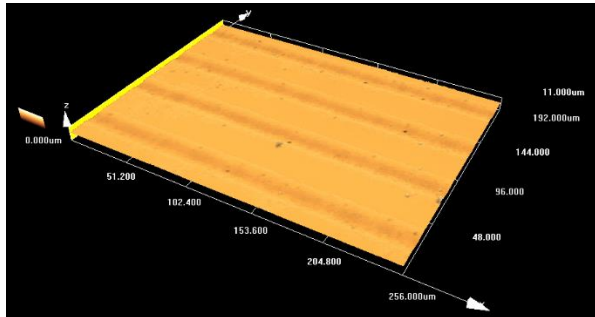
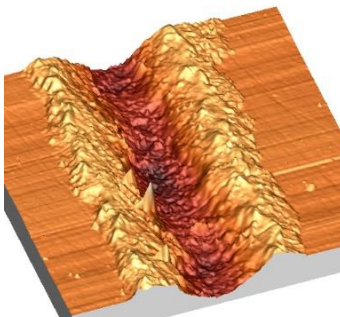
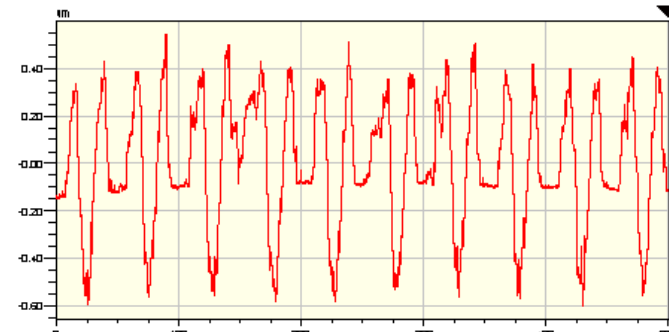
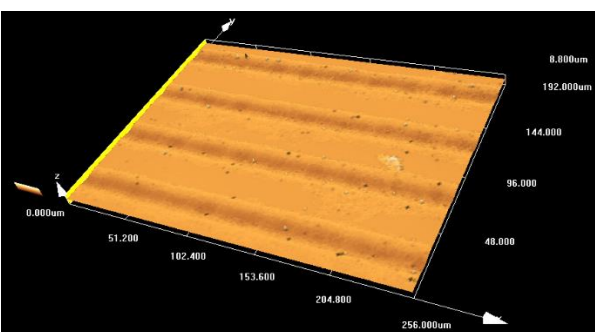
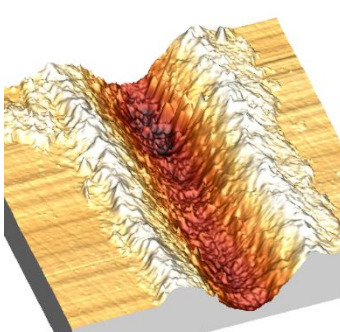
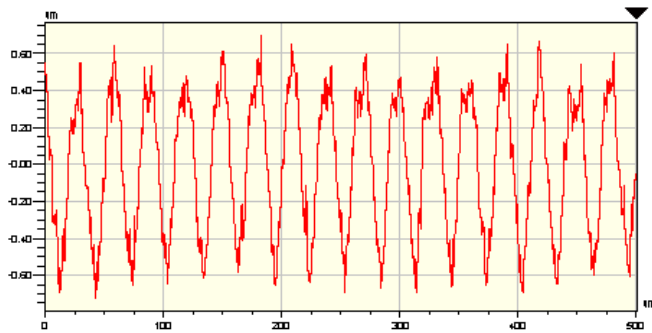
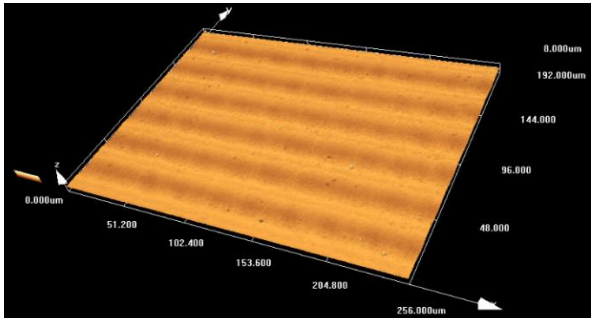
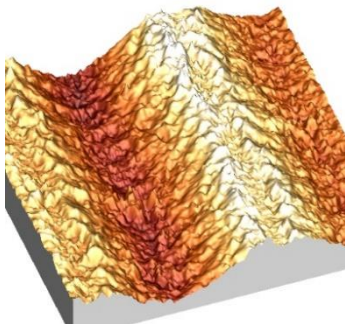
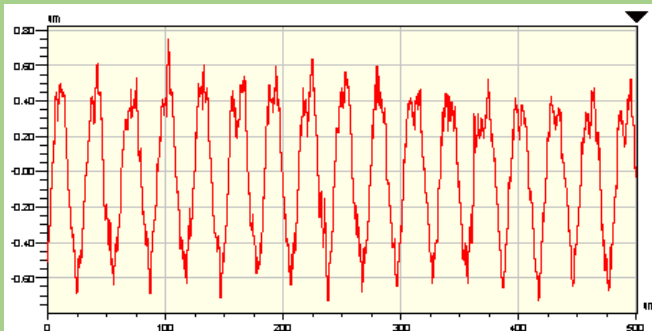
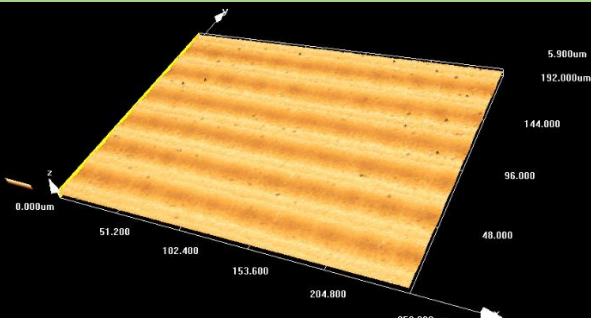
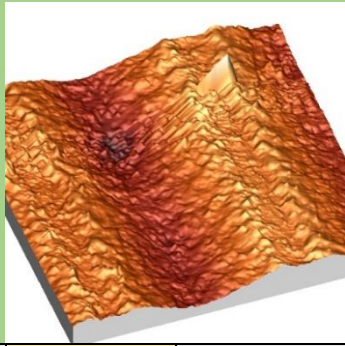
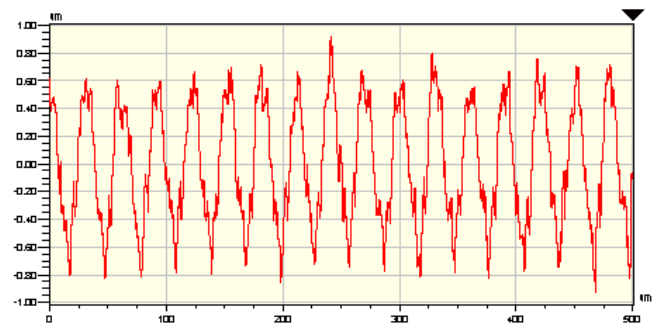
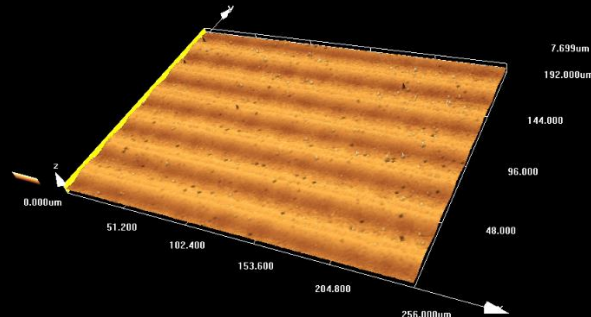
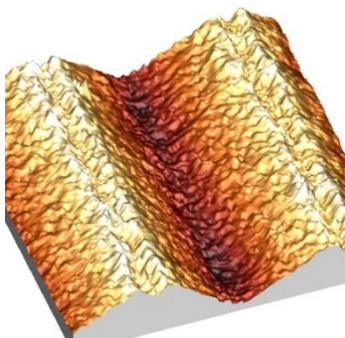
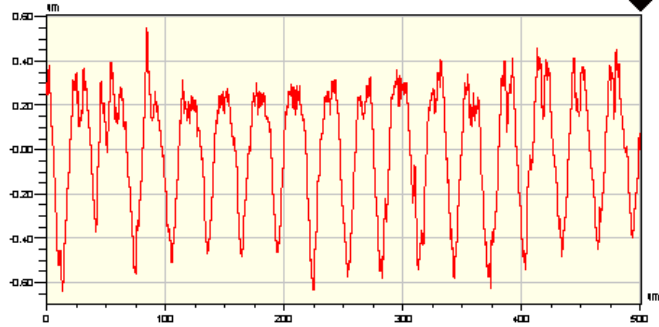
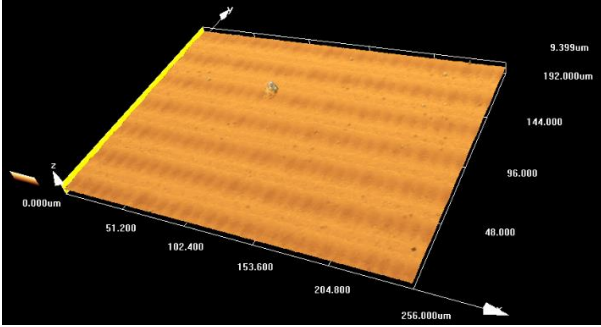
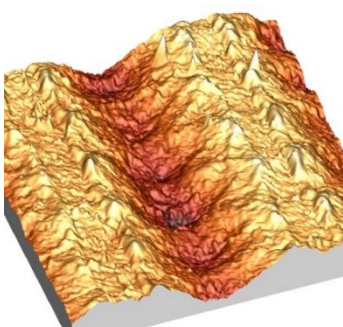
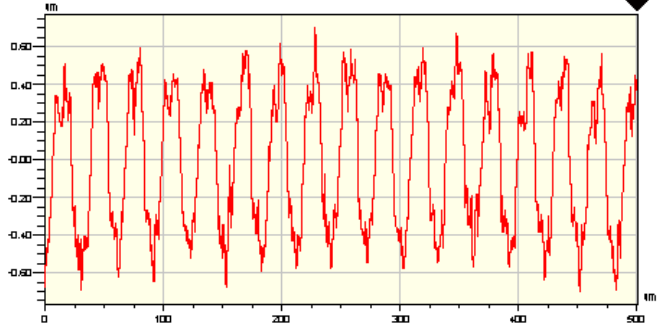
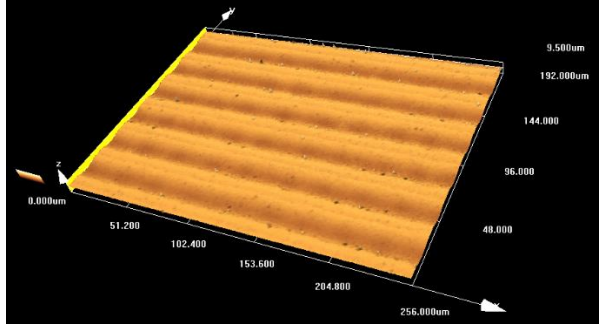
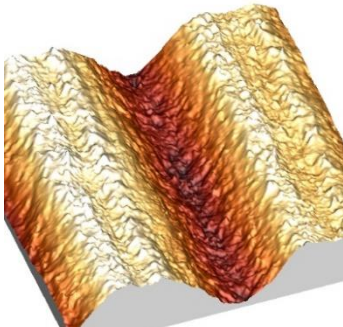
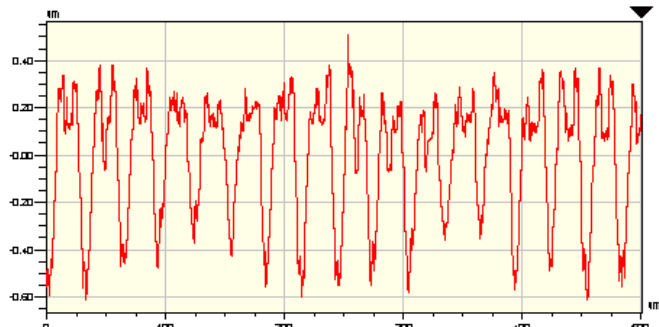
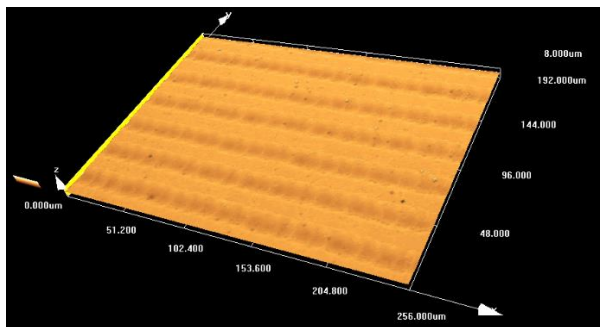
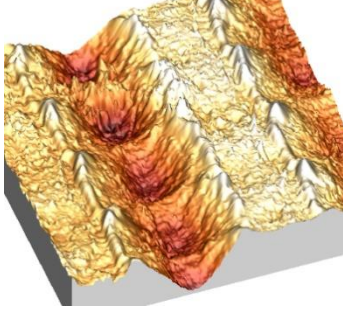
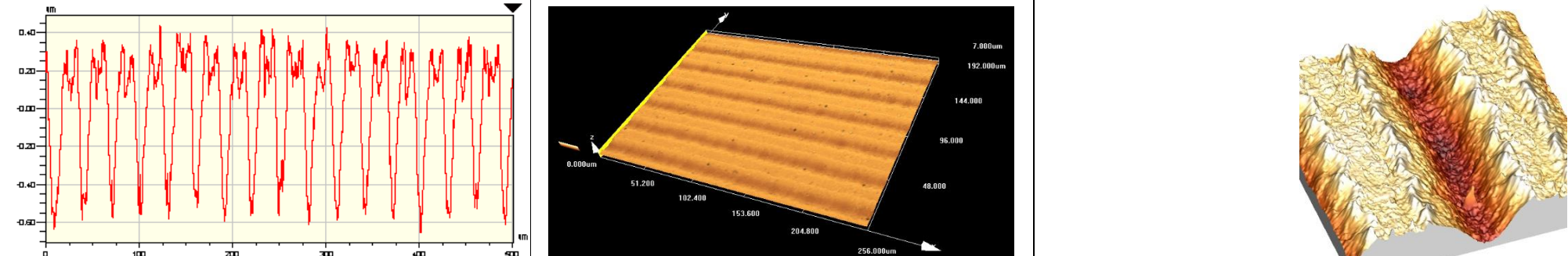
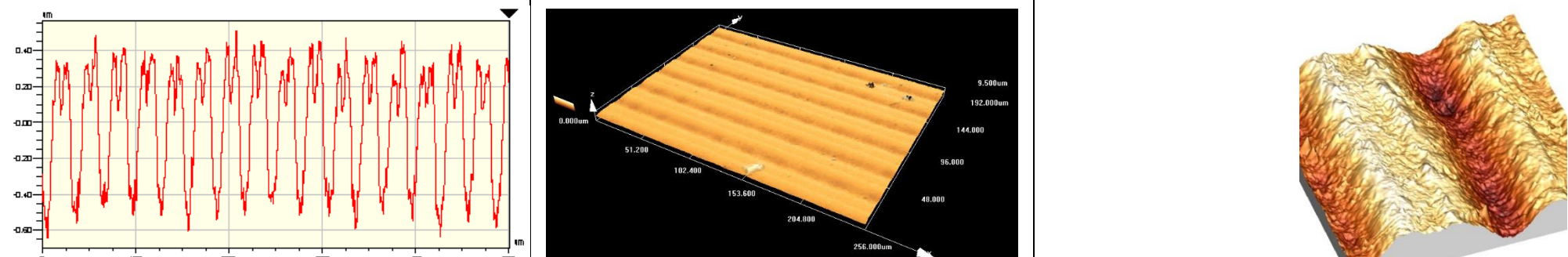
7	5	3	750	8	<b>R<sub>v</sub> (um)</b>	<b>R<sub>p</sub> (um)</b>	<b>R<sub>t</sub></b>	<b>R<sub>t</sub></b>	<b>h<sub>laser</sub></b>	<b>h<sub>pil-up</sub></b>	<b>h<sub>t</sub></b>	<b>w<sub>laser</sub></b>	<b>w<sub>pil-up</sub></b>	<b>w<sub>t</sub></b>
					-0,620	0,890	1,500	1,549 ±0,260	0,77 ±0,14	0,37 ±0,07	1,15 ±0,23	12,67 ±0,76	7,15 ±1,12	28,46 ±0,35
														
8	5	3	1000	6	<b>R<sub>v</sub> (um)</b>	<b>R<sub>p</sub> (um)</b>	<b>R<sub>t</sub></b>	<b>R<sub>t</sub></b>	<b>h<sub>laser</sub></b>	<b>h<sub>pil-up</sub></b>	<b>h<sub>t</sub></b>	<b>w<sub>laser</sub></b>	<b>w<sub>pil-up</sub></b>	<b>w<sub>t</sub></b>
					-0,600	0,540	1,140	2,099 ±0,109	1,04 ±0,05	0,40 ±0,03	1,43 ±0,07	14,80 ±0,60	7,45 ±0,65	30,30 ±1,38
														



Table 14. Contact profilometer, confocal microscope and AFM result of the 50um interspacing samples

Interlineado: 30um															
S	Seed (bits/ms)	I (A)	F (Hz)	Dist. pulse	Contact profilometer			Confocal microscope	AFM						
1	1	2,5	250	4,8	R <sub>v</sub> (um)	R <sub>p</sub> (um)	R <sub>t</sub>	R <sub>t</sub>	h <sub>laser</sub>	h <sub>pil-up</sub>	h <sub>t</sub>	w <sub>laser</sub>	w <sub>pil-up</sub>	w <sub>t</sub>	
					-0,720	0,700	1,420	1,668 ±0,021	1,03 ±0,07	0,50 ±0,08	1,53 ±0,15	18,51 ±0,87	5,38 ±0,13	27,32 ±1,33	
															
2	2	2,5	500	4,8	R <sub>v</sub> (um)	R <sub>p</sub> (um)	R <sub>t</sub>	R <sub>t</sub>	h <sub>laser</sub>	h <sub>pil-up</sub>	h <sub>t</sub>	w <sub>laser</sub>	w <sub>pil-up</sub>	w <sub>t</sub>	
					-0,730	0,750	1,470	1,548 ±0,407	0,98 ±0,08	0,31 ±0,03	1,31 ±0,11	17,38 ±0,36	5,61 ±0,21	27,21 ±0,81	
															
3	2	2,5	750	3,2	R <sub>v</sub> (um)	R <sub>p</sub> (um)	R <sub>t</sub>	R <sub>t</sub>	h <sub>laser</sub>	h <sub>pil-up</sub>	h <sub>t</sub>	w <sub>laser</sub>	w <sub>pil-up</sub>	w <sub>t</sub>	
					-0,920	0,920	1,840	2,588 ±0,214	1,59 ±0,09	0,36 ±0,02	1,96 ±0,11	18,54 ±0,28	4,45 ±0,55	28,71 ±0,80	
															

4	2	3	250	9,6	<b>R<sub>v</sub> (um)</b>	<b>R<sub>p</sub> (um)</b>	<b>R<sub>t</sub></b>	<b>R<sub>t</sub></b>	<b>h<sub>laser</sub></b>	<b>h<sub>pil-up</sub></b>	<b>h<sub>t</sub></b>	<b>w<sub>laser</sub></b>	<b>w<sub>pil-up</sub></b>	<b>w<sub>t</sub></b>
					-0,640	0,550	1,190	1,322 ±0,028	0,80 ±0,16	0,26 ±0,03	1,07 ±0,16	16,66 ±0,34	4,60 ±0,36	25,64 ±0,75
														
5	2	3	500	4,8	<b>R<sub>v</sub> (um)</b>	<b>R<sub>p</sub> (um)</b>	<b>R<sub>t</sub></b>	<b>R<sub>t</sub></b>	<b>h<sub>laser</sub></b>	<b>h<sub>pil-up</sub></b>	<b>h<sub>t</sub></b>	<b>w<sub>laser</sub></b>	<b>w<sub>pil-up</sub></b>	<b>w<sub>t</sub></b>
					-0,700	0,700	1,400	2,419 ±0,013	1,63 ±0,08	0,36 ±0,09	1,99 ±0,13	16,53 ±0,45	5,41 ±0,22	27,23 ±0,47
														
6	5	3	500	12	<b>R<sub>v</sub> (um)</b>	<b>R<sub>p</sub> (um)</b>	<b>R<sub>t</sub></b>	<b>R<sub>t</sub></b>	<b>h<sub>laser</sub></b>	<b>h<sub>pil-up</sub></b>	<b>h<sub>t</sub></b>	<b>w<sub>laser</sub></b>	<b>w<sub>pil-up</sub></b>	<b>w<sub>t</sub></b>
					-0,610	0,510	1,120	1,335 ±0,223	0,72 ±0,06	0,23 ±0,03	0,96 ±0,09	13,69 ±0,32	3,35 ±0,88	21,06 ±0,50
														

7	5	3	750	8	<b>R<sub>v</sub> (um)</b>	<b>R<sub>p</sub> (um)</b>	<b>R<sub>t</sub></b>	<b>R<sub>t</sub></b>	<b>h<sub>laser</sub></b>	<b>h<sub>pil-up</sub></b>	<b>h<sub>t</sub></b>	<b>w<sub>laser</sub></b>	<b>w<sub>pil-up</sub></b>	<b>w<sub>t</sub></b>
					-0,650	0,440	1,090	1,740 ±0,009	1,91 ±0,07	0,28 ±0,04	1,19 ±0,06	13,80 ±0,39	5,25 ±0,25	23,53 ±1,02
														
8	5	3	1000	6	<b>R<sub>v</sub> (um)</b>	<b>R<sub>p</sub> (um)</b>	<b>R<sub>t</sub></b>	<b>R<sub>t</sub></b>	<b>h<sub>laser</sub></b>	<b>h<sub>pil-up</sub></b>	<b>h<sub>t</sub></b>	<b>w<sub>laser</sub></b>	<b>w<sub>pil-up</sub></b>	<b>w<sub>t</sub></b>
					-0,640	0,510	1,150	1,905 ±0,107	1,26 ±0,11	0,25 ±0,03	1,50 ±0,12	14,71 ±0,56	4,92 ±0,22	24,69 ±0,45
														

## Annex A.2 Interface of L-Win and Weldmark

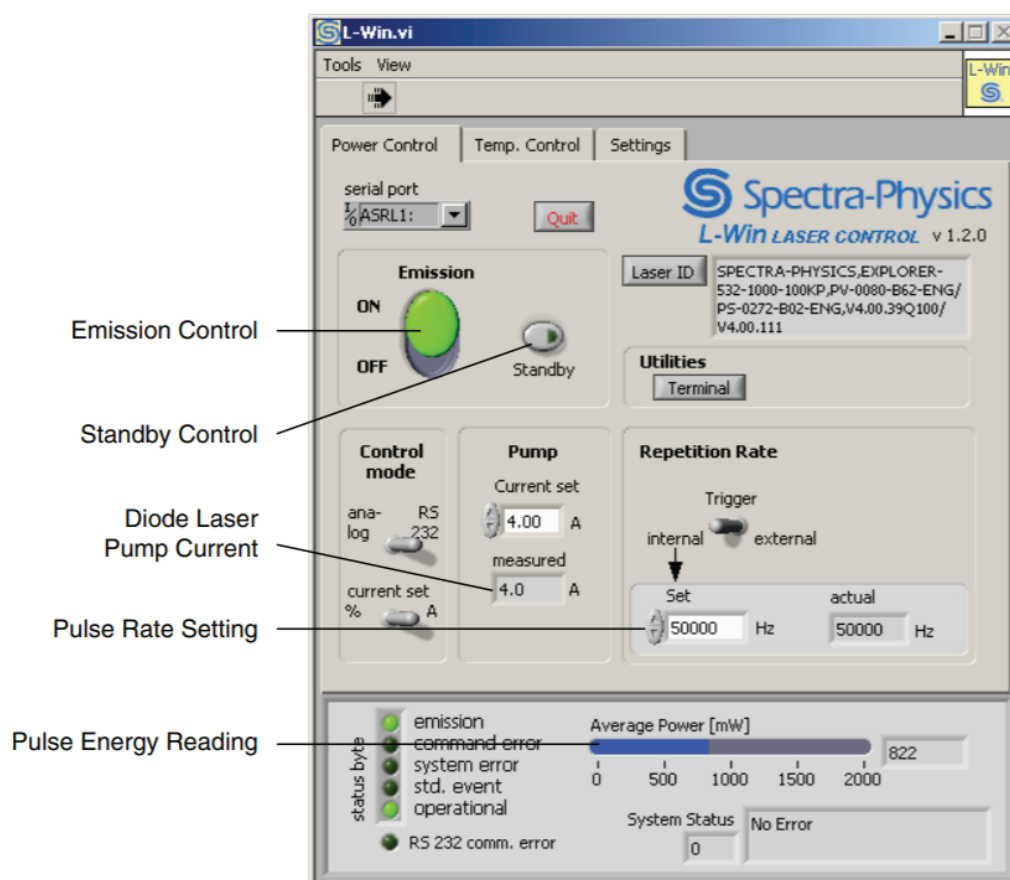


Figure 87. L-Win main display.



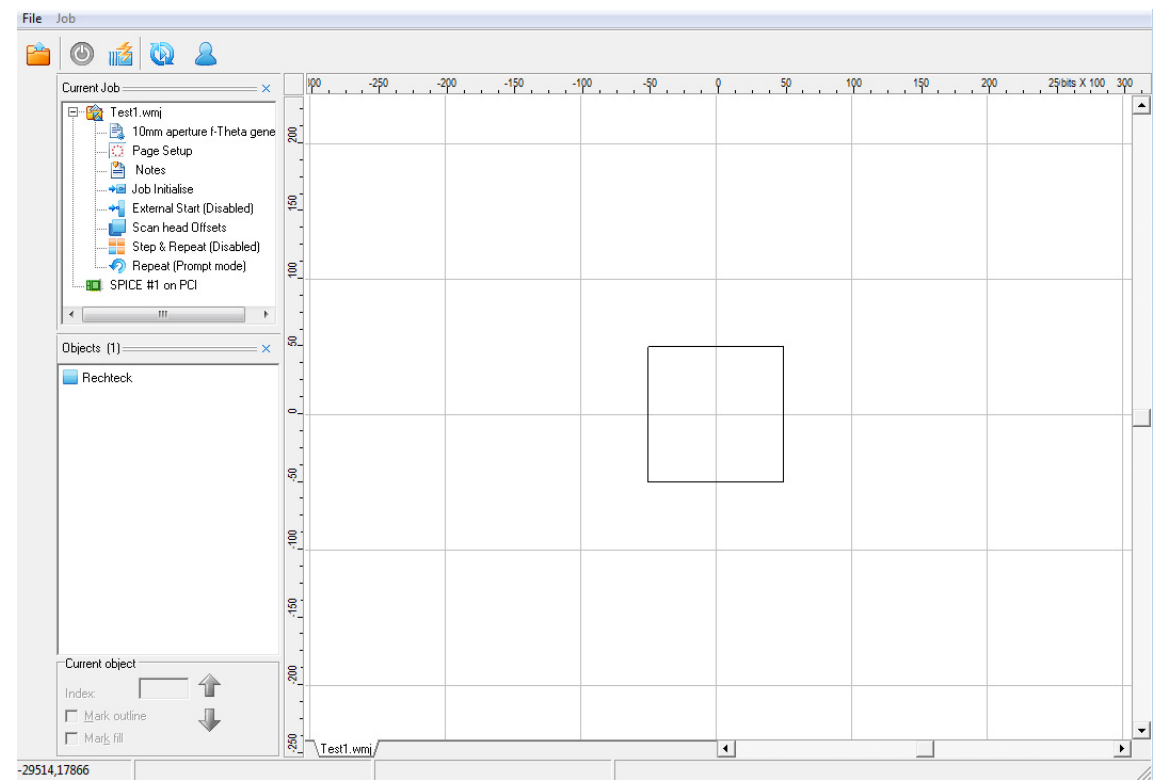


Figure 88. The interface of WeldMARK.

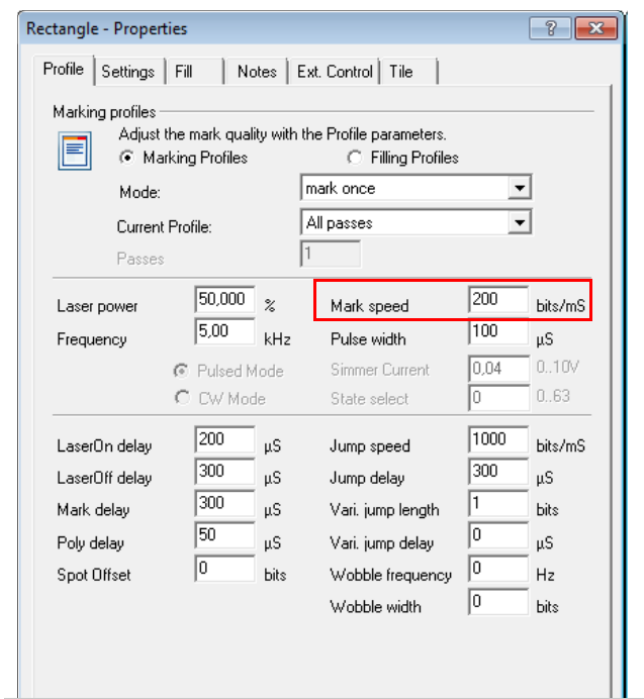


Figure 89. Properties table to modify the mark speed in WeldMARK.